Enhancing the Resiliency and Cybersecurity of Power System State Estimation with High Breakdown Point Robust Estimators

A Dissertation

Presented in Partial Fulfillment of the Requirements for the

Degree of Doctor of Philosophy

with a

Major in Electrical Engineering

in the

College of Graduate Studies

University of Idaho

by

Andrew G. Miles

Approved by:

Major Professor: Yacine Chakhchoukh, Ph.D.

Committee Members: Brian K. Johnson, Ph.D.; Herbert Hess, Ph.D.; Eric Wolbrecht, Ph.D.

Department Administrator: Joseph D. Law, Ph.D.

May 2022

Abstract

As the power system grows in complexity, so does the need for accurate real-time information. The real-time information allows operators to evaluate a system state to control, plan, automate, and operate the power system. Many of the existing state-estimation methods are based on a Gaussian noise assumption on the error in the measurement data used in the model. The weighted least squares (WLS) estimator, Kalman filters such as the Extended Kalman filter (EKF), and Unscented Kalman filter (UKF), which produce optimal results with this assumption, are popular. However, recent research has shown that measurements errors in phasor measurement units within the power system trend toward non-gaussian probability distributions. Due to the non-gaussian noise, the increased model complexity, and the possible occurrence of cyberattacks, the need for robust estimators has grown significantly. In this work, two robust high-breakdown regression estimators, namely S- and MM-estimators, are adapted and implemented to provide resistance to modeling errors, non-Gaussian noise, and false data injection attacks (FDI). The proposed estimators are applied to two critical future applications. The first considered application is a poly-phase distribution static-state estimator (DSSE). The proposed DSSE estimators show better performance than estimators proposed in the literature, such as the WLS with bad data detection and the robust Huber M-based estimator. The proposed estimators offer more accurate state estimates and energy distribution locational marginal prices (DLMPS) as demonstrated on a modified IEEE 13-bus system in the presence of topology attacks. The second application is a robust distributed or decentralized dynamic state estimator for transmission systems. The distributed dynamic state estimator will be an essential tool for utilizing wide-area monitoring systems (WAMS) using phasor measurement units for control applications. The two robust estimators are implemented for comparison, one in a centralized and one in a distributed or decentralized fashion. The second approach permits the enhancement of resiliency and cyber-security at a reduced computational cost. The IEEE 14- and 118-bus model test cases are implemented to evaluate the proposed distributed dynamic state estimation (DSE) with a transient.

Acknowledgments

I would like to firstly express my sincere gratitude to my advisor Prof. Yacine Chakhchoukh for the continuous support with my Ph.D. study and related research, for his patience motivation and immense knowledge. His guidance helped me thorough the various research projects, and writing of this dissertation. I would like to thank him for encouraging me through various research projects and for assisting me to grow as a researcher.

I would also like to thank Prof. Brian Johnson for his insightful comments and assistance with my research endeavors. I would like to thank the rest of my Ph.D. committee: Prof. Herbert Hess and Prof. Eric Wolbrecht for their insightful comments and encouragements throughout my research.

Dedication

This dissertation is dedicated to my mother, my sister, and family for their continuous encouragement, support, and patience throughout my Ph.D. study

Table of Contents

List of Tables

List of Figures

List of Abbreviations

AEP … American Electric Power

BPA … Bonneville Power Administration

CKF … Cubature Kalman Filter

DLMP … Distribution Locational Marginal Pricing

DMS … Distribution Management System

DoS … Denial of Service

DSE … Dynamic State Estimation

DSSE … Distribution Static State Estimation

DSO … Distribution System Operator

EMS … Energy Management System

FDI … False Data Injection

GPS … Global Positioning System

GSE … General State Estimation

IoT … Internet of Things

LAV … Least Absolute Value

LMP … Locational Marginal Pricing

LMS … Least Median Squares

LNR … Largest Normalized Residuals

LTS … Least Trimmed Squares

MIT … Massachusetts Institute of Technology

MITM … Man in The Middle

ODE … Ordinary Differential equations

OLS … Original Least Squares

PKF … Particle Kalman Filter

PMU … Phasor Measurement Unit

PU … Per Unit

RMSE … Root Mean Square Error

RTU … Remote Terminal Unit

SCADA … Supervisory Control and Data Acquisition

SHGM … Schweppe-Huber generalized M

SSE … Static State Estimation

SVD … Single Value Decomposition

UKF … Unscented Kalman Filter

WAMS … Wide Area Management System

WLS … Weighted Least Squares

Chapter 1   Introduction

1.1   Background and Motivation

With the advent of the deployment of the digital computer, power systems monitoring began evolving at a rapid rate, primarily due to the capability to compute large-scale power flow problems. Notably, the first successful large-scale digital power-flow program completed at the American Electric Power (AEP) paved the way for improved power system monitoring and control applications. After the 1965 blackout that affected over 30 million people, AEP and Fred Schweppe, a Massachusetts Institute of Technology (MIT) researcher, understood the importance of monitoring the status of the power system by estimating voltage magnitudes and phase angles from supervisory control and data acquisition (SCADA) measurements throughout the AEPs 345kV and 765kV network [1]–[3]. In 1972, the world's first real-time power-system static-state estimator was successfully employed. Around this time, Bonneville Power Administration (BPA) also deployed a similar state estimator on their system on the west coast.

Nowadays, these same SCADA systems have allowed for numerous applications of state estimation in power systems. This state estimation is a crucial tool integrated into the energy management system (EMS) at control centers, and its results are used in monitoring, control, and decision-making processes. For example, state estimation impacts contingency analysis, load forecasting, electricity pricing-such as computing locational marginal prices (LMPs), and autonomous controls to help operate the system in a safe state. After the initial applications by Schweppe, AEP, and BPA, power system state estimation has opened numerous avenues for new research on measuring and improving resiliency. Despite important innovations within power system state estimation bad data detection, the capability to identify and process corrupted measurements still raises much interest. Hence, there is a continual need to propose effective methods that can handle and resist corrupted measurements: identification and elimination of bad measurements or false data injection attacks, and reliable estimation in the presence of non-Gaussian noise. It is opportune to recall the key requisites for executing a practical state estimation: observability of the system, quality of measurements, correct network topology, and parameters. If the established requisites are not met, the estimator performance could be degraded and unreliable. This problem has led to the development of sophisticated state estimator algorithms robust to corrupted measurements (bad data) and network configuration and parameters errors. State estimation results should ideally be free from effects of bad data such as measurement error.

 Furthermore, one limiting factor for SCADA systems is that they observe the power system every 4 to 6 seconds, and even up to minutes. This minute timeframe allows the operators to use the SCADA measurements for pseudo real-time actions, where the state of the system is assumed to be static. To view the power system dynamically and in real-time the faster data logging rates of phasor measurement units (PMUs) are being utilized more frequently.

PMUs are capable of measuring and transmitting time synchronized voltage and current phasors at high-frequency update rates, i.e., 30 to 120 measurements per second. The PMU measurements are synchronized and time-aligned using satellite-based time reference such as clocks receiving the Global Positioning Systems (GPS) signals. The phasor measurements from PMUs have enabled researchers to develop more advanced techniques for state estimation in power systems [4]–[10], especially in the realm of real-time state estimation. Real-time state estimation computes the sate estimation methods within the data collection timeframe . Several authors have proposed the so-called hybrid SE that combines both SCADA and PMU measurements [11]–[15] . The linear PMU-based state estimator was proposed using time synchronized current and voltage phasors to evaluate the state at high rates [16]–[18]. At a given time snapshot, the measured phasors are formulated in their complex rectangular forms, and the estimation is applied to a linear regression problem. Using an increased number of PMU measurements, authors have proposed a dynamic state estimator, where states at successive times are linked together by a nonlinear function. An Extended or Unscented Kalman filter could track the dynamic states using PMU measurements[19]–[24].

These available PMU measurements and their communication infrastructure could improve state estimation availability, accuracy, and reliability. Consequently, as these technologies are implemented the potential risks of FDI cyberattacks that could modify measurements through a man-in-the-middle type intrusion increase. Thus, detecting, eliminating, or correcting corrupted measurements has become an essential area of interest for state estimation research. This can be achieved using data analytics, a model-based approach and available clean data.

This dissertation investigates and implements high breakdown, highly efficient, robust regression estimators to propose a robust static power distribution level state estimator and a robust dynamic state estimator for the transmission system to resist accidental errors or FDI attacks. Where the breakdown point is the maximum number of outliers that an estimator can resist while maintaining reliability. Efficiency is equivalent to the accuracy of the unbiased estimator with a clean data case. The regression estimators considered are the robust, fast S-estimator and Modified-M, also known as the MM-estimator proposed in robust statistics theory [25]. These robust regression estimators provide the

advantage of theoretically identifying measurement and topology errors while retaining a high breakdown point.

The application will focus on improving estimation performance in the presence of bad data for both transmission and distribution systems. As the robust estimators are applied, this work will investigate the computation time of the robust estimators, cyberattack impacts on single-phase, three-phase system state estimates, and their financial implications for energy markets and operations.

1.2   Technical Contributions

The contributions of this dissertation are summarized as follows.

1. A robust static state estimation approach is proposed and demonstrated by applying high breakdown robust regression estimators, namely the S- and MM-estimators, to three-phase distribution systems. The proposed approaches' main advantage is detecting and removing bad data from measurement vectors, and power system topologies in the three-phase coupled distribution systems. The S- and MM- estimators are also enhanced to improve convergence and computation time in large systems. The MM- could offer high efficiency when its high breakdown point is increased. The S-estimator efficiency could be enhanced by re-executing a weighted least squares estimation (WLS) after detecting and rejecting outliers based on the residuals of the S-estimator.

2. A new dynamic state estimation approach based on a robust UKF augmented with high breakdown robust regression estimators is proposed and demonstrated for the transmission level power systems at a centralized level.

3. A new distributed or decentralized robust dynamic state estimation approach is implemented applying high breakdown robust regression estimators (i.e., S-based UKF and MM-based UKF) to transmission level power systems. The robust UKF is executed on islands of the power system to enable its execution and accelerate its convergence speed and increase robustness or the number of attacks detected in large power systems.

4. A performance evaluation is provided for the proposed methods compared to some of the literature implemented UKF and Huber M-UKF with different false data injection scenarios considering the IEEE 14-bus, IEEE 57-bus, and the IEEE 118-bus transmission systems. The performance evaluation on the distribution system is considered on a modified IEEE 13-bus distribution system. The performance evaluation assessed the impact on the states and the resulting distribution locational marginal pricing (DLMPs).

1.3   Dissertation Outline

This dissertation is composed of seven chapters. This first chapter states the motivation for the presented work and outlines the dissertation's contributions. The second chapter presents the general background information about existing state estimation techniques, such as the weighted least squares, bad detection, and robust estimation techniques. Chapter 3 focuses on the power system modeling which is used throughout the dissertation. In the first part, bulk transmission power systems models are introduced. In the second part of the chapter, distribution modeling is discussed. Chapter 4 discusses the theory, design, and application of state estimators. This chapter describes the Unscented Kalman Filter (UKF) and the robust estimators paired with it for dynamic estimation.

Chapter 5 presents applications of the robust estimators to distribution systems and the resulting impact that measurement and topology FDI attacks cause. The effects on the states and the distribution locational marginal pricing are analyzed. Chapter 6 evaluates the proposed DSE applied to transmission systems in two formats: Centralized and distributed methods. In the first section, the estimators are used to a multi-machine centralized model of the IEEE 57- bus model and IEEE 118-Bus model. The impacts of FDI attacks on the centralized system are shown for both the IEEE 57-bus and 118-bus models. The root mean square error (RMSE) is evaluated for each estimator. In the second section, the decentralized or distributed DSE is implemented on islands to expand on the application of robust based DSE to large power systems. The considered systems are the IEEE 14-bus and 118-bus decomposed in small islands. Robust S- and MM-based DSE are executed in each island to track the dynamic and algebraic states, and the root mean squared error is calculated for each island, state, and estimator. Finally, Chapter 7 provides conclusions and presents additional topics for future work.

Chapter 2   Robust State Estimation in Power Systems

This chapter introduces the different types of estimators popular in the literature. The static state estimator is typical for the transmission systems operation and is executed, in practice, at regular intervals, i.e., from a few seconds to a few minutes. Cyber-security is becoming a significant concern and is discussed. The chapter introduces the proposed contributions, which are 1) implementing two high breakdown robust estimators (S- and MM-) to the static three-phase distribution state estimator and 2) implementing these robust estimators to the dynamic distributed state estimator at the transmission level.

2.1   Static and Hybrid Power System State Estimation

The most common approach to estimate the static state estimation (SSE) in the literature is the weighted least squares (WLS) [16], [26], [27]. The assumed accuracy of the measurements determines the weights. The SSE processes SCADA measurements and is an essential part of the control centers' EMS. The SCADA measurements are active/reactive power flows, active/reactive injections, and bus voltage magnitudes. The primary focus of state estimation is to deliver an accurate estimate of the designated states of an observable system. The first step to conducting a static SE process is to establish a model that relates the state variables, such as voltage and angle of the buses, to the measurements such as power flows and bus voltages for a given network configuration expressed in equation (2.1).

$$z = h(x) + v \tag{2.1}$$

where x is the n-dimensional state vector comprised of the system voltages and angles, the vector z is the m-dimensional measurement vector; h is the vector function relating measurements to the state variables known as the measurement function, and v is the measurement error vector. The error v is assumed to be Gaussian with a covariance matrix which is diagonal for independent measurements, R, of size m x m comprising the variance of the measurements given by $R_{i,i} = \sigma_i^2$. The WLS objective function $J(x)$ can now be formed as shown in equation (2.2):

$$J(x) = [z - h(x)]^T R^{-1} [z - h(x)] \tag{2.2}$$

where $[A]^T$ is the transpose row vector of the column vector A. Each error term in equation (2.2) includes a weight (inversely proportional to the error variance, generally σ_i^{-2}) that determines how each measurement influences the estimates. Thus, a measurement with a small error variance has a more significant weight since it is more accurate than a measurement with a large error. The state estimate $\hat{x}$ that minimizes $J(x)$ can be iteratively computed as follows [16].

$$G\Delta x = H^T R^{-1} (z - h(x^k)) \tag{2.3}$$

where $G = H^T R^{-1} H$ is the gain matrix, and H is the Jacobian of the measurement function $h(.)$ with respect to the state, i.e., $H = \frac{\partial h}{\partial x}$. After convergence, i.e., $|x^{k+1} - x^k| < \epsilon$, where ϵ is a chosen small number and $|.|$ is a vector norm, a solution of the WLS estimation problem gives the final state of the system. Once $\hat{x}$ is obtained, the respective residuals and the covariance of the state estimate error S can be calculated by (2.4) and (2.5):

$$r = z - \hat{z} = z - h(\hat{x}) \tag{2.4}$$

$$S = \left(H^T R^{-1} H\right)^{-1} \tag{2.5}$$

The covariance matrix T of the measurement estimate error, and the covariance of the residuals U are given by (2.6) and (2.7)

$$T = H S H^T \tag{2.6}$$

$$U = R - T \tag{2.7}$$

The power grid evolution is resulting in integrating more renewable generation, Internet IoT, and sensors such as PMUs. A widespread installment of PMUs has the potential to revolutionize the power system state-estimation (SE) process through their unique ability to measure synchronized phasors. PMUs [15], [28] have become popular to gather real-time information with GPS synchronized time stamps. The real-time information allows operators to obtain system awareness from the power system state estimation and operate, control, plan the power system [29]. With a sufficient number of PMUs, the state estimation problem becomes a simple linear estimation without any iteration [30], [31]. But, due to the high cost and secure communication infrastructure requirements associated with using PMUs for critical applications, the number of PMUs installed in a power system is still limited. There have been attempts to improve state estimation performance by combining PMU measurements with conventional measurements from SCADA. The merge of PMU measurement data with SCADA measurements in a hybrid state estimator may be sequential or integrated; researchers have preferred the sequential SE due to the re-usability of the energy management system (EMS) software [32].

2.1.1 Network Configuration

Within the power system, the physical connection of the individual components through circuit breakers, for example, is converted into a digital representation, a bus-branch model, to execute the SE algorithm. In the network topology data processing, the connectivity of the grid is determined, and the measurement availability (constant with the location of metering devices). Most topology studies concentrate on analyzing the related residuals given by an analysis of the topology and measurements

[9], [10], [33]–[35]. If a configuration error occurs, it should be corrected to avoid incorrect SE results. In critical cases, topology errors can be processed by the general state estimation(GSE) approach [35] where the state vector is augmented. With the deployment of phasor measurement units (PMUs), the strategic placement of phasor and conventional measurements to enhance the topology error processing capability has been studied [31].

2.1.2 *Observability Analysis*

Alongside network topology, observability of the power system is critical to the convergence and the feasibility of the SE. Observability constitutes an analytical way of checking whether a received set of measurements is sufficient to ensure the estimation of the system state. With this analytics, observable areas may be identified as well. If needed, pseudo-measurements such as forecasted values using statistical tools and virtual measurements such as zero power injections are used to reestablish full observability [13]. Network topology and measurement placement determine the observability analysis. There are two ways to approach the problem of observability. The first approach uses graph theory for segmenting the system into topological [9] graphs. The second one used numerical methods [36] involving the manipulation of matrices representing the topology. A simple test would be, for example, to check if the Jacobian of the measurement function with respect to the state is full rank [16].

2.1.3 *Detectability and Identifiability*

Data redundancy is a vital requisite for accurate or robust estimation and bad data detection. State estimation does not fulfill the critical role of handling corrupted measurements and network configuration errors when deprived of redundant measurements. Theoretically, the state estimation accuracy is also limited by the available number of measurements if these follow the assumed model. This implies that the state estimation ability to depict an accurate state of the system is dictated by the measurements providing observability, sufficient measurement redundancy, accuracy of sensors and a correct representation of the topology.

Within the measurement vector, the subset can be split into critical and non-critical measurements. The term critical refers to a measurement that cannot be discarded without the loss of observability, causing the non-convergence of the state estimation. In contrast, the redundant measurements provide a set in which a measurement may be used to recover the full observability of the system in response to a loss of a critical measurement. Additionally, the very same definition can be applied to a critical pair of measurements in which multiple measurements are influenced due to a single piece of bad data due to the system's topology. The primary issue when a pair of measurements is impacted by a single piece of bad data is that the occurrence of a large error in the targeted measurement is not detectable, and the relatable measurement pairs are detectable but not identifiable by the residual test. This means the

ability to identify which pair is corrupted becomes ambiguous with the residual test. This has been explored up to tuples of critical measurements in [37]–[40].

The difference in the received and the estimated measurements calculated in (2.4) are statistically checked to determine whether the estimation process can be considered accurate and whether errors follow the Gaussian assumption. When this hypothesis is tagged as a suspect using the chi-squared test [17], a residual analysis is performed to locate sources of the anomalies, remove the bad measurements, and re-execute the WLS. This is a crucial functionality of state estimation since it is responsible for the results' credibility.

2.1.4   Analysis of correlated residuals

Corrupted measurements may appear, for example, because of failures either in measurement devices or in the communication process of the collected data or false data injection (FDI) attacks. When corruption of the measurements occurs, the effects can come in many forms. Some bad data is easily detected since they represent gross errors that deviate so much from other measurements that they can be eliminated by simple plausibility checks such as the chi-squared test [41]. However, bad data from uncalibrated measuring instruments may not be large enough to do this. They may be considered ordinary by the model of the random errors established in equation (2.1). Most of the algorithms dedicated to the process of corrupted measurements are run after the estimation step. In the WLS estimator, detecting/identifying bad data is based on sound statistical principles, such as the normalized residual test in (2.8), where r is the residual vector and its relating covariance matrix U is obtained by equation (2.7). The standard deviation of the ith residual $r(i)$ is $\sigma_U(i) = \sqrt{U(I,I)}$ and $U(I,I)$ is the ith diagonal element of matrix U.

$$r_N(i) = r(i)/\sigma_U(i) \leq \text{threshold} \tag{2.8}$$

When the normalized residuals exceed the chosen threshold, which is generally set around 2 or 3 if the noise is Gaussian, there is a suspicion that this measurement is bad.

In the residual analysis, there are many possibilities for gross errors to become apparent, depending on: positions of corrupted measurement in the grid, type of measurements, how many measurements are spurious, and whether they are intentionally generated and coordinated by attackers. Fortunately, when a single bad data is present, the largest residual component corresponds to the spurious measurement. If it is not a critical measurement, it can be removed safely. Therefore, in a measurement system with adequate redundancy, a single bad data will be correctly detected/identified with a relatively low computational cost.

Conversely, the same does not happen in cases of multiple bad data since their identification could involve time-consuming combinatorial detection algorithms. The simplest case would require successive applications of the largest normalized residual (LNR) test because of the bad data smearing effect [42]. Bad data smearing impedes eliminating the corrupted measurements all at once. An outlier becomes clear to the LNR test after removing another outlier. The suspected measurements are successively removed as necessary until the LNR test becomes negative. This may require several identifications and elimination cycles.

2.2   Cyber-Security for State Estimation

When bad data is present in the measurement set, there is a common idea that spurious measurements should be detected and eliminated from the estimation. Detection could be more complex, difficult, and challenging if cyberattackers generated false data injection (FDI) attacks.

For example, an expert intruder could deliberately target specific measurements at carefully chosen measurement devices or substations. In this case, the residual analysis in the bad data detection module can fail to detect the attacked measurements, especially if the attacks are coordinated [43]. For example, the authors in [44] have shown that the attacker can generate stealthy FDI attacks with enough topology knowledge and access to sensors. FDI can corrupt measurements or the perceived topology of the system at the control center. While multiple measurement sensors can be faulty or corrupted, topology modification could have more severe consequences [11], [45]. Analyzing transmitted data and vulnerabilities of SE to cyberattacks has been a rapidly growing research area. Multiple types of cyberattacks such as FDI and denial of service (DoS) attacks are evaluated in [46].

The FDI attacks corrupt data communicated between remote terminal units (RTUs) and the control center. These FDI attacks can be in a few areas, either at the RTU, in transit through man-in-the-middle (MITM) attacks, or within the control center and can take a couple of forms. These forms are 1.) bad data within measurements from the RTU 2.) Topology attacks modify the represented physical system [10], [33]. DoS is also employed to block communications to the control center [47]. DoS attacks can be more critical than FDI attacks DoS cyberattacks could block all communications for the SE and force the operator to use historical pre-attack data if critical measurements are lost.

Various approaches have been proposed in the literature to protect the power system against FDI attacks. These include offline methods such as determining the location of sensors that would need extra security and protection [47], [48]. Other methods can be implemented online and are derived from statistical, signal processing approaches, and machine learning. The online techniques process the data to determine the suspicious measurements. An anomaly detection method for distribution systems

considering forecasted loads, pseudo-measurements, and synchrophasors has been proposed in [47]. Data-driven monitoring approaches [49]–[51] were considered for detecting FDI attacks targeting state estimation for distribution and transmission systems. Robust estimation theory has also been evaluated for the detection of FDI attacks in the literature [41], [52]–[54]. These robust estimation techniques develop resistant estimators that are optimal beyond the strict Gaussian assumption currently used within the power system. Robust estimators can detect/resist a maximum percentage of outliers called breakdown point [55]. Outliers which can the consequence of FDI attacks, are data points that do not follow the model of the majority of the data.

2.2.1 *Robust Estimation Theory Techniques*

While the WLS estimator is optimal with the Gaussian assumption, it is sensitive to departures from this assumption, and the presence of bad data can seriously degrade the estimation accuracy. Robust estimators for regression models were proposed to provide robustness against outliers and gross errors. M-estimators were introduced in the statistics literature by Huber [56]. Merrill and Schweppe [57] explored the application of M-estimators to power system state estimation to resist measurements outliers effectively. However, the performance of the M-estimators, including the least absolute value (LAV), becomes unreliable in the presence of gross errors on the regressors or topology affecting the estimate. Additionally, the Schweppe-Huber generalized M- (SHGM)[58], least absolute value (LAV) [17], [59], [60], least trimmed squares (LTS), and least median of squares (LMS) [61], [62] were proposed . SHGM, LTS, and LMS are robust estimators that can resist leverage points or outliers in the regressor matrix and can offer high breakdown points[63], [64]. These are caused by attacks or random errors in the topology caused by wrongly communicated states of circuit breakers or bad grid parameters such as line or transformer parameters. Conceptual and practical details on leverage points can be obtained in [16]. The LAV which is an estimator which minimizes the L_1 norm instead of L_2 such as the WLS of the measurement of the residuals. The LAV estimator can be executed by linear programming solvers and an detect outliers according to [59]. Adding a weighting scheme, the weighted-LAV (WLAV) is also one of the most common robust estimators with high performance and robustness [65]. The LMS minimizes the median of the squared residuals. The LMS has the disadvantage of poor efficiency if the measurements obey the model with Gaussian noise. The LTS minimizes the trimmed sum of the squared order statics errors. A detailed review of robust estimators is found in Rousseeuw and Leroy's book [55], Maronna and Yohai [25], Zoubir et al [66] and Huber [64].

2.3   Proposed Robust Distribution State Estimation

While state estimation is common at control centers for transmission systems, it is still limited for distribution systems. To adapt the SSE to distribution systems, additional considerations need to be taken into account [46], [67]. Primarily:

1.   High resistance to reactance r/x ratios

2.   Radial and meshed topologies

3.   Three phases and unbalance oriented

4.   Observability

5.   Cyber-security issues

Despite these challenges, distribution system state estimators are still being actively researched and explored. This interest increased with possible new sensors such as micro-PMUs and smart meters being installed and the need to operate the future active distribution system more efficiently with more integration of renewable and distributed generation. To observe the distribution systems, distribution management systems (DMS) collect measurements to support DSSE. Like transmission system networks, traditional measurements are communicated through RTUs. Due to the size of the power system, each RTU has its local time source; therefore, there may be a synchronization error when comparing measurements from different RTUs known as time skew. As the power system grows in complexity, so does the need for accurate real-time information.

Many essential issues in the distribution system state estimators development have been explored in previous literature [68], [69], including various models for 4-wire and 3-wire systems, which are analyzed for the implementation of distribution system state estimators. However, the application of robust estimators on distribution systems, especially for 4-wire topologies with low redundancy, has much room to grow.

Previously, robust estimators have been applied to distribution system state estimation for single phase systems. The prominent applications studied are WLS with bad detection based on the chi-squared test and the LNR scheme. In these past models, the estimators provided added robustness and resiliency to the system if bad data is present in the measurements. Recently, authors have evaluated robust estimators such as the LTS and LMS that could resist outliers on the topology [32]. The LTS and LMS can offer a high breakdown point. They tend to lack efficiency if their breakdown is increased.

This thesis implements high breakdown point S- and MM- estimators that could resist both measurement vectors and power system topologies errors in an unbalanced three-phase coupled distribution system. The MM- offers high efficiency when its high breakdown point is increased. The

S-estimator efficiency is improved by re-executing a WLS after detecting and rejecting outliers based on analyzing the S-estimation residuals.

2.4   Proposed Robust Distributed Dynamic State Estimator

The static state estimation gained interest over time and is applied in practice by control centers. Schweppe expected that the static state estimator could perform well in practice [1]–[3] and it has continually done so in real-world applications. However, the faster real-time dynamic state estimator has become an increasingly popular research topic. The term dynamic state estimation indicates that the estimator uses the previous measurement or estimated state and the current measurement in time [70]. The times are linked through a nonlinear function following the model. Recently, there have been efforts to define dynamic state estimation [20] and separate it from the nature of the evolution of the states. In power engineering, the "dynamic" term may be ambiguous as it typically means the oscillatory response of the power system with a transient period. These states could be evaluated using a forecasting-aided state estimator [8], which is effective for the slow time evolution of the states but is considered to be different from the DSE.

Many estimators have been implemented in terms of the classical static state estimation, as discussed previously. However, due to the advancing nature of the power system, the dynamic variables of a system are worth considering for a wide-area monitoring system [71]. Whether the DSE is a DC or AC [71], state estimators have been applied to small and large-scale power systems [21], [72]. Of these estimators, Kalman filters have retained much interest in dynamic power system state estimation. Kalman filters such as the Extended Kalman filter [22], Unscented Kalman filter [73], particle Kalman filters (PKF) [23], and ensemble Kalman filter (EnKF) [24] were proposed to implement DSE to the power system at a transmission level. The EKF can approximate the nonlinear dynamics by truncated Taylor series expansion via the Jacobian. The UKF, classified as a sigma point filter, approximates the nonlinear dynamics through sigma point projection which is explained in Chapter 4. The advantage of the UKF is that it does not require the calculation of the Jacobian as the EKF [19], [22]. and improves tracking accuracy for larger nonlinearities [74] Applications of the Kalman filters are explored in [74] with the application of a two-stage estimator and the LAV. Furthermore, the author in [75] implemented the robust GM- estimator to the dynamic power system simulation with projection statistics to offer robustness against measurement and topology errors. Furthermore, it is challenging to execute the DSE in a centralized fashion when the system becomes large. The idea is to run several DSE in parallel or in a distributed fashion to accelerate the execution time and simplify the tracking algorithm. Firstly the author in [76] provided substantial work in enhancing the observability of decentralized power systems while tracking states. Furthermore, the authors in [21] proposed such an approach by implementing an

EnKF. However, their work did not investigate the detection and correction of attacks on the measurements or topology.

This work considers implementing distributed high-breakdown robust S- and MM-based UKF filters to ensure dynamics state tracking while detecting outliers and FDI attacks. The DSEs are run in several islands to increase the number of attacks detected and accelerate the convergence time.

Chapter 3   Power System Model

This chapter reviews both transmission and distribution level modeling for the applications toward state estimation. Firstly, the multi-machine model dynamic equations used for transmission networks will be presented to enable the DSE implementation and evaluation. More specifically, the algorithm proposed in [73] was used to simulate the dynamics of the power system. The procedure is briefly explained in Section (3.1.1). The decentralized modeling considered is similar to the one presented in [21], [76], [77]. A brief overview is shown in section 3.1.3.

Secondly, the models used for distribution topology and power flow calculation are explained, the static robust distribution state estimation evaluation is executed using these models. For the power flow generation, OpenDSS [78] was used.

3.1   Transmission System Dynamics and Swing equation

The power system constantly evolves and grows with new interconnections of transmission networks and distributed generation components. As the power system evolves, the observed dimensionality related to the modeling of ordinary differential equations (ODEs) and the resulting complexity increases. Simplifications could be considered to satisfy specific needs such as available computational capacity to study and simulate the system. The classical synchronous machine model allows for studies such as transient stability and is helpful for large power systems interaction representation where the rotor dynamics and accelerating torque are included in the analysis. The accelerating torque is the difference between mechanical and electromagnetic torque. The swing equation is given in (3.1) in terms of mechanical and electromagnetic power [79].

$$M\frac{d^2\delta_m}{dt^2} + D\frac{d\delta_m}{dt} = P_m - P_G(\delta, \theta, V) \tag{3.1}$$

Where δ_m is the mechanical rotor angle of the rotating machine, M is the inertia constant of the generator, D is the damping constant of the generator, P_G is the per phase electrical power supplied by the generator and expressed in (3.2).

$$P_G(\delta, \theta, V) = \sum_{j=1}^{N}|V_i||V_j|\left(G_{ij}\cos(\delta_i - \theta_j) + B_{ij}\sin(\delta_i - \theta_j)\right) \tag{3.2}$$

Where G_{ij} and B_{ij} are the conductance and the susceptance between buses i and j, respectively. The voltage phasor at bus j has a phase angle θ_j and a magnitude V_j. N is the total number of system buses, G_{ij} and B_{ij} are 0 if there is no connection between a particular bus j and bus i. P_m is the mechanical power input to the generator. This mechanical power is assumed to be constant over the considered

analysis time intervals. The electrical power at the ith machine in (3.2) depends upon the mechanical rotor angle of the ith machine (δ_i) and the voltage and angle of the connected buses j.

The machine model considered through the dynamic simulation is presented in Figure 1 and equations (3.3) and (3.4). The synchronous machines are modeled by a constant E_d behind a transient reactance x_d' and the angle δ_I can vary. The loads are assumed to be constant impedances [80].
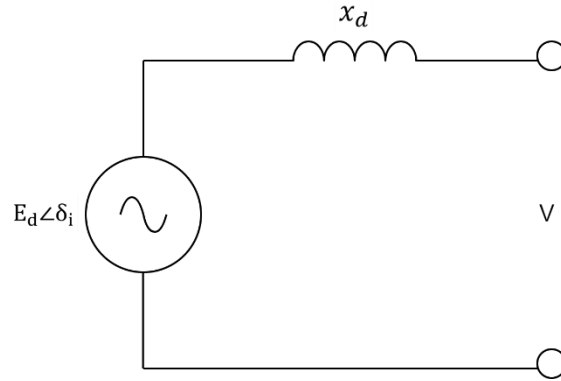
Figure 1:Synchronous generator model

Simplifying the equations above to a first-order system (3.3) and (3.4) may be found.

$$\dot{\delta}_i = \omega_i \tag{3.3}$$

$$\dot{\omega}_i = -\frac{D_i}{M_i}(\omega_i) + \frac{1}{M_i}\left(P_{M_i} - P_{G_i}(\theta, V)\right) \tag{3.4}$$

The index i indicates the ith generator. This model can be tracked by PMUs sampling at 30 samples per second or higher and following the IEEE Std C37.118.1a-2014 standard and following the IEEE Std C37.118.1a-2014 standard [81].

3.1.1 Multi-Machine Transmission System

The swing equation is evaluated by a numerical integration method such as the Euler or Runge-Kutta [73] to simulate the system's dynamic behavior. The following preliminary calculations are made.

1. The load impedances are calculated after executing a power flow in MATPOWER [82]. The admittance of the ith load bus with voltage V_{Li} and complex power $S_{Li} = P_{Li} + jQ_{Li}$, gives (3.6).

$$y_{Li} = \frac{P_{Li} - jQ_{Li}}{|V_{Li}|^2} \tag{3.6}$$

2. The generator internal voltages $E_i \angle \delta_i$ are given by equation (3.7)

$$E_i \angle \delta_i = V_{ai} + jx_{di} \frac{S_{gi}^*}{|V_{ai}|} = |V_{ai}| + jx_{di} \frac{(P_{gi} - jQ_{gi})}{|V_{ai}|} \tag{3.7}$$

The pre-disturbance terminal voltages $V_{ai} \angle \beta_i$ and the generator starts at an angle $\delta_i^0 = \delta_i + \beta_i$. The Y_{bus} matrices are updated depending on if the time is in the pre-fault, faulted, or postfault time interval.

In simulating the multi-machine transmission system, further reductions can be made to focus on the generators by taking advantage of the Kron reduction of the admittance matrix [81]. This reduction of the power system paired with the classical model allows for easier integration and analytics for the respective generators, where the bus voltage magnitudes and angles can be calculated as shown in (3.9). The injected current vector is linked to the voltage vector by:

$$I = Y_{bus}V \tag{3.9}$$

Injected currents are nonzero for the n-internal generator buses resulting in an injected current vector represented by (3.10)

$$I = \begin{bmatrix} I_n \\ \cdots \\ 0 \end{bmatrix} \tag{3.10}$$

The matrix Y_{bus} and vector V can be partitioned into two groups: generator buses and remaining buses as given in (3.11)

$$I = \begin{bmatrix} I_n \\ \cdots \\ 0 \end{bmatrix} = \begin{bmatrix} Y_{nn} & \vdots & Y_{ns} \\ \cdots & \cdots & \cdots \\ Y_{sn} & \vdots & Y_{ss} \end{bmatrix} \begin{bmatrix} E_n \\ \cdots \\ V_s \end{bmatrix} \tag{3.11}$$

The internal generator bus location is denoted by the subscript n, and the subscript s is used for all the remaining buses on the system. Y_{nn} is a diagonal matrix of inverted the generator impedances shown in (3.12).

$$Y_{nn} = \begin{bmatrix} \frac{1}{jx_d} & & & 0 \\ & \ddots & & \\ & & \ddots & \\ 0 & & & \frac{1}{jx_d} \end{bmatrix} \tag{3.12}$$

and also, the km'th element of Y_{ns} is (3.13).

$$Y_{nskm} = \begin{cases} \frac{-1}{jx_d} & \text{if } m = G_n \text{ and } k = n \\ 0 & \text{otherwise} \end{cases} \tag{3.13}$$

The injected current is related to the internal generator voltage by the matrix $\widehat{Y}$ in (3.14). Secondly, the matrix and Y_R in (3.15) is used to relate the bus voltages to the internal generator voltage in (3.16).

$$I_n = (Y_{nn} - Y_{ns}Y_{ss}^{-1}Y_{sn}) = \hat{Y}E_n \tag{3.14}$$

$$\hat{Y} = (Y_{nn} - Y_{ns}Y_{ss}^{-1}Y_{sn}) \tag{3.15}$$

$$Y_R = Y_{ss}^{-1}Y_{sn} \tag{3.16}$$

Above, the matrix $\hat{Y}$ is the reduced admittance matrix used for the multimachine simulations. It has dimensions (nxn) where n is the number of the generators in the system.

3.1.2   Transmission System Measurement Model

In using the matrices determined in the multi-machine section above, the admittance matrix may be utilized to calculate the desired measurements in the simulation. The reduced Y_{bus} matrix $\hat{Y}$ found in (3.15) is utilized to calculate the real and reactive power for each generation device such as a synchronous generator or condenser in (3.17) and (3.18) respectively.

$$P_{Gi} = Re(E_i I_i^*) \tag{3.17}$$

$$Q_{Gi} = Im(E_i I_i^*) \tag{3.18}$$

Voltages and phase angles for each bus on the system can be calculated by (3.19) and (3.20).

$$|V|_{Buses} = |Y_R \cdot E_i| \tag{3.19}$$

$$\theta_{Buses} = angle(Y_R \cdot E_i) \tag{3.20}$$

The resulting power flow calculations are given in (3.21)-(3.24).

$$P_i = \sum_{j=1}|V_i||V_j|(G_{ij}\cos\theta_{ij} + B_{ij}\sin\theta_{ij}) \tag{3.21}$$

$$Q_i = \sum_{j=1}|V_i||V_j|(G_{ij}\sin\theta_{ij} - B_{ij}\cos\theta_{ij}) \tag{3.22}$$

$$P_{ij} = G_{ij}(V_i)^2 - |V_i||V_j|(G_{ij}\cos(\theta_{ij}) + B_{ij}\sin(\theta_{ij})) \tag{3.23}$$

$$Q_{ij} = -V_i^2(B_{ij} + B_{ij}^{sh}) - |V_i||V_j|(-G_{ij}\sin(\theta_{ij}) + B_{ij}\cos(\theta_{ij})) \tag{3.24}$$

Where G_{ij} and B_{ij} are the real and imaginary parts of (i,j) element of the system Y_{bus} matrix. V_i is the voltage magnitude at bus i. V_j is the voltage magnitude at bus j. θ_{ij} is the voltage angle difference between at bus i and bus j.

3.1.3   Decentralized Dynamic Power System equations

The power system dynamics need to be modeled in islands to decentralize the power system dynamic state estimation. Variables are classified as dynamic and algebraic states or variables. This method aims

to isolate islands, decouple them, and estimate them individually. The adopted decentralized modeling is also presented in [21], [76], [77]. Equation (3.25) shows the combined state vector below.

$$x = \begin{bmatrix} x_d \\ x_a \end{bmatrix} = \begin{bmatrix} \delta \\ \omega \\ \theta \\ |V| \end{bmatrix} \text{ where } x_d = \begin{bmatrix} \delta \\ \omega \end{bmatrix} x_a = \begin{bmatrix} \theta \\ |V| \end{bmatrix} \tag{3.25}$$

The dynamic state is x_d while x_a indicates the algebraic states. $F_d(\cdot)$ represents the nonlinear differential equations for the dynamic states, $g(\cdot)$ contains the nonlinear algebraic equations and $h(\cdot)$ includes the power flow measurement equations. The general form of the differential-algebraic equations (DAE) is given in [21], [76], [77] and reproduced in the following equations.

$$\begin{cases} \dot{x}_d = F_d(x_d, x_a) \\ 0 = g(x_d, x_a) \\ z = h(x_d, x_a) \end{cases} \tag{3.26}$$

$$\begin{cases} \dfrac{d\delta}{dt} = 2\pi f_0(\omega - 1) \\ \dfrac{d\omega}{dt} = \dfrac{1}{M_i}\left[P_m - P_g - D_i(\omega - 1)\right] \\ 0 = P_g - P_j(\delta, \theta, |V|) \\ 0 = Q_g - Q_j(\delta, \theta, |V|) \\ P_{inj}(i) = \sum_{j=1}^{N}|V_i||V_j|\left(G_{ij}\cos\theta_{ij} + B_{ij}\sin\theta_{ij}\right) \\ Q_{inj}(i) = \sum_{j=1}^{N}|V_i||V_j|\left(G_{ij}\sin\theta_{ij} - B_{ij}\cos\theta_{ij}\right) \end{cases} \tag{3.27}$$

The first two terms in (3.27) are dynamic differential equations related to rotor angle and speed of synchronous machines, i.e, $F_d(x_d, x_a)$. The remaining equations are algebraic. The next equations give the generators real and reactive power equations $g(x_d, x_a)$ and last two equations give injections of the buses $h(x_d, x_a)$.

As discussed in [77], [83], $g_{x_a}(x_d, x_a)$ has a solution for x_a and a non-zero determinant $\det(g_{x_a}(x_d, x_a)$. One can obtain (3.28), the partial derivative of g with respect to x_a is $g_{x_a}(x_d, x_a) = \partial g(x_d, x_a)/\partial x_a$ and the partial derivative of g with respect to x_d is denoted by $g_{x_d}(x_d, x_a)$

$$\begin{cases} g_{x_d}(x_d, x_a)\dfrac{dx_d}{dt} + g_{x_a}(x_d, x_a)\dfrac{dx_a}{dt} = 0 \\ g_{x_d}(x_d, x_a)F_d(x_d, x_a) + g_{x_a}(x_d, x_a)\dfrac{dx_a}{dt} = 0 \end{cases} \tag{3.28}$$

The ODE and the measurements are given by (3.29) in (3.30):

$$\frac{dx}{dt} = \begin{bmatrix} \dot{x}_d \\ \dot{x}_a \end{bmatrix} = \begin{bmatrix} F_d(x_d, x_a) \\ -g_{x_a}(x_d, x_a)^{-1}g_{x_d}(x_d, x_a)F_d(x_d, x_a) \end{bmatrix} \tag{3.29}$$

$$z = h(x_d, x_a) = \begin{bmatrix} g(x_d, x_a) \\ h(x_a) \end{bmatrix} \tag{3.30}$$

In expanding the ODE, additional simplifications may be made to apply the system of equations in a distributed solution to which the authors in [76], [77] refer to it as a decoupled approach.

$$g_{x_a}(x_d, x_a) = \frac{\partial g(x_d, x_a)}{\partial x_a} = \begin{pmatrix} g_{x_a 1} & g_{x_a 2} \\ g_{x_a 3} & g_{x_a 4} \end{pmatrix} \cong [J] = \begin{pmatrix} j_1 & j_2 \\ j_3 & j_4 \end{pmatrix} \tag{3.31}$$

$$g_{x_a 1} = \frac{\partial P}{\partial \theta} = P_\theta \quad g_{x_a 2} = \frac{\partial P}{\partial V} = P_V \quad g_{x_a 3} = \frac{\partial Q}{\partial \theta} = Q_\theta \quad g_{x_a 4} = \frac{\partial Q}{\partial V} = Q_V \tag{3.32}$$

The matrices $g_{x_a 2}$ and $g_{x_a 3}$ can be neglected as in (3.33)

$$g_{x_a 2} = 0 \quad g_{x_a 3} = 0 \tag{3.33}$$

The equation (3.34) relates the change in the angles and voltages in the system to the change in the generators' angle and power in (3.35) and (3.36).

$$[\Delta x_a(n)] = \begin{bmatrix} \Delta\theta(n) \\ \Delta V(n) \end{bmatrix} = -g_{x_a}(x_d, x_a)^{-1} g_{x_d}(x_d, x_a) \begin{bmatrix} \Delta\delta(n) \\ \Delta P(n) \end{bmatrix} \tag{3.34}$$

$$\Delta\delta(n) = \omega - \omega_s \tag{3.35}$$

$$\Delta P(n) \approx P_M(n) - P_g(n) \tag{3.36}$$

$$g_{x_a}(x_d, x_a) = \frac{\partial g(x_d, x_a)}{\partial x_a} = \begin{pmatrix} g_{x_a 1} & 0 \\ 0 & g_{x_a 4} \end{pmatrix} \cong [J] = \begin{pmatrix} j_1 & 0 \\ 0 & j_4 \end{pmatrix} \tag{3.37}$$

The fast decentralized method commonly seen in power system analysis [77], as shown below in (3.38)-(3.39) [84].

$$\Delta\theta = [j_1]^{-1}[\Delta P] \tag{3.38}$$

$$\frac{\Delta V}{V} = [j_4]^{-1}[\Delta Q] \tag{3.39}$$

One step further provides us with the simplified equations used in the decentralized method in (3.40) and (3.41) where B' and B'' are j_1 and j_4 respectively.

$$\Delta\theta = [B']^{-1}[\Delta P] \tag{3.40}$$

$$\Delta V = [B'']^{-1} \begin{bmatrix} \frac{\Delta Q}{V} \end{bmatrix} \tag{3.41}$$

This decentralized method is proposed to allow the decomposition of the power system into smaller subsections and decentralize the dynamic state estimation. The system is decomposed into islands, as noted in [21], and the dynamic state estimation is executed for each island. It is assumed that the islands are observable. The tie-lines and boundary buses of the system are defined as:

- The internal bus is fully included on the considered island without connection to other external boundary buses.
- The internal boundary bus of a considered island has a connection with an external boundary bus.
- The external boundary bus is a bus that belongs to another island and connects to an internal boundary bus through a tie-line.
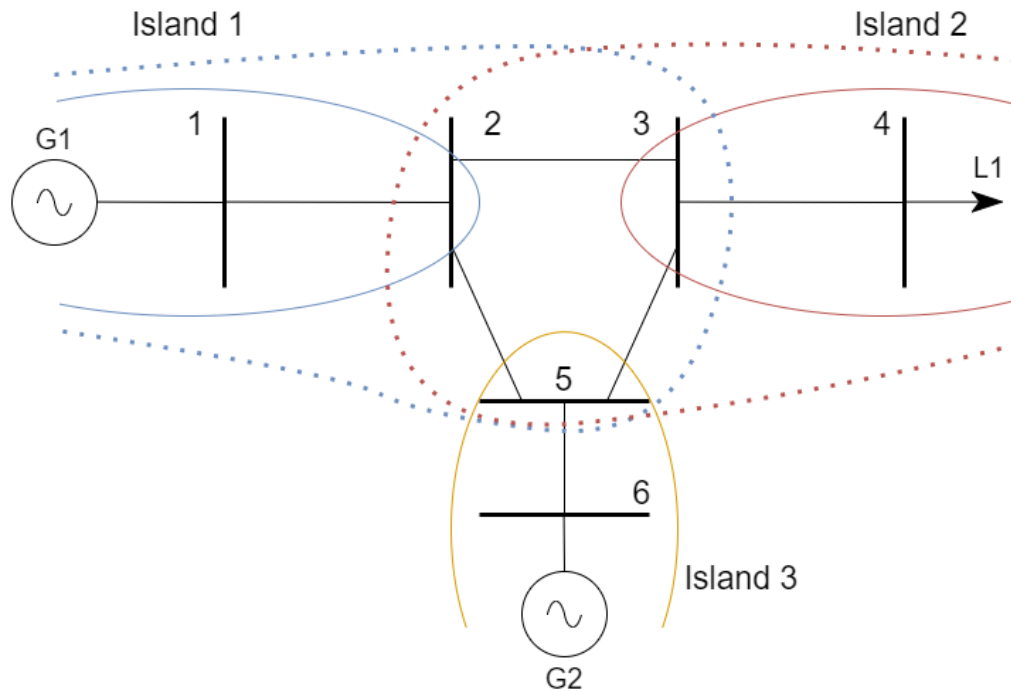
Figure 2: Island designation by external and internal nodes

For example, in Figure 2, the internal buses included in Island 1 are buses 1 and 2. In expanding to the external network, Area 1 includes external boundary buses 3 and 5. Therefore, in the state estimation of the system, Island 1 includes buses 1,2,3,5 and generator 1. The inclusion of generator 1 makes this a dynamic island. Island 3 is also a dynamic island, containing internal buses 5 and 6 and external buses 2 and 3. The system needs to be modular enough to incorporate islands with dynamic equations such as generators and algebraic islands. Islands will be classified as either *Dynamic* or *Algebraic*. In

observing island 2, the internal buses are 3 and 4, where there is no generator attached to these internal buses. Therefore, Island 2 is classified as an algebraic island.

In developing the sub-system model with our two island types, the proposed *dynamic* power system model can be noted as seen above and re-iterated below in equations (3.42) – (3.47);

$$x_l = \begin{bmatrix} x_d \\ x_a \end{bmatrix} = \begin{bmatrix} \delta_l \\ \omega_l \\ \theta_l \\ |V|_l \end{bmatrix} = \begin{bmatrix} \delta_{l-internal} \\ \delta_{l-external} \\ \omega_{l-internal} \\ \omega_{l-external} \\ \theta_{l-internal} \\ \theta_{l-external} \\ |V|_{l-internal} \\ |V|_{l-external} \end{bmatrix} \tag{3.42}$$

$$\begin{cases} \dot{x}_d = F_d(x_d, x_a) \\ 0 = g(x_d, x_a) \\ z = h(x_d, x_a) \end{cases} \tag{3.43}$$

$$\begin{cases} \dfrac{d\delta}{dt} = 2\pi f_0(\omega - 1) \\ \dfrac{d\omega}{dt} = \dfrac{1}{M_i}\left[P_m - P_g - D_i(\omega - 1)\right] \\ P_g - P_j(\delta, \theta, |V|) = 0 \\ Q_g - Q_j(\delta, \theta, |V|) = 0 \\ P_{inj}(i) = \sum_{j=1}^{N}|V_i||V_j|\left(G_{ij}\cos\theta_{ij} + B_{ij}\sin\theta_{ij}\right) \\ Q_{inj}(i) = \sum_{j=1}^{N}|V_i||V_j|\left(G_{ij}\sin\theta_{ij} - B_{ij}\cos\theta_{ij}\right) \end{cases} \tag{3.44}$$

If an algebraic island is selected for estimation, the system of equations is reduced to remove the dynamic equations such as noted in (3.45)-(3.47);

$$x_l = [x_a] = \begin{bmatrix} \theta_l \\ |V|_l \end{bmatrix} = \begin{bmatrix} \theta_{l-internal} \\ \theta_{l-external} \\ |V|_{l-internal} \\ |V|_{l-external} \end{bmatrix} \tag{3.45}$$

$$\begin{cases} 0 = g(x_d, x_a) \\ z = h(x_d, x_a) \end{cases} \tag{3.46}$$

$$\begin{cases} P_g - P_j(\delta, \theta, |V|) = 0 \\ Q_g - Q_j(\delta, \theta, |V|) = 0 \\ P_{inj}(i) = \sum_{j=1}^{N}|V_i||V_j|\left(G_{ij}\cos\theta_{ij} + B_{ij}\sin\theta_{ij}\right) \\ Q_{inj}(i) = \sum_{j=1}^{N}|V_i||V_j|\left(G_{ij}\sin\theta_{ij} - B_{ij}\cos\theta_{ij}\right) \end{cases} \tag{3.47}$$

These equations are subject to change as determined by the topology of each island. The dynamic vector is chosen depending on the internal topology as well as the external topology. If an external boundary bus includes a generator, that generator's power flow is included in the dynamic equations, as subsequently is estimated in the state variables.

3.2 Distribution System Modeling

The most fundamental difference between standard transmission system-level modeling and distribution system modeling is the inherently unbalanced nature of distribution systems. This unbalance in distribution systems stems from their configurations such as three-phase, two-phase, single-phase both in possible overhead and underground lines, resulting in differing power flows on different feeders [85], [86]. This unbalance of the distribution system is modeled by the admittance matrix, however, expanded to reflect each phase of the system at each location. Commonly, Carson's equations are used to calculate the self and mutual impedances of the lines shown in (3.48) and (3.49) [85]. Where r_I is the conductor resistance in $\Omega/_{mile}$ GMR_I is the Geometric Mean Radius of conductor i in feet and D_{ij} is the Distance between conductors i and j in feet.

$$Z_{ii} = r_i + 0.09530 + j0.12134\left(\ln\frac{1}{GMR_i} + 7.93402\right) \Omega/_{mile} \tag{3.48}$$

$$Z_{ij} = 0.09530 + j0.12134\left(\ln\frac{1}{D_i} + 7.93402\right) \Omega/_{mile} \tag{3.49}$$

Equations (3.48) and (3.49) can be used to create the $Z_{primitive}$ the matrix found in (3.50), where the phases and the neutral n are included. These phases are mutually coupled, and therefore the $Z_{primitive}$ will result in a 4x4 matrix due to the neutral phase.

$$\left[Z_{primitive}\right] = \begin{bmatrix} Z_{aa} & Z_{ab} & Z_{ac} & \vdots & Z_{an} \\ Z_{ba} & Z_{bb} & Z_{bc} & \vdots & Z_{bn} \\ Z_{ca} & Z_{cb} & Z_{cc} & \vdots & Z_{cn} \\ \dots & \dots & \dots & \dots & \dots \\ Z_{na} & Z_{na} & Z_{na} & \vdots & Z_{nn} \end{bmatrix} = \begin{bmatrix} Z_{ij} & Z_{in} \\ Z_{nj} & Z_{nn} \end{bmatrix} \tag{3.50}$$

In most applications, the primitive impedance matrix in (3.51) is reduced to a 3x3 matrix by reducing the neutral phase. Using Kron [87] reduction   reduces the $Z_{primitive}$ matrix into the Z_{abc} phase impedance matrix. The Kron reduction equation for the impedance matrix is shown in (3.54).

$$[Z_{abc}] = [Z_{ij}] - [Z_{in}] \cdot [Z_{nn}]^{-1} \cdot [Z_{nj}] = \begin{bmatrix} Z_{aa} & Z_{ab} & Z_{ac} \\ Z_{ba} & Z_{bb} & Z_{bc} \\ Z_{ca} & Z_{cb} & Z_{cc} \end{bmatrix} \quad \Omega/_{mile} \tag{3.51}$$

For a non-transposed distribution line, the diagonal terms are not be equal, nor are the off-diagonal terms. The matrix is still symmetrical. Similarly, the shunt admittance of a line is composed of the conductance and the susceptance. The capacitance results from the potential difference between conductors since charged conductors create an electric field outwards from their center [88]. The method of conductors and their images is used in the process to calculate the shunt capacitance and admittance [88]. This process is similar to Carson's equations above, where equations (3.52) and (3.53) are used to determine the self and mutual potential coefficients.

$$P_{ii} = 11.17689 \cdot \ln\frac{S_{ii}}{RD_i} \; \text{mile}\big/_{\mu F} \tag{3.52}$$

$$P_{ij} = 11.17689 \cdot \ln\frac{S_{ii}}{D_{ij}} \; \text{mile}\big/_{\mu F} \tag{3.53}$$

Where S_{ii} is the distance from conductor i to its image in feet. S_{ij} is the distance from conductor i to the image of conductor j in feet. RD_I is the radius of the conductor i in feet. D_{ij} is the distance from conductor i to conductor j in feet.

For overhead lines, the primitive potential coefficient matrix $[P_{primitive}]$ is formed. In four-wire grounded wye lines, the primitive matrix is given by (3.54). The phases of the system and the neutral are included.

$$[P_{primitive}] = \begin{bmatrix} P_{aa} & P_{ab} & P_{ac} & \vdots & P_{an} \\ P_{ba} & P_{bb} & P_{bc} & \vdots & P_{bn} \\ P_{ca} & P_{cb} & P_{cc} & \vdots & P_{cn} \\ \dots & \dots & \dots & \dots & \dots \\ P_{na} & P_{na} & P_{na} & \vdots & P_{nn} \end{bmatrix} \tag{3.54}$$

Since the neutral is grounded, Kron reduction is applied once again to produce the phase potential matrix P_{abc} with dimensions dictated by the amount of phases. similar to the admittance matrix reduction above shown below in (3.55).

$$[P_{abc}] = [P_{ij}] - [P_{in}] \cdot [P_{nn}]^{-1} \cdot [P_{nj}] \tag{3.55}$$

The inverse of the matrix P_{abc} will give the capacitance matrix C_{abc} as shown in (3.56).

$$[C_{abc}] = [P_{abc}]^{-1} \tag{3.56}$$

Equation (3.57) provides the admittance where the shunt conductance has been neglected, f is the frequency of the system.

$$[C_{abc}] = 0 + j2\pi f \cdot [C_{abc}]\frac{\mu S}{\text{mile}}. \tag{3.57}$$

3.3 Distribution System Measurement Model

The measurements of the distribution system are modeled using the system states $V_i^{a,b,c}$ $\theta_i^{a,b,c}$ where $i = 1,2\cdots,n$ and the values from the Y_{bus} matrix.

3.3.1 Power Injection Measurements

The real and reactive power injections at bus i phase ph can be written in equations (3.58) and (3.59) [85], [86].

$$P_i = V_i^{ph} \sum_{p\in\Phi} \sum_{j=1}^{n} V_j^p \left(G_{ij}^{ph,p} \cos\left(\theta_i^{ph} - \theta_j^p\right) + B_{ij}^{ph,p} \sin\left(\theta_i^{ph} - \theta_j^p\right)\right) \tag{3.58}$$

$$Q_i = V_i^{ph} \sum_{p\in\Phi} \sum_{j=1}^{n} V_k^p \left(G_{ij}^{ph,p} \sin\left(\theta_i^{ph} - \theta_j^p\right) - B_{ij}^{ph,p} \cos\left(\theta_i^{ph} - \theta_j^p\right)\right) \tag{3.59}$$

Where $G_{ij}^{ph,p}$ and $B_{ij}^{ph,p}$ are the real and imaginary parts of (i,j) element of the system Y_{bus} matrix between phases ph and p. V_i^{ph} is the voltage magnitude at bus i phase ph (eg A.), V_j^p is the voltage magnitude at bus j at phase p, which belongs to the set Φ composed by the phases a,b and c. θ_i^{ph} is the voltage angle at bus i phase ph, θ_j^p is the voltage phase angle at bus j phase p.

3.3.2 Power Flow Measurements

The real and reactive power flow from bus i to bus j can be written as given in equations (3.60) and (3.61). Equation (3.62) provides the line charging susceptance, where the susceptance includes the self susceptance B_{ij}^{sh} and coupled susceptance $B_{ij}^{sh,ph,p}$ between phases ph and p [86].

$$P_{ij} = V_i^{ph} \sum_{p\in\Phi} V_j^p \left(G_{ij}^{ph,p} \cos\left(\theta_i^{ph} - \theta_j^p\right) + B_{ij}^{ph,p} \sin\left(\theta_i^{ph} - \theta_j^p\right)\right) -$$
$$V_i^{ph} \sum_{p\in\Phi} V_i^p \left(G_{ij}^{ph,p} \cos\left(\theta_i^{ph} - \theta_j^p\right) + B_{ij}^{rph,p} \sin\left(\theta_i^{ph} - \theta_j^p\right)\right)$$

$$\tag{3.60}$$

$$Q_{ij} = V_i^{ph} \sum_{p\in\Phi} V_j^p \left(G_{ij}^{ph,p} \sin\left(\theta_i^{ph} - \theta_j^p\right) - B_{ij}^{ph,p} \cos\left(\theta_i^{ph} - \theta_j^p\right)\right) -$$
$$V_i^{ph} \sum_{p\in\Phi} V_i^p \left(G_{ij}^{ph,p} \sin\left(\theta_i^{ph} - \theta_j^p\right) - B_{ik}^{rph,p} \cos\left(\theta_i^{ph} - \theta_j^p\right)\right)$$

$$\tag{3.61}$$

$$B_{ij}^{rph,p} = B_{ij}^{ph,p} + B_{ij}^{sh} \cdot B_{ij}^{sh,ph,p} \tag{3.62}$$

3.3.3   Measurement Jacobian Matrix

The Jacobian matrix of the power system can be formed by the partial derivatives of the measurements with respect to the system states, as shown in equations (3.63) and (3.64). Due to the inclusion of µPMUs, voltage phasors are also included in the measurement matrix. Such that, these measurements are power injections, flows, voltage magnitude, and voltage angle. However, in noting the difference between transmission and distribution systems, the Jacobian is between phases.

$$[H] = \frac{\partial h(x)^T}{\partial x} \tag{3.63}$$

$$H(x) = \begin{bmatrix} \dfrac{\partial P_i^{a,b,c}}{\partial \theta_i^{a,b,c}} & \dfrac{\partial P_i^{a,b,c}}{\partial \theta_j^{a,b,c}} & \dfrac{\partial P_i^{a,b,c}}{\partial V_i^{a,b,c}} & \dfrac{\partial P_i^{a,b,c}}{\partial V_j^{a,b,c}} \\[2ex] \dfrac{\partial Q_i^{a,b,c}}{\partial \theta_i^{a,b,c}} & \dfrac{\partial Q_i^{a,b,c}}{\partial \theta_j^{a,b,c}} & \dfrac{\partial Q_i^{a,b,c}}{\partial V_i^{a,b,c}} & \dfrac{\partial Q_i^{a,b,c}}{\partial V_j^{a,b,c}} \\[2ex] \dfrac{\partial P_{ij}^{a,b,c}}{\partial \theta_i^{a,b,c}} & \dfrac{\partial P_{ij}^{a,b,c}}{\partial \theta_j^{a,b,c}} & \dfrac{\partial P_{ij}^{a,b,c}}{\partial V_i^{a,b,c}} & \dfrac{\partial P_{ij}^{a,b,c}}{\partial V_j^{a,b,c}} \\[2ex] \dfrac{\partial Q_{ij}^{a,b,c}}{\partial \theta_i^{a,b,c}} & \dfrac{\partial Q_{ij}^{a,b,c}}{\partial \theta_j^{a,b,c}} & \dfrac{\partial Q_{ij}^{a,b,c}}{\partial V_i^{a,b,c}} & \dfrac{\partial Q_{ij}^{a,b,c}}{\partial V_j^{a,b,c}} \\[2ex] 0 & 0 & \dfrac{\partial V_i^{a,b,c}}{\partial V_i^{a,b,c}} & 0 \\[2ex] 0 & 0 & 0 & \dfrac{\partial V_j^{a,b,c}}{\partial V_j^{a,b,c}} \end{bmatrix} \tag{3.64}$$

3.3.4   Distribution System Reference Bus

Due to the multi-phase modeling of the distribution system, the selection of a reference bus becomes an important task. As denoted in [85], the author evaluates a few different applications of reference bus selection and importantly notes that arbitrarily assigning a balanced bus as the reference will yield biased and/or incorrect solutions. In summarizing, the three avenues were compared in [85] are as follows:

1. Assuming an existing bus with balanced three-phase voltage
2. Using the angle of one phase as the reference
3. Using a three-phase virtual bus reference

In this work, method 2, an angle of one of the phases, has been used as a reference, which was assumed to be a PMU measurement. This could be designated as the substation location on Phase A, B, or C. This method allows for the other two phases to converge to the angles dictated by the measurements and estimation method. In terms of building the Jacobian of the system, only one column is removed as only one reference value is selected, similar to positive sequence reference bus selection.

Consequently, with the removal of this column, the possibility of a singular Jacobian matrix becomes possible. Having a non-solvable system is due to the nature of the measurements and selected states, such as the voltage magnitude and angle. If the measurement is only comprised of voltage magnitudes and angles, then the Jacobian would not be full rank due to the removal of the reference node column in the Jacobian matrix. Therefore, power flow and power injection equations allow enough redundancy to keep the system observable. The Jacobian matrix should be overdetermined and full rank to ensure observability.

Chapter 4   Dynamic Robust State Estimators

Since Schweppe et al proposed power state estimators [1]–[3], there have been numerous contributions based on the classic WLS algorithms. Dynamic state estimators will be employed to track the states of the power system with higher PMU data rates. The DSE enables monitoring and control functions in wide-area monitoring systems (WAMS). The EKF, UKF, and CKF have been proposed in the recent literature [20], [89]. In this chapter, the Unscented Kalman filter, and its representation in batch mode regression will be introduced and implemented as the base estimator proposed in the dynamic state estimation algorithms. Furthermore, the robust estimators used to enhance resiliency are discussed. One advantage of the UKF consists of not requiring the calculation of a Jacobian at each time step k [90] like the EKF, the filter can be easily applied to many different applications. It is also reported that the UKF has higher performance when the nonlinearities in the state-space representation increase [90].

4.1   Unscented Kalman Filter

To estimate the states of the power system components the discrete nonlinear process model is considered [90]. The state-space representation is given by:

$$x_k = F(x_{k-1}, u_{k-1}) + w_{k-1} \tag{4.1}$$

$$y_k = H(x_k, u_k) + v_k \tag{4.2}$$

$$w_k \sim N(0, Q_k) \qquad Q_k = \text{cov}\{w_k\} = E\{w_k \cdot w_k^T\} \tag{4.3}$$

$$v_k \sim N(0, R_k) \qquad R_k = \text{cov}\{v_k\} = E\{v_k \cdot v_k^T\} \tag{4.4}$$

The state is the vector x_k of dimension n, u_k is the system input vector and y_k is the measurement vector of dimension m. The functions $F()$ and $H()$ are nonlinear and assumed to be continuous, w_k is the process noise sequence and v_k is the observation (measurement) noise sequence. Noise is assumed to be Gaussian (following a normal distribution) with zero mean and known time-invariant covariance matrices $Q_k = Q$ and $Q_k = R$. The objective of the filters is to recursively estimate x_k from the collected measurements y_k. This means calculating estimates of x_k at time *k,* given the $y_{1,...,}y_k$ values up to time k. Using the assumption that the initial state vector $(x_0|y_0)$ is known, $(x_k|y_k)$ is obtained recursively in a two-step process: prediction step and update or correction step using the non-linear equations $x = F(x)$ and $y = H(x)$ respectively.

The Unscented Kalman filter has been applied to track or filter the state from the measurements. The filter predicts the next state using the so-called sigma points. These points are propagated through the

nonlinear function F to deliver the prediction of the states. For calculating the statistics of a random variable that undergoes a nonlinear transformation, the unscented transformation is used [90].

To understand the calculation of the sigma points, consider a variable x (dimension n) propagated through a nonlinear function $y = f(x)$. The mean of x can be calculated by (4.5), and the covariance of x is calculated by (4.6).

$$\bar{x} = E\{x\} \tag{4.5}$$

$$P_x = E\{(x - \bar{x}) * (x - \bar{x})^T\} \tag{4.6}$$

To calculate the statistics of y, a matrix ψ of $2 * n + 1$ sigma vectors is formed per (4.7) – (4.9).

$$\psi_0 = \bar{x} \tag{4.7}$$

$$\psi_i = \bar{x} + \gamma\left(\sqrt{P_x}\right)_i \quad i = 1, \cdots, n \tag{4.8}$$

$$\psi_i = \bar{x} - \gamma\left(\sqrt{P_x}\right)_i \quad i = n + 1, \cdots, 2 * n \tag{4.9}$$

Where (4.10) is a scaling parameter and (4.11) depends on the constant α which determines the spread of the sigma points around the mean value $\bar{x}$.

$$\gamma = \sqrt{n + \lambda} \tag{4.10}$$

$$\lambda = \alpha^2 * (n + k_f) - n \tag{4.11}$$

The constant k_f is a secondary scaling parameter and is set to 0 for state estimation. A note can be made that is the ith column of the matrix square root denoted by $\left(\sqrt{P_x}\right)_i$, may also be described through the Cholesky factorization method. The ψ_i vectors are propagated through the nonlinear function $y_i = f(\psi_i)$. The mean and covariance for y are calculated by a weighted sample mean and covariance of the posterior sigma points y_i, where the weights are given in equations (4.12) to (4.14):

$$W_0^{(m)} = \frac{\lambda}{(n+\lambda)} \tag{4.12}$$

$$W_0^{(c)} = \frac{\lambda}{(n+\lambda)} + (1 - a^2 + \beta) \tag{4.13}$$

$$W_i^{(m)} = W_i^{(c)} = \frac{1}{2*(n+\lambda)} i = 1, \cdots, 2 * n \tag{4.14}$$

As stated above, the UKF filter has two main portions, the prediction step and the correction or update step. Below is the main UKF state estimation algorithm, with additive (zero mean) noise [90]:

4.1.1 Initialization Step

The initial estimated state vector $\hat{x}_0 = \widetilde{x_0}$ and covariance $P_0 = \widetilde{P_{x,0}}$ by estimates of the expected value and covariance of x_0.

Sigma point calculation for k>=1

$$\chi_{k-1}^i = \left[\hat{x}_{k-1} \pm \gamma * \left(\sqrt{P_{k-1}}\right)\right] \tag{4.15}$$

4.1.2 Prediction Step

For the prediction step, a transformation of the sigma points through the state-update function (4.16) is made. The predicted state estimate (4.18) and its covariance (4.19) are then calculated, where the weights $W_i^{(m)}$ and $W_i^{(c)}$ are defined by equations (4.12) to (4.14).

$$\chi_k^{i,-} = f(\chi_{k-1}^i) \tag{4.16}$$

$$\hat{x}_k^- = \sum_{i=1}^{2n} w_i \chi_{k-1}^{i,-} \tag{4.18}$$

$$P_{x,k}^- = \sum_{i=1}^{2n} w_i \left(\chi_k^{i,-} - \hat{x}_k^-\right)\left(\chi_k^{i,-} - \hat{x}_k^-\right)^T + Q_{k-1} \tag{4.19}$$

4.1.3 Measurement Update

Similar to the predicting step, a transformation of the sigma points through the measurement-update function found in equation (4.12) will be made. And the covariance of the measurements can be made in (4.21).

$$\hat{z}_k^- = \sum_{i=1}^{2n} w_i \chi_{k,*}^{i,-} \tag{4.20}$$

$$P_{z,k}^- = \sum_{i=1}^{2n} w_i \left(\chi_{k,*}^{i,-} - \hat{z}_k^-\right)\left(\chi_{k,*}^{i,-} - \hat{z}_k^-\right)^T + R_k \tag{4.21}$$

Calculate the cross-covariance

$$P_{xz,k}^- = \sum_{i=1}^{2n} w_i \left(\chi_k^{i,-} - \hat{x}_k\right)\left(\chi_{k,*}^{i,-} - \hat{z}_k\right)^T \tag{4.22}$$

Calculate the Kalman filter gain vector:

$$K_k = P_{xz,k}^- \left(P_{z,k}^-\right)^{-1} \tag{4.23}$$

Finally, calculate the estimated corrected state and its covariance by the standard Kalman filter algorithm in (4.24) and (4.25)

$$\hat{x}_k = \hat{x}_k^- + K_k(y_k - \hat{y}_k^-) \tag{4.24}$$

$$P_k = P_k^- - K_k P_{y_k y_k} K_k^T \tag{4.25}$$

4.1.3.1   Batch Mode Regression

Several authors have represented the UKF in its batch mode-regression [75]. This representation is useful to get the corrected state. For example, a WLS estimator applied to the batch-mode regression will give an equivalent to the UKF. This representation is most beneficial to offer robustness if existing robust regression estimators are applied. By applying a statistical linearization to the nonlinear system process model, the predictions and observations may be processed simultaneously [75].

The prediction error is $\Delta_x = x_k - \hat{x}_k^-$ where x_k is the true state; τ_k is the linearization error, and equation (4.26) provides the covariance of the prediction state error estimated by (4.19). The cross covariance matrix of $P_{xz,k}^-$ determined by the UKF in (4.22). These covariance matrices give the matrix H_k which is no longer the Jacobian martrix.

$$E[\Delta_x \Delta_x^T] = P_{x,k}^- \tag{4.26}$$

$$H_k = \left(P_{xz,k}^-\right)^T \left(P_{x,k}^-\right)^{-1} \tag{4.27}$$

The batch-mode regression form is shown in (4.28). I_k is an identity matrix.

$$\begin{bmatrix} z_k + H_k \hat{x}_k^- + \hat{z}_k^- \\ \hat{x}_k^- \end{bmatrix} = \begin{bmatrix} H_k \\ I_k \end{bmatrix} x_k + \begin{bmatrix} v_k + \tau_k \\ \Delta_x \end{bmatrix} \tag{4.28}$$

equation (4.27) may be rewritten in the compact equation (4.30)

$$\tilde{z}_k = \underline{H}_k x_k + \underline{e}_k \tag{4.29}$$

$$\underline{S}_k = E\left[\underline{e}_k \underline{e}_k^T\right] = \begin{bmatrix} R_k + R_l & 0 \\ 0 & P_k^- \end{bmatrix} \tag{4.30}$$

Where $\underline{e}_k$ is an approximation error and $\underline{S}_k$ is its covariance matrix. The matrix R_k is the observation noise error covariance , and lastly R_l is the covariance of a statistical linearization error term.

4.2   Robust Estimators

4.2.1   Huber M-Estimator

Robust linear regression analysis provides an alternative method to the least squares regression analysis when fundamental assumptions required for the least squares approach are unfulfilled by the nature of the data. Robust methods have been designed to deal with the outliers. Outliers are data point that do not follow the model of the majority of the data. Despite being a well-established field, given the early seminal contributions of Huber [64] and Tukey [91], robust statistics and algorithms have received

renewed interest given the recent developments in computation power available in EMS. Consider the standard regression model in (4.31)

$$y = \chi\beta + \varepsilon \tag{4.31}$$

Where y and ε are vectors of dimension n and χ is a matrix of dimension n by p, and vector β has a dimension p. The Huber robust estimator $\hat{\beta}$ minimizes (4.32)

$$\sum_{i=1}^{n} \rho\left(\frac{y_i - \chi_i\beta}{S}\right) \tag{4.32}$$

Where S is an estimate of the standard deviation of the error term. Such that $S = \frac{MAD}{0.6745}$, where MAD is the median absolute deviation of the residuals from their median [92]. The constant 0.6745 makes the estimate consistent for a normal distribution. ρ is a loss function called rho-function or ρ-function which gives the contribution of each residual to the objective function[16], [25] and χ_I is the ith row of regressor matrix χ. If we let the ψ-function be ψ = ρ′ then a necessary condition for a minimum is that $\hat{\beta}$ satisfy:

$$\sum_{i=1}^{n} \chi_{ij}\psi\left(\frac{y_i - \chi_i\hat{\beta}}{S}\right) = 0 \text{ for all } j = 1, \dots, p \tag{4.33}$$

Table 1: ρ-functions and their weight functions for different types of M-estimators

Method	Objective Function	Weight Function
Least Squares	$\rho_{LS}(e) = e^2$	$w_{ls}(e) = 1$
Huber	$\rho_H(e) = \begin{cases} \frac{1}{2}e^2 & \text{for } |e| \leq k \\ k|e| - \frac{1}{2}k^2 & \text{for } |e| > k \end{cases}$	$w_H(e) = \begin{cases} 1 & \text{for } |e| \leq k \\ k/|e| & \text{for } |e| > k \end{cases}$
Tukey Bisquare	$\rho_B(e) = \begin{cases} \frac{k^2}{6}\left(1 - \left[1 - \left(\frac{e}{k}\right)^2\right]\right)^3 & \text{if } |e| \leq k \\ \frac{1}{6}k^2 & \text{if } |e| > k \end{cases}$	$w_H(e) = \begin{cases} \left[1 - \left(\frac{e}{k}\right)^2\right] & \text{for } |e| \leq k \\ 0 & \text{for } |e| > k \end{cases}$

The Huber rho-function and weight function are found in Table 1. The weight function is $w_H(e) = \psi(e)/e$. Applying the Huber M-estimator to estimate x_k at each correction step in equation (4.28) offers robustness against outliers in the measurement vector containing both elements $(z_k + H_k\hat{x}_k^- + \hat{z}_k^-)$ and $\hat{x}_k^-$. This was proposed in the literature for different applications, and specifically for power dynamic state estimation [93]. The rho-function needs to satisfy the following [94]:

1. $\rho(e)$ should be symmetric.

2. Always nonnegative $\rho(e) \geq 0$

3. Monotone in $|e_i|$, $\rho(e_i) \geq \rho(e_{i'})$ for $|e_i| > |e_{i'}|$

4. Equal to zero when its argument is zero $\rho(0) = 0$

5. $\rho(e)$ is continuous

6. let $a = \sup \rho(e)$, $then\ 0 < a < \infty$

7. if $\rho(e) < a$ and $0 \leq e < v$, then $\rho(e) < \rho(v)$

4.2.2 Robust S-Based Estimator

Proposed by Rousseeuw and Yohai [95] in the context of regression estimation, the S-estimator minimizes a robust M-estimate of the scale of the residuals. The S-estimator finds the smallest dispersion of the residuals calculated using the M-scale estimate. According to the authors [95], the S-estimator is defined by (4.34) with the M- scale estimator $\hat{\sigma}_s$ satisfying (4.35). Through this minimization of a robust scale, the S-estimator down-weights points that deviate from the regression line or hyperplane. The S-estimator can reach high breakdown points. The breakdown point is the maximum percentage of outliers an estimator can resist while being still reliable. Outliers could be on the observation or measurement vector (called y-axis outliers) or in the regressor points or one ith point, χ_i, which is the ith row of regressor matrix χ (called x-axis outliers or leverage points). Bad leverage points are outliers on the regressors, or points that are far from the bulk data on the x-axis and do not obey the regression model. Since the S-estimator evaluates the regression model and the scale, it keeps good leverage points that obey the model and down weights the effect of bad leverage points or x-axis outliers.

$$\hat{\beta}_s = \min_{\beta} \hat{\sigma}_s(e_1, e_2, \dots, e_n) \tag{4.34}$$

$$\frac{1}{n}\sum_{i=1}^n \rho\left(\frac{y_i - \sum_{i=1}^n \chi_i\beta}{\hat{\sigma}_s}\right) = b \tag{4.35}$$

The parameter b is chosen to be $b = E_\Phi[\rho(e)]$, Φ represents the standard normal distribution, ρ is the weighting rho-function and is bounded [64], and E_Φ is the expected value. Notice that the WLS would be equivalent to using the classical standard deviation as $\hat{\sigma}_s$ where $\rho(r) = r^2$. Different ρ-functions could be chosen to ensure robustness, such as the Huber ρ-function. For this application the bi-square ρ-function is chosen, as shown in Table 1.

In the case of a regressor matrix, χ, satisfying the general position condition (i.e., any n rows of χ are linearly independent), constants used within the S-estimator can be found in [95], allowing a theoretical

breakdown point of up 0.5. The finite-sample breakdown measures global robustness and is defined as the maximum fraction of the worst outliers an estimator can resist while still giving reliable estimates, i.e., the estimation bias is still finite [25].

The theoretical breakdown point for S-estimators was derived in Mili and Coakley [96] for structured linear regression where the rows of χ are sparse and dependent. The authors showed that if the S-estimator satisfies $b/\rho(k) = (n - q + 1)/n$ shown in (4.35). Then the finite breakdown point is $\varepsilon_m(\hat{x}, Z) = (n - q + 1)/n$.

$$\left\lceil \frac{n+N+2}{2} \right\rceil \leq q \leq n \tag{4.36}$$

Where $\lceil \cdot \rceil$ is the greatest integer function and n is the number of measurements. The maximum number of row vectors that lie on a hyperplane of dimension (p-1) is denoted N [55]. As indicated in the literature, while the S-estimator is highly resistant to bad data reaching a high breakdown point, it comes at the cost of possibly a low efficiency. This implies the reduced accuracy of the estimates if the data is clean and Gaussian.

4.2.3   Robust MM-Based Estimator

In 1987, Yohai [97] introduced a new improvement toward higher efficiency for high-breakdown estimators like LMS and LTS. He called this new estimator the Modified M estimator (MM). The MM estimation procedure begins with estimating the regression parameters using S-based estimation techniques. This MM estimator simultaneously has a high breakdown point, and high efficiency with Gaussian distributed errors. MM-estimation is built upon a multi-step process where an efficient M-estimator is used following a high-breakdown point estimator that gives the initial starting β estimate. In this case, the M- was used in conjunction with the S-estimator to take advantage of the high breakdown point of the latter estimator [66], [98], [99]. MM-estimation can be defined by (4.37) [99], [100].

$$\sum_{i=1}^{n} \psi \left(\frac{y_i - \sum_{i=1}^{n} \chi_i \beta}{\hat{\sigma}_s} \right) \chi_{ij} = 0 \text{ for } j = 1, \dots, p \tag{4.37}$$

Possible functions ρ and ψ for both estimators can be found in [95]. An algorithm to execute the MM- is available in [97], [100] with a possible choice of both the breakdown point and the efficiency. With the steps above, the best statistical properties of the two estimation procedures are brought together, although with the disadvantage that the computational effort is increased. The algorithm could be parallelized to reduce the computation burden. The scale estimate $\hat{\sigma}_s$ is obtained from the residuals of the S-estimation method for a chosen ρ and b that ensures an initial high breakdown point.

The classical procedure for the MM-estimator is as follows [99]:

1. Apply a high breakdown point S-estimator to get the initial β, calculate the residuals and their corresponding high breakdown point M-robust scale estimate $\hat{\sigma}_s$

2. The re-weighted least squares is executed iteratively with Tukey's weights (w_i) as given in Table 1 to get the final coefficients after convergence

$$\sum_{i=1}^{n} w_i \left(\frac{y_i - \sum_{i=1}^{n} \chi_i \beta}{\hat{\sigma}_s} \right) \chi_{ij} = 0 \text{ for } j = 1, \dots, p \tag{4.38}$$

4.3   Sub Sampling Techniques

In the classical S algorithm, a set of non-singular subsamples is used to determine the best regressor values "betas" within our regression equation (4.39).

$$y_i = \beta_0^t x_i + \varepsilon_i \tag{4.39}$$

This nonsingular random sample of the data points containing measurements is taken and their corresponding rows in the regressor matrix of size equal to the number of states. The least-squares problem may now be solved on this reduced data set and a refinement of the resulting parameter and simultaneous scale on the whole dataset may be made. This is repeated a pre-specified number of times. The final S-estimate gives the smallest robust M-estimate of residuals scale and the associated regression coefficient beta. Since the regressor matrix is very sparse, a singular subsample could be randomly chosen. If a singular subsample is chosen or the subsample is not full rank, the algorithm fails at solving the least-squares problem. The selection starts again by taking a new subsample. The probability of discarding increases steeply with large matrixes. In this case, the discard rate is excessive and requires an enormous number of primary subsamples before the desired number of nonsingular ones is reached. In this situation, simple random subsampling algorithms are infeasible. In the case of high dimensional power system datasets, as described by the number of states of a system, the computation time and the total number of combinations increase to an infeasible time. This can be described by probability where a set of all k row combinations of a set of n rows or the ("n choose k") as shown in equation (4.40) where k is greater than n.

$$\binom{n}{k} = \frac{n!}{(n-k)! \, k!} \tag{4.40}$$

This subsampling technique works well for small to medium datasets, which are largely overdetermined. In methods such as QR, LU, and Single Value Decomposition (SVD), computation techniques are used to compute the rank of a matrix for analysis [101]–[103]. However, the application of LU provides a few advantages since it is quicker, on the order of $\frac{2}{3}m^3$ than QR which is on the order

of $\frac{3}{2}m^3$, and SVD which is on the order of $12m^3$ [103] where m is the size of the square matrix. The Cholesky decomposition is twice as fast as the LU decomposition but only for positive definite Hermitian matrices [103]. Thus LU with Gaussian elimination was used. In this application, a random subset should be selected for the S- estimation to enhance the probability of convergence and the removal of leverage points. LU decomposition allows for more modularity through row pivoting by Gaussian elimination, either partial or complete. Through Gaussian elimination, a non-singular full rank matrix can be deterministically found instead of a random combination in the standard S-estimation theory. That is to say, instead of randomly selecting a subset and testing for non-singularity, observations may be drawn sequentially and the ones which cause a singularity may be discarded.

The overdetermined matrix is key in this solution. In this, LU decomposition with pivoting may be implemented to determine a subset of the overdetermined matrix which is full rank by building a matrix that is a full rank through partial pivoting. Thus, instead of fully random sampling, a random subsample may be built systematically. In the realm of statistics, M. Koller implemented a similar technique [104] with regards to nonsingular subsampling for S-estimators with categorical predictors in R. The specific subsampling algorithm produced in MATLAB for this research may be provided upon request.

Chapter 5 High Breakdown point Robust Distribution Static State Estimation

This chapter develops robust estimators for the distribution static state estimation. The purpose is to explore the impacts of bad data on energy markets and related Distribution Locational Marginal Prices (DLMPs) and how robust estimators can assist in the removal of bad data and improve state estimation robustness. This is where robust estimation theory becomes increasingly relevant and valuable to power systems state estimation. Robust estimation offers increased grid operation and control resilience when data is not trustworthy or departs from model assumptions. In a past project conducted from 2018 to 2021, the Transactive Power Application (TPA) prototype was created with collaborators which allows the users to buy and sell power and energy on the distribution system with utility oversight [105]. Consumers that can generate power from solar PV are called prosumers. Additional analytics are conducted behind the application in OpenDSS for each transaction to ensure the feasibility of the power flow solutions in the system.

Many existing static state-estimation methods are based on the Gaussian assumption, such as the WLS. This chapter shows the effects on the distribution state estimation process and resulting DLMPs by corrupted data. Various scenarios are analyzed by applying standard estimators with typical power system operation in steady-state operation. Cyberattacks are introduced into the system to simulate the effects on estimation and DLMP prices such that:

1. Modifying the PMU data received by the estimators to observe the effects of corrupted data
2. Modifying the topology of the system used in the state estimation of the physical reality by augmenting the values in Y_{bus} to create instabilities in the system.

5.1 Distribution Modeling With OpenDSS for Static State Estimation

The multi-phase distribution system model uses the equations given in chapter 3. OpenDSS, an open-source software that utilizes Carsons' equations is used to generate power flows and admittance matrix. OpenDSS [106], a free opensource software developed by Electric Power Research Institute (EPRI), provides a code-based user interface that allows for co-simulation with MATLAB and PYTHON. Co-simulation with OpenDSS and MATLAB has been conducted to generate the Y_{bus} and initial power flow values which are used as input measurements to the static distribution state estimation. The output of the distribution SSE was used to calculate distribution system prices. Scripts were created to read the text output files from OpenDSS:

1. Y_{bus}
2. Y-Primitive
3. Capacitance-Primitive
4. Voltage Phasor at each bus
5. Power injection at each bus
6. Power flow on each line (multi-phase)
7. Line configuration and naming convention
8. Bus location and naming convention

The standard notation applies in exporting the Y_{bus} in OpenDSS, as seen in (5.1).

$$I = Y_{bus}V \qquad (5.1)$$

The vector of nodal current injection I are calculated using the Y_{bus} and the voltages in V. In this application, the Y_{bus} exported by OpenDSS [78] does not include series and shunt admittances, however they may be found by exporting the Y-Primitive and capacitance-Primitive matrices. To fully calculate the desired line representation, the line capacitance values need to be added to the Y_{bus}, or the Y-Primitive matrix needs to be utilized. In this case, the capacitance matrix exported from OpenDSS was utilized and added to the Y_{bus}. To convert the capacitance matrix to the respective admittance values, equation (5.2) is used. Where the Cmatrix is the capacitance primitive matrix from OpenDSS. *L* is the unit length defined by the user in OpenDSS, and Ybase is the admittance base of the system.

$$C_{admittance} = \frac{\left(\frac{2\pi f}{2}C_{matrix}(1e-9)*L\right)}{Ybase} \qquad (5.2)$$

To create the model of the distribution system the equipment were entered into a database using a JSON format. In this, all fields required by OpenDSS were included in the JSON file such as names, locations, impedances, regulator tap positions and operating limits. The specific files were broken into fields such as:

1. Lines
2. Transformers
3. Voltage regulators
4. Consumption Load Sites
5. Production Sites

A SQL database was created and managed by team members, and through this database, a communication port was opened with OpenDSS to generate the distribution system topology (Y_{bus})

and simulate the power flow. This Y_{bus} and power flow are noted as the system's operating point in a discrete-time and is recomputed at every market close at hourly intervals. As the distribution system changes throughout the day due to respective loads, or topologies, the data loaded and exported by OpenDSS changes. This data is read into MATLAB and the database for use in calculation of additional analytics such as pricing, and approval or denial of power contracts. The distribution system model flow diagram which was used to generate the measurement model can be seen in Figure 2.
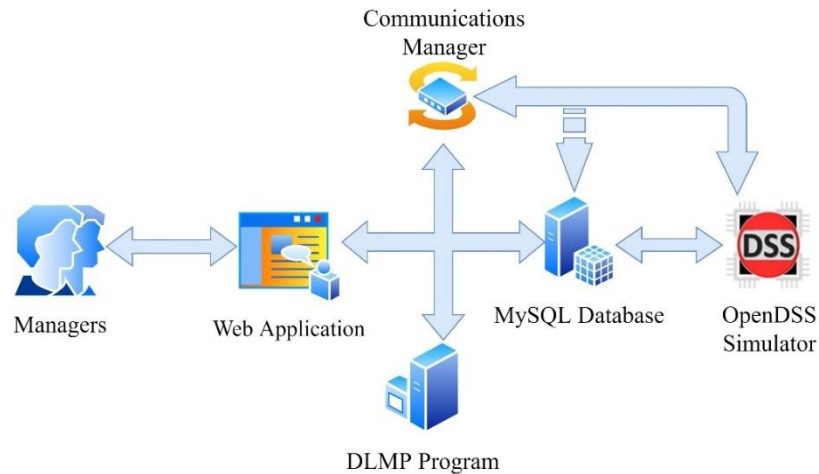
Figure 2: Transactive Power Application Flow Diagram

5.2   Distribution Locational Marginal Pricing

With the addition of distributed generation into the distribution system, the distribution system operator (DSO) has the ability to incorporate a new market. In this market, the social welfare of its prosumers can be evaluated and prices can be calculated with respect to location. In literature and everyday operation, this locational marginal pricing (LMP) [107] has been the backbone of transmission companies' market structure and dispatch. This application can also be applied to the distribution system such as a distribution locational marginal price (DLMP). As proposed in [107]–[109], DLMP values provide a standpoint of the distribution grid conditions to the wholesale energy market or cleared price for the energy market. Through metering, this social welfare can be applied to a supply and bid function similar to the LMP and provides the following optimization welfare function (21), where p^{FL}, p^{DG}, q^{DG} are the procurement of real and reactive power from distributed generation (DG) and flexible loads (FL).

With the increased renewable distributed generation integrated into the distribution system, the trend towards a more open competitive market will impact the grid operation and the needed control by the distribution system operators (DSO). The general economic and social welfare can be maximized by

considering DLMP representing the price of incremental power injected or consumed at different locations. In practice, the LMPs are considered for power transmission markets [107], [110], [111].

The objective is to minimize the total cost while ensuring the system constraints and boundaries are satisfied. Equality constraints translate the need for real and reactive power consumption and supply balances within the distribution system. The inequality constraints represent the limits of the distributed generation, lines' and transformers' capacity limits, voltage constraints at different nodes. These constraints are included in the cost function using Lagrangian multipliers. The cost function is then minimized using semi-definite programming that provides the total optimized cost and the DLMPs at different nodes. The obtained DLMPs can be classified into real power DLMPs and reactive power DLMPs. Each DLMP contains four price components that are added together to provide the nodal price [112]. The four elements of a DLMP are increment costs corresponding to injected energy, loss, congestion, and voltage levels. Indeed, the final nodal price (DLMP) represents the impact of loads and generation (injections) at that node on the distribution grid, considering the value of losses, energy cost, and congestion components.

These DLMP values provide a standpoint of the distribution grid conditions to the wholesale energy market or cleared price for the energy market. The impact of the LMP from the transmission system was included as well at the distribution feeder. DLMP prices were evaluated and calculated down the feeder, and the obtained fluctuations of the DLMP price relates to the grid

$$\text{maximize } w\big(p^{FL}, p^{DG}, q^{DG}\big) := w_p\big(p^{FL}, p^{DG}\big) + w_p\big(q^{DG}\big) \tag{5.3}$$

To maximize this optimization problem, constraints and boundaries are set to calculate the DLMP price. The real and reactive power losses are represented by p^l and q^l respectively. equation (5.4) denotes the voltage threshold. Each of the real and reactive powers limits for the distributed generation is set within the optimization problem as noted in (5.4)-(5.7).

$$V_L^- \leq V_L \leq V_L^+ \tag{5.4}$$

$$p^{DG-} \leq p^{DG} \leq p^{DG+} \tag{5.5}$$

$$q^{DG-} \leq q^{DG} \leq q^{DG+} \tag{5.6}$$

$$p^{FL-} \leq p^{FL} \leq p^{FL+} \tag{5.7}$$

Once the constraints have been set, the DLMP values can be determined and optimized through semi-definite programming [109]. The overall representation of the DLMP values can be found in the real

power equation (5.8) and reactive power DLMP (5.9). These equations are composed of the energy $\frac{\Pi_p^E}{\Pi_q^E}$, loss $\frac{\Pi_p^L}{\Pi_q^L}$, congestion $\frac{\Pi_p^C}{\Pi_q^C}$, and voltage $\frac{\Pi_p^V}{\Pi_q^V}$ terms.

$$\Pi_p^{Grid} = \Pi_p^E + \Pi_p^L + \Pi_p^C + \Pi_p^V \tag{5.8}$$

$$\Pi_q^{Grid} = \Pi_q^E + \Pi_q^L + \Pi_q^C + \Pi_q^V \tag{5.9}$$

This formulation in (5.8) and (5.9) provides prices that may be used as a contribution to a nodal price noted as the DLMP. A nodal price represents the impact of loads and generation on the distribution grid by decomposing the value into losses, energy, and congestion components. More details about the equations and algorithm are available in [112].

5.2.1   *Prosumer Based Distribution Market*

The model of a modified IEEE 13-bus system is introduced in this section. This system is used for the robust distribution static state estimation evaluation. The IEEE 13-bus system is based on a 4.16kV voltage level with relatively short line distances [112]. The base system is a small distribution network but has a significant load which provides flexibility in generating scenarios for analytics. The lines are modeled as overhead and underground lines, with the availability of a shunt capacitor and regulating transformer. To verify the impact of the transactions on the voltage stability of the grid, a three-phase power flow analysis was conducted for calculating the voltage phasors. The power flow calculations were performed using OpenDSS [78]. OpenDSS was selected for its ability to analyze unbalanced systems and for the simplicity of connecting it to the web application. The prosumer enhanced 13-bus system specified was the power system model used for this analysis. This multi-phase system incorporates a radial distribution system with aggregated loads designating residential, commercial, and industrial loads as shown in Figure 3. This system is ideal to examine the impact of bad data on state estimators, pricing, and redundancy of measurements.
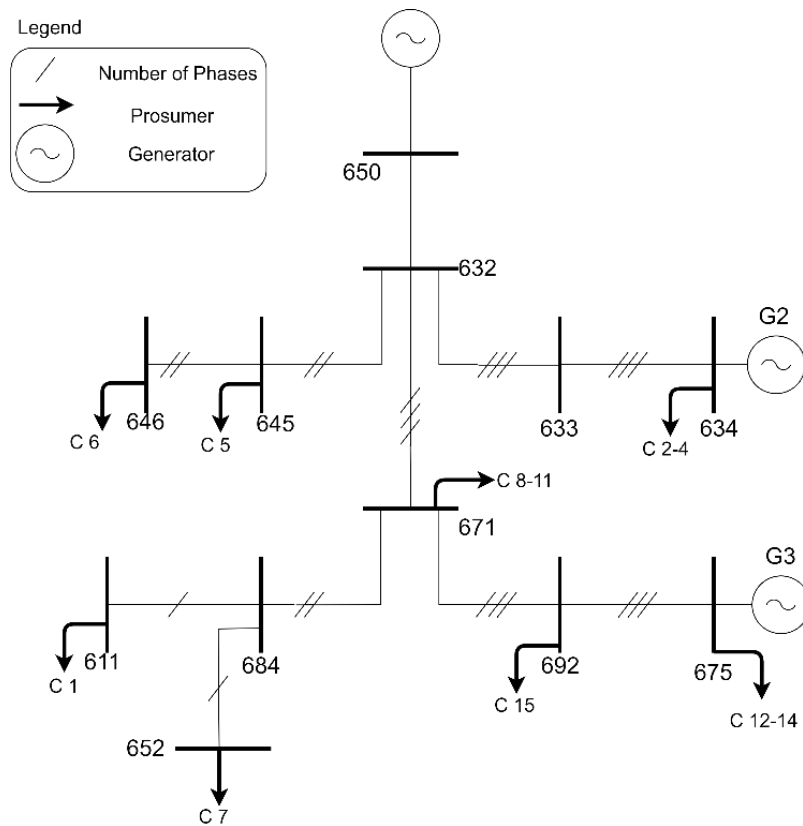
Figure 3: Modified IEEE 13-bus model with dispatchable generation

Table 2: Modified IEEE 13-bus model prosumer information and location

Load #	P (kW)	Q (kVAR)	Bus	Phases
1	170	80	611	1
2	160	110	634a	1
3	120	90	634b	1
4	120	90	634c	1
5	170	125	645	1
6	230	132	646	2
7	128	86	652	1
8	17	10	670a	1
9	66	38	670b	1
10	117	68	670c	1
11	1155	660	671	3
12	485	190	675a	1
13	68	60	675b	1
14	290	212	675c	1

Table 3: Modified IEEE 13-bus model prosumer information for simulation 1

Customer	kW	kVAR
C1	170	20
C2	160	115
C3	120	109
C4	120	240
C5	170	125
C6	0	0
C7	128	68
C8	8.5	5
C9	33	19
C10	58.5	34
C11	0	0
C12	485	-10
C13	68	-140
C14	290	12

At each customer location, there is a meter recording voltage, current, angle, and power. When a case is executed, OpenDSS calculates the power flow and exports the metered data for data analytics to simulate measurements received from SCADA or PMUs. With metered data collected at each prosumer site, the application monitors the voltages at the customer meter point for transaction feasibility determination. If the voltage level at a consumer location exceeds a per unit (p.u.) threshold (for example 1.05) with the transaction time, then that transaction will be *disabled*. Such that, the allocated transaction will be removed from the database, and therefore will not be reflected in the power flow calculations.

5.2.1.1 <u>Distribution Locational Marginal Pricing Simulation</u>

For a case example for the inclusion of prosumer-based photovoltaic generation into the IEEE 13-bus system. The PV rooftop generation is assumed to be installed in residential areas to produce real power. The total power penetration of PV was set to 60% of the stated residential loads. The industrial load at bus 675 (C11-13) consumes all of its power. A total of 512 kW PV generation was added to the system. Thus, the total load supplied by the classical dispatchable generation reduces from 1811kW to 1290kW. With this amount of generated PV power, Table 4 shows that generator 650 on phase A is no longer producing any real power. This means that, in phase A, real power is not purchased from the substation feeder. It is noted that the PV and dispatchable generation fully cover the consumed power within phase A.

Table 4: Dispatchable Generation with 60% PV generation.

Generator Location	kW	kVAR
650.A	0	46.758
650.B	78.487	182.46
650.C	225.17	160.78
634.A	28.441	0
634.B	50	0
634.C	50	0
675.A	250	0
675.B	250	0
675.C	250	0

Table 5:Customer Load with 60% PV generation.

Customer	kW	kVAR
C1	68	20
C2	64	115
C3	48	109
C4	48	240
C5	68	125
C6	0	0
C7	51.2	86
C8	8.5	5
C9	33	19
C10	58.5	34
C11	0	0
C12	485	-10
C13	68	-140
C14	290	12

Figure 4 displays the DLMPs in phase A, which are around the same cost as the dispatchable generation. Figure 5 indicates the reactive DLMPs where the generators and the PVs are assumed to provide only real power. The DLMPs values are close to the cost of reactive power at the feeder 11 c/kVARh. It can be noted that the dispatchable generators at bus 634 and bus 675 do not produce reactive power, therefore, the primary optimization of reactive power in the case was around the substation amount and price of reactive power. The real power price in cents per kilowatt hours is denoted by c/kwh is. The reactive power price in cents per kilovars hours is denoted by c/kVARh.
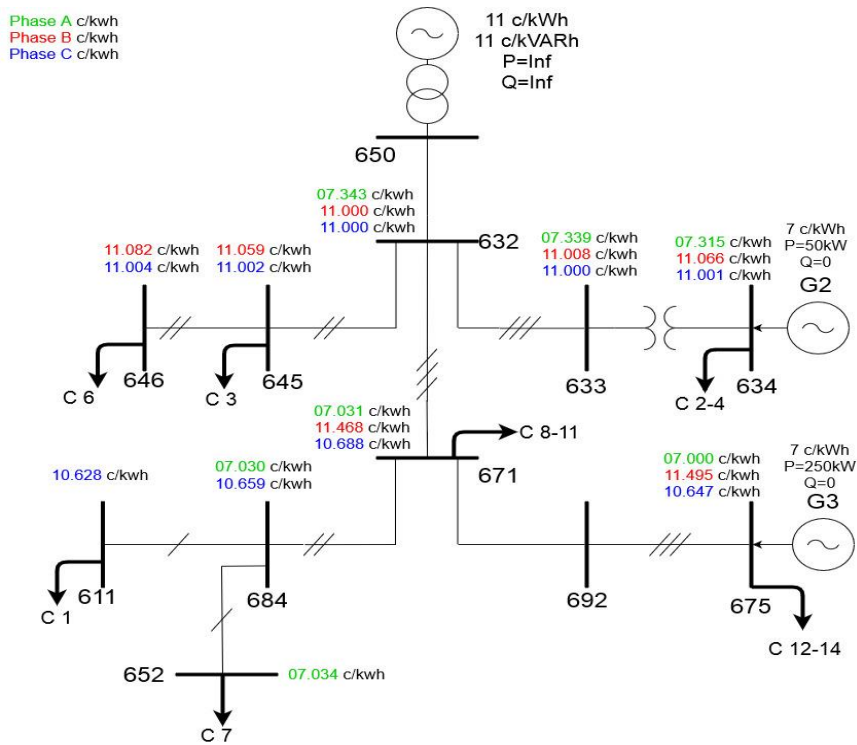
Figure 4: Real power DLMP at different buses of the IEEE 13 bus system with 60% PV
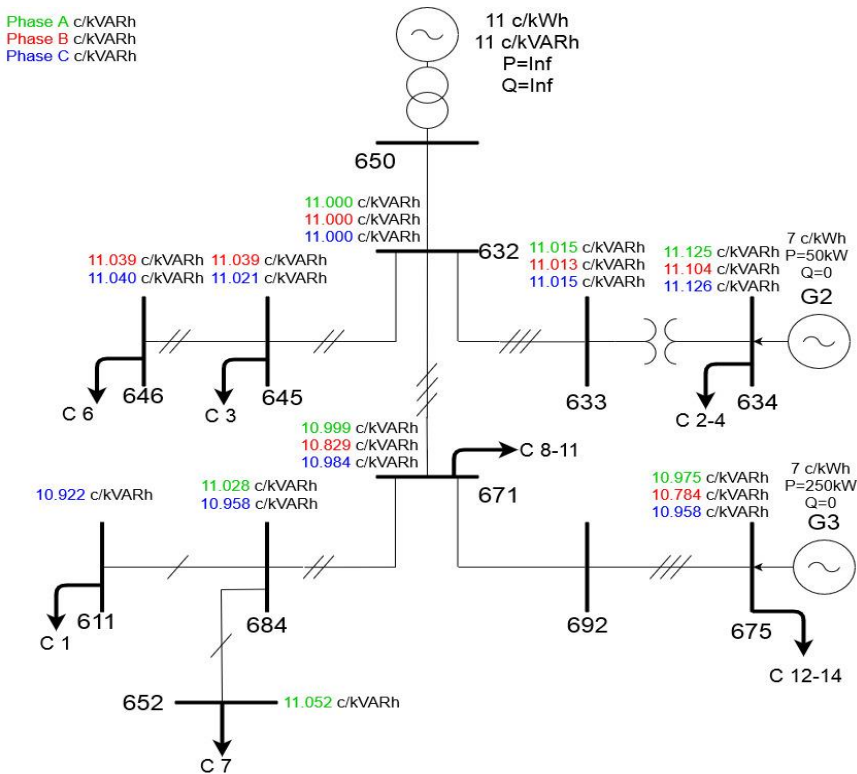
Figure 5: Reactive power DLMP at different buses of the IEEE 13 bus system with 60% PV.

This simulation above provides insight into how the Transactive Power Application operates with regard to power flow, pricing, and congestion. These prices are used and displayed on the Transactive Power Application for utility oversight.

Figure 6: Prosumer Power (kWh) and purchase cost ($) from April 5th to April 15th 2021
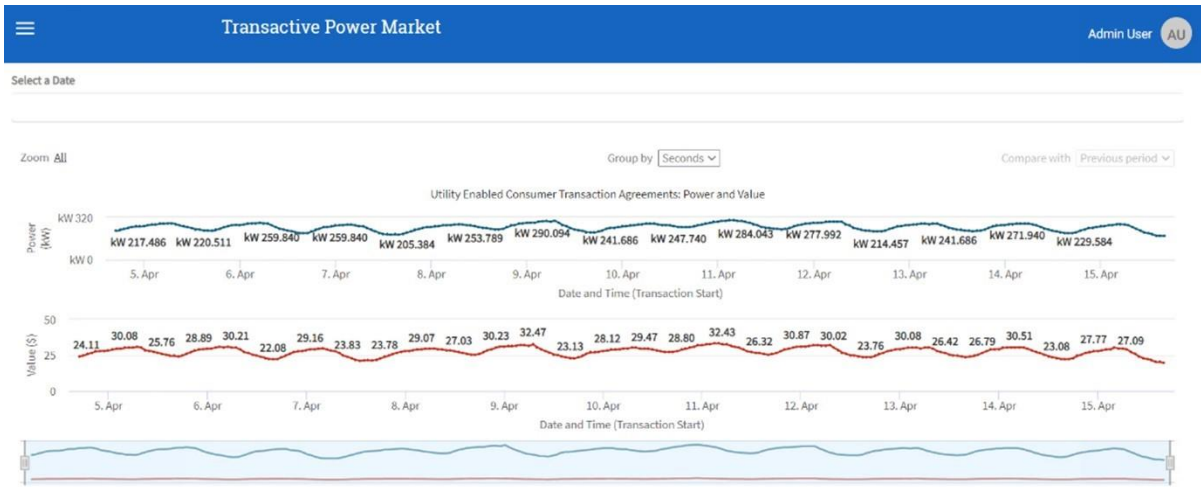
Figure 7: Smart Building usage (kWh) and purchase cost ($) from April 5th to April 15th 2021

Figure 8: Bus 634 DLMP Prices from April 5th to April 15th 2021

A time series of weather data was collected between April 5th to April 15th 2021 in the north Idaho region. Figure 6 shows the power usage of consumer where the oscillatory characteristics correspond to day and night cycles. Figure 7 provides the consistent loading of a smart building purchasing power. Lastly Figure, 8 provides a visual example of the system where the voltages became too close to their limits on the distribution system, and the relating cost was impacted due to the violation. It can be seen that the prices have increased in phases A and C, and supplementally, the price has dropped on phase B due to the voltage violation.

5.2.2   Distribution System State Estimation Model

The IEEE-13 bus model was simulated in OpenDSS as described in the previous section, and dataflow gives the true measurements to which random noise is added. At a given time snapshot, the system state vector $x \in R^n$ relates to the vector of measurements $z \in R^m$ by :

$$z = h(x) + e \tag{5.10}$$

$$\overline{V} = \begin{bmatrix} |V|_{1a} \\ |V|_{1b} \\ \vdots \\ |V|_m \end{bmatrix} \overline{\theta} = \begin{bmatrix} \theta_{1a} \\ \theta_{1b} \\ \vdots \\ \theta_m \end{bmatrix} \overline{P}_{inj} = \begin{bmatrix} P_{inj_1} \\ P_{inj_2} \\ \vdots \\ P_{inj_m} \end{bmatrix} \overline{Q}_{inj} = \begin{bmatrix} Q_{inj_1} \\ Q_{inj_2} \\ \vdots \\ Q_{inj_m} \end{bmatrix} \overline{P}_{flow} = \begin{bmatrix} P_{flow_1} \\ P_{flow_2} \\ \vdots \\ P_{flow_m} \end{bmatrix} \overline{Q}_{flow} = \begin{bmatrix} Q_{flow_1} \\ Q_{flow_2} \\ \vdots \\ Q_{flow_m} \end{bmatrix} \tag{5.11}$$

In (5.11) above, the measurements are dictated by their respective node. More explicitly, the measurement vector for the voltages $\overline{V}$ is the voltages for each individual node where $|V|_{1a}$ is the voltage magnitude of bus 1 phase a. Secondly, the power injection $\overline{P}_{inj}$ and $\overline{Q}_{inj}$ is per node. Lastly, $\overline{P}_{flow}$ and $\overline{Q}_{flow}$ are the real and reactive power flows on each phase.

$$z = \begin{bmatrix} \overline{V} \\ \overline{\theta} \\ \overline{P_{InJ}} \\ \overline{Q_{InJ}} \\ \overline{P_{flow}} \\ \overline{Q_{flow}} \end{bmatrix}, h(x) = \begin{bmatrix} h_1(x_1, x_2 \ldots x_n) \\ h_2(x_1, x_2 \ldots x_n) \\ \vdots \\ h_m(x_1, x_2 \ldots x_n) \end{bmatrix}, e = \begin{bmatrix} e_1 \\ e_2 \\ \vdots \\ e_m \end{bmatrix} \quad (5.12)$$

The function $h(x)$ is nonlinear, known as the measurement function, and e is a vector representing measurement errors generally assumed to be Gaussian. The measurements could contain $\overline{\theta}$ if we micro-PMUs are available. The state estimation is obtained by minimizing the objective function J in (5.13)

$$J(x) = \sum_{i=1}^{m} \frac{(z_i - h_i(x))^2}{R_{ii}} \quad (5.13)$$

The function J represents the summation of the squares of the measurement residuals weighted by their respective measurement error variance R_{ii}. This objective function can be rewritten as :

$$J(x) = (z - h(x))^T R^{-1}(z - h(x)) \quad (5.14)$$

Where R is the covariance matrix of the measurement errors and is assumed to be a diagonal matrix and $(.)^T$ is the transpose of a vector. The matrix [H] is the Jacobian of the measurement vector with respect to the state vector for all three phases. The measurement function and Jacobian can be constructed using the known system model, including branch parameters, network topology, and measurement locations and types. The network topology is derived by a sparse system admittance matrix known as the Y-bus matrix. Most of the elements are found on the diagonal, and the cross-correlation terms are located between the relating indices. The admittance found in the Y-bus matrix is used to compute both the H matrix and measurement h(.) vector. The state estimation is solved with an iterative algorithm (5.15) to (5.18).

$$[H] = \frac{\partial h(x)^T}{\partial x} \quad (5.15)$$

$$G(x^k) = [H]^T [R^{-1}][H] \quad (5.16)$$

$$\Delta x^{k+1} = G(x^k)^{-1} [H]^T [R^{-1}][z - h(x^k)] \quad (5.17)$$

Equation (5.16) is the system gain matrix and (5.17) shows the update to the state for the weighted least squares algorithm. It can be seen that to obtain Δx^{k+1} that the inverse of the gain matrix needs to be taken. To avoid the inverse, the Gain matrix G(x) can be decomposed into its triangular factors by

Cholesky factorization resulting in (10-13) and solved using forward and backward substitution at each iteration [113].

$$[G(x^k)] = [L] \cdot [L]^T \tag{5.18}$$

$$L \cdot L^T \cdot \Delta x^{k+1} = -g(x^k) \tag{5.19}$$

$$L^T \cdot \Delta x^{k+1} = {-g_i(x^k)} / {L_{11}} \tag{5.20}$$

$$x^{k+1} = x^k + \Delta x^{k+1} \tag{5.21}$$

After the convergence of the algorithm, i.e., $\|\Delta x^{k+1}\|$ is small enough, a bad data detector (BDD) is applied to flag the bad data by analyzing of the normalized residuals. Commonly the application of the chi-squared test is used to detect if outliers are present in the data set, however the LNR method is chosen in this research. The LNR, which is the maximum of the normalized absolute residuals, is checked, and the measurement is rejected if larger than a chosen threshold such as 3. This is noted in (5.22)-(5.23).

$$|\text{residuals}| = |z - h(x)| \tag{5.22}$$

$$\text{LNR} = \frac{|\text{residuals}|}{\sqrt{\text{diag(R)}}} > 3 \tag{5.23}$$

The robust estimators are applied to the modified IEEE 13-bus system shown in Figure 9. Here, bad data is introduced as measurement attacks and topology attacks on the three-phase system. In these simulation cases, four different estimators are implemented. All estimators used the same power flow and Jacobian equations. The measurement vector has been reduced to a minimal set of PMU devices. This reduction of measurements permits testing the estimators' performance in a scenario with low redundancy of measurements. The system will be more susceptible to cyber-attacks and shows the advantage of robust static estimation.

5.3   Distribution State Estimation Simulations

The IEEE 13-bus model is implemented and used as the test case to test the impact of bad data on the distribution system, including the original un-modified single, two, and three-phase loads. In modifying the IEEE 13-Bus model, the regulator has been removed to avoid a recursive scenario with the DLMP calculation and voltage regulation tap changes in OpenDSS. In defining the measurements in the system, PMUs are placed among the distribution system to minimize the number of μPMUs [114]. Each μPMU is capable of measuring voltage magnitude, phase angle, and both active and reactive power injections. Each line has measurements for two active and two reactive power flows at its ends. As

indicated in Table 6 on the next page, only one set of power flow measurements is used in the measurement calculations. Reducing the number of PMUs permits testing each estimator's ability for a lower redundant system. The goal is also to create a system with the possibility of leverage points to impact the effectiveness of each filter. Also indicated in Figure 9, distributed generators have been incorporated into the test system to allow for the respective energy market implementation, and their values are presented in Table 7. In the simulations, two cases are evaluated. In the first case, bad data corrupts the measurements of the system. In the second case, bad data is introduced into the perceived topology of the system implemented by the state estimator, impacting both the estimation and resulting price signals.
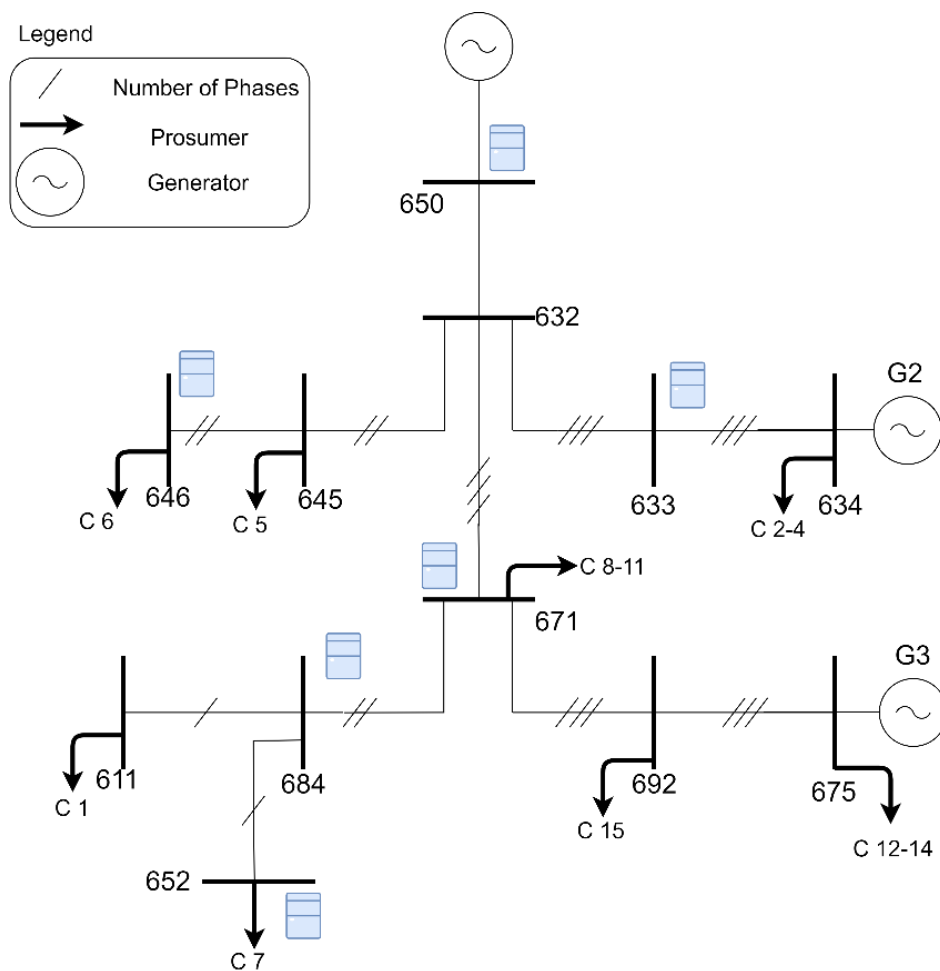
Figure 9: Modified IEEE 13-Bus model with PMU placements

Table 6: Measurement Redundancy for the Modified IEEE 13-bus model

Type of measurements	Amount/Total
V_i	13/26
θ_i	13/26
P_i	16/16
P_{ij}	15/23
P_{ji}	0/23
Q_i	16/16
Q_{ij}	15/23
Q_{ji}	0/23
Total Number	77/176
Total Amount of States	51
Redundancy Ratio	77/51
Number of Branches	26

Table 7: Dispatchable generation real and reactive power values

Generator Location	kW	kVAR
650.A	Inf	Inf
650.B	Inf	Inf
650.C	Inf	Inf
634.A	50	0
634.B	50	0
634.C	50	0
675.A	250	0
675.B	250	0
675.C	250	0

Four estimators will be evaluated with the modified IEEE 13-bus model. The system will be estimated to provide an observable estimate of each bus's voltage magnitude and angles with a limited number of micro-PMU measurements. These estimated states are used as input to the DLMP pricing algorithm. The first estimator is the WLS using a forward and backward sweep for solving with the largest normalized residual test for bad data removal. The second estimator is the Huber M-estimator implemented by the ROBUSTFIT robust linear regression function in MATLAB. The third is the proposed S- estimator upgraded by a bad data detection and a final WLS. Lastly, the proposed MM-estimator is followed by a bad data detection with a final WLS. The extra step of bad data detection with a WLS might not be needed for the MM- since it can ensure high efficiency. The extra step, however, improves the efficiency of the S-estimator. Algorithms of the S- and MM-estimators are provided in [64]. We have adapted those to the power systems context with a sparse regressor matrix and computed the increment state Δx^{k+1} in (5.20) by regressing the $[z - h(x^k)]$ on the Jacobian

[H] using these high breakdown robust estimators until convergence. Once a convergent state has been found, the bad data detection is applied to determine if there is bad data present.

5.3.1 *Distribution State Estimation of the IEEE 13-Bus System Under Measurement False Data Injection Attacks*

A man-in-the-middle attack could generate a false data injection where measurements are corrupted. The FDI could lead to degraded state estimation quality and maliciously impacted prices. An example would be a prosumer measured value of power that might not be feasible, such that the house has a capability of 8kW production with an erroneous measurement of 80kW. Without a security or resiliency assessment, a value of 80kW would be incorporated into the state estimation calculations, potentially causing the wrong state of the system and pricing. Attacks could even prevent the state estimator and pricing algorithm from converging.

In the first series of experiments, the robust estimators are evaluated by their ability to identify and reject the bad data with measurement FDI attacks. Each estimator will experience the same topology matrix and measurement vector. A uniformly random scaling factor 1-90% or 110-200% corrupted the original measurement vector to create the measurement FDI attack. The rand function [115] from Matlab was used to generate the vector of bad data and scaling factors individually. Such that $z_k = h(x_k)$ is corrupted by a random number $C_k(I)$ following a uniform distribution. In this, equation (5.24) denotes the application of the FDI injection, modifying the measurement vector, plus added normal noise.

$$z_k^c(i) = z_k(i) \cdot C_k(i) + v_k(i) \tag{5.24}$$

A Monte-Carlo experiment has been conducted to evaluate the impact of attacks. Up to four corrupted measurements were injected simultaneously per case with a set of 200 Monte-Carlo replications. The considered metrics are the detection rate of true cyberattacks and the root mean squared error (RMSE). Table 8 on the next page provides the location of the four pieces of bad data, and in each case, the multiplying factor ranged between 50% and 150%.

Table 8: False Data Injection For Sample Monte-Carlo Simulation

Item	Value
False Data Injection Location	41 Node Voltage– node 646.B
	51 Node Angle – node 645.B
	54 Node Angle – node 646.C
	60 Power Flow – node 633.C – 634.C
Bad Data Multiplier	115.14%
	112.72%
	141.29%
	110.61%
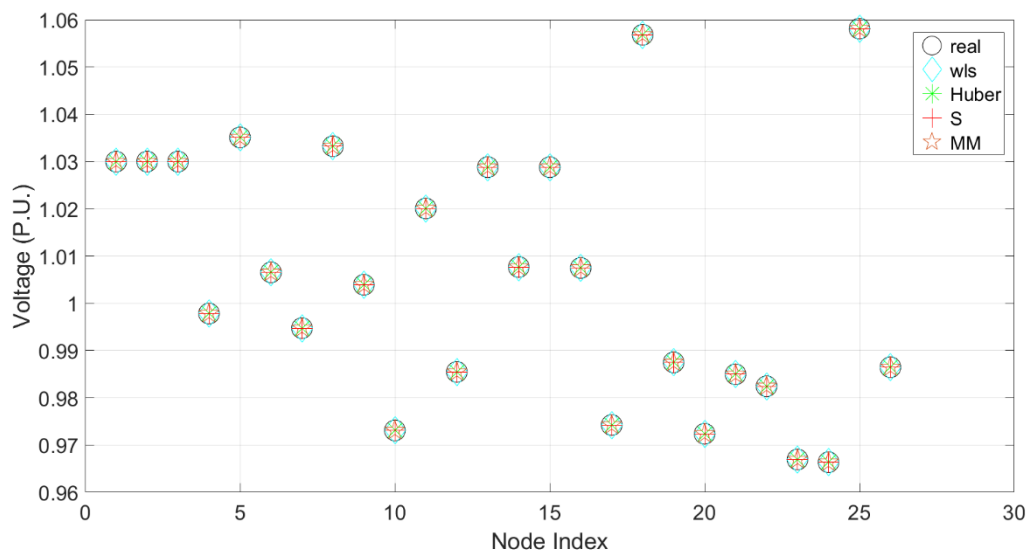
Figure 10: IEEE 13-Bus Estimation of node voltage magnitude for measurement FDI attack
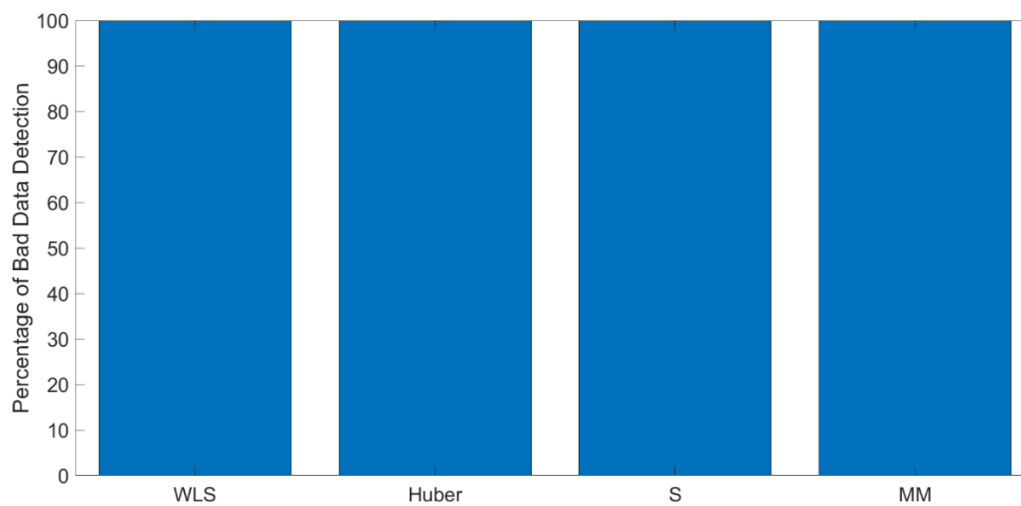
Figure 11: Percentage of bad data detection for a 200 case Monte-Carlo simulation

As a metric, the average RMSE was calculated to provide the relative error of the estimators. Equation (5.25) indicates the average RMSE calculation where i is the variable, N is the number of Monte-Carlo simulations, x_i is the actual state, and $\hat{x}_i$ is the estimated state, and nb is the number of state variables, lastly is the kth replication of Monte-Carlo simulation.

$$Average\ RMSE = \frac{1}{N}\sum_{k=1}^{N}\sqrt{\frac{1}{nb}\sum_{i=1}^{nb}\frac{\left(x_{i,[k]}-\hat{x}_{i,[k]}\right)^2}{x_{i,[k]}}} \qquad (5.25)$$

Table 9: Nodal voltage and angle RMSE for a 200 case Monte-Carlo simulation with FDI attacks

Estimator	Voltage RMSE	Angle RMSE
WLS	$19.09 \cdot 10^{-3}$	$4.078 \cdot 10^{-3}$
Huber-WLS	$0.333 \cdot 10^{-3}$	$1.8043 \cdot 10^{-3}$
S-WLS	$2.44 \cdot 10^{-3}$	$7.39 \cdot 10^{-3}$
MM-WLS	$2.4376 \cdot 10^{-3}$	$8.11 \cdot 10^{-3}$

Figure 11 shows the amount of correctly identified bad data. In Table 9, the bus voltage magnitude and angle RMSEs for each estimator are shown. All estimators prove to be highly resistant to FDI attacks in the measurement vector. As identified in the literature, FDI attacks and bad data within the measurement vector can be detected with the LNR technique allowing all estimators to retain resiliency for the measurement with FDI. All estimators are theoretically resistant to measurements outliers.

5.3.2   Distribution State Estimation of the IEEE 13-Bus System Under Topology Attacks

Topology errors and attacks are more challenging than measurement attacks. This section investigates the robustness of the S- and MM-estimators under this type of attack. Within the same system and measurement setting, the bad data attacks created in the Y_{bus} impacted the topology or the H matrix (Jacobian). The goal of this attack was to simulate a scenario where the known topology of the system, such as a line, is corrupted to create errors and possible non-convergent states. Two elements in the Y_{bus} were attacked at random, and a random scaling multiplied the impedances corresponding to these indices.

Since this is a coupled three-phase system, the location of the bad data propagates to more indices within the Jacobian matrix. If the attack vector falls on a cross-coupling of a conductor, it will only propagate to the respective line. If the topology attack falls on a line or bus value. All lines and buses connected to this attack vector are also impacted. This is shown in Table 10 where there are attacks on the Y_{bus}, however it has now impacted 8 rows in the Jacobian matrix (topology matrix). For analytics,

the FDI attack on the Y_{bus} was fixed, and the magnitude of the attack was varied between 0.95-1.05% randomly through a Monte -Carlo simulation in the same fashion as the measurement FDI attacks.

Table 10: Topology attack location and magnitude

Item	Value (Row,Col)	
Bad data On Y-bus (Row,Col)	25,24 9,6	
Bad data multiplier	0.951 1.024	
Impact on H (Row,Col)	12,23 12,24 12 49 12,50	28,23 28,24 28,49 28,50
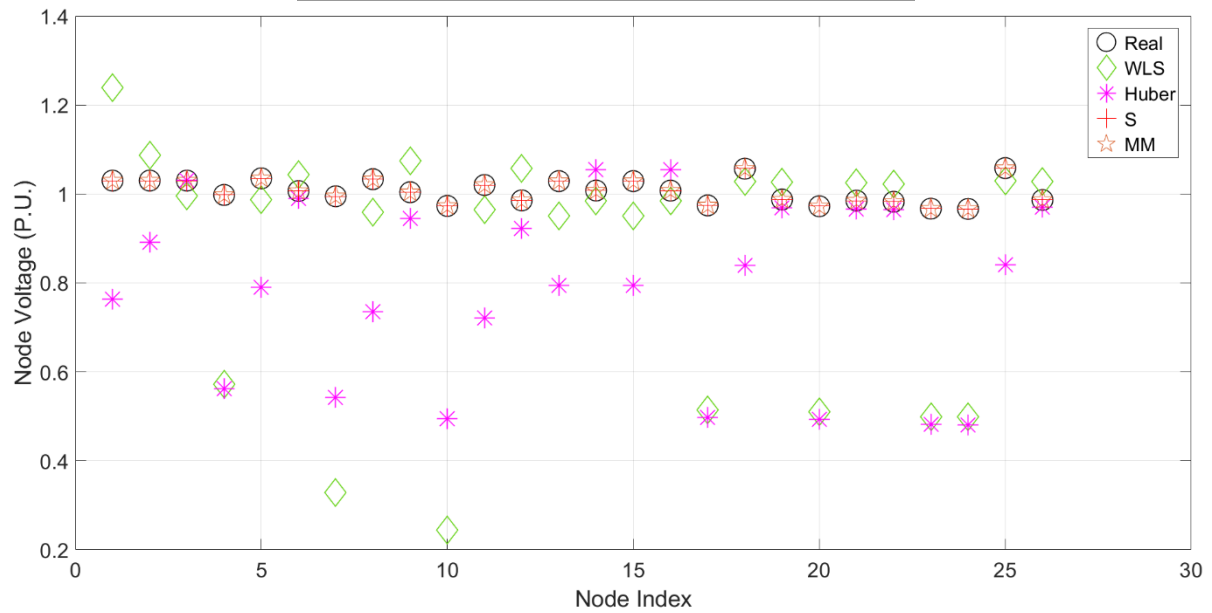
Figure 12: Nodal voltage estimate for each estimator with topology

Figure 12 displays the voltage magnitude for each estimator with its actual value for the different system nodes. Both the WLS and Huber M-estimator produce gross errors when faced with topology errors. The robust S- and MM-estimators are able to retain a robust estimate and reject the bad topology data. Below, Figures 13 and 14 provide box plots for the distribution of the RMSE errors over a Monte-Carlo simulation for both the voltage magnitude and angle over all nodes for topology attacks.
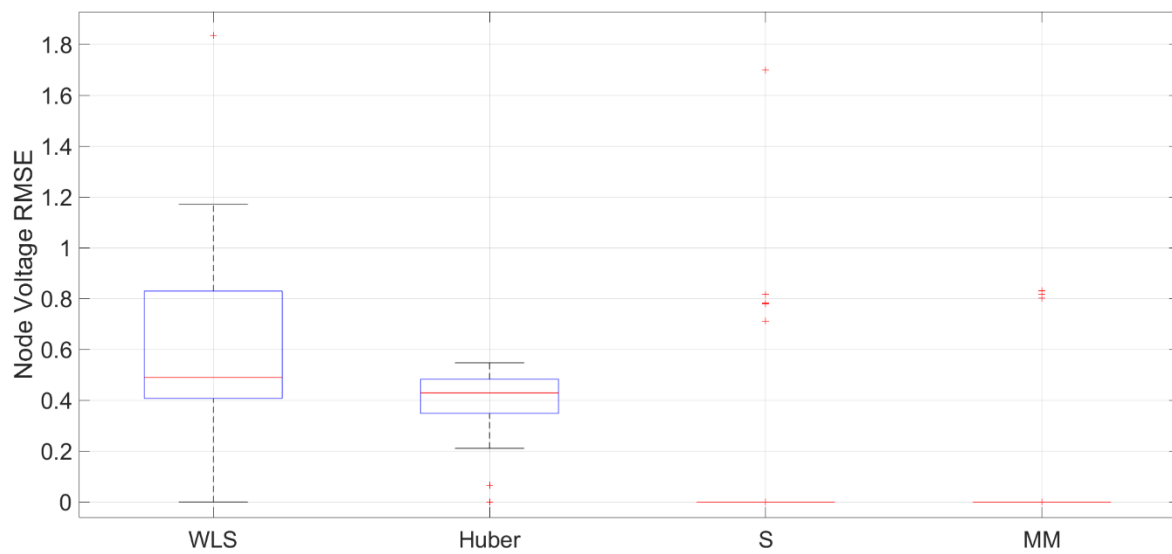
Figure 13: Node voltage RMSE for each estimator with Monte Carlo simulation for topology FDI
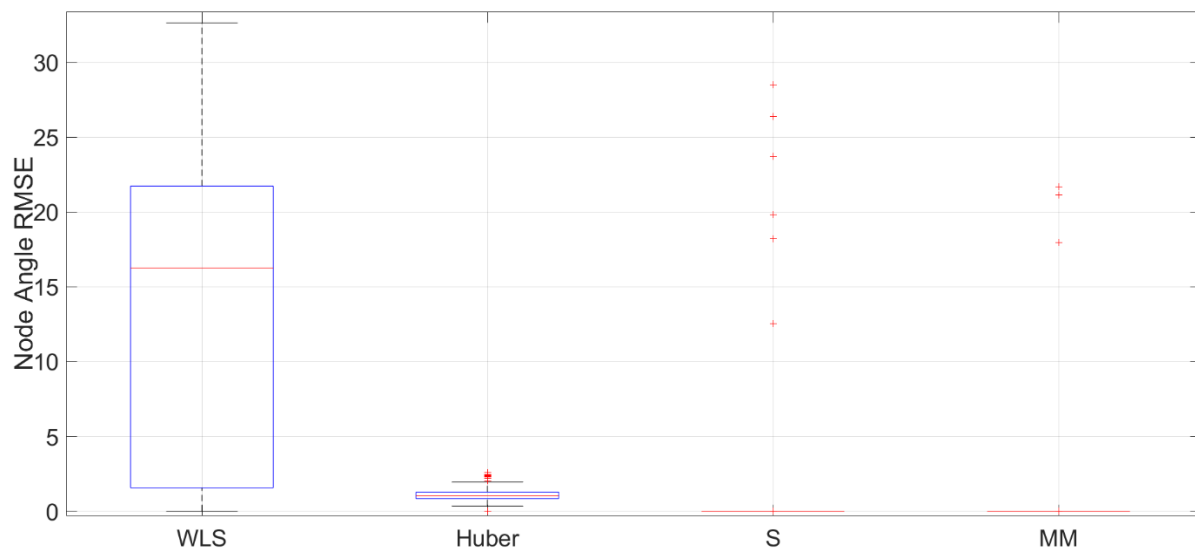
Figure 14: Node Angle RMSE for each estimator with Monte-Carlo simulation for topology FDI

Table 11: Mean RMSE for each estimator over the Monte-Carlo simulation with topology attacks

Filter	Voltage RMSE	Angle RMSE
WLS	0.48959	16.2682
Huber-WLS	0.42915	1.0203
S-WLS	$3.2338 \cdot 10^{-3}$	$7.39 \cdot 10^{-3}$
MM-WLS	$4.49136 \cdot 10^{-3}$	$8.11 \cdot 10^{-3}$

Table 11 provides the associated RMSE of the Monte-Carlo simulation for the topology attacks case. These RMSE Figures display the effectiveness of the S- and MM-estimators, which are resilient to topology errors. Additionally, it provides a metric for the performance of the WLS and Huber estimators, showing how their full breakdown in the advent of topology attacks impacts their performance. While the scaling factor of 0.95-1.05 is not a very large and impactful value, it shows the sensitivity of these estimators in the presence of topology attacks. This sensitivity and its impact can be further shown in the next section with the related DLMP prices.

5.3.2.1 Impact of FDI Errors on DLMPs

The DLMP algorithm was applied to the IEEE 13-bus model to simulate the impact of bad data on energy markets. Since μPMUs were not installed at every bus, the state estimators were leveraged to gather the voltages and angles seen at each node. The considered distribution system does not have every bus/node readily observable,. The estimation needs to be accurate and free of errors and provides values for all buses. Once the state estimators calculated the nodal states, the DLMP algorithm was applied to calculate the price of energy at each node for real and reactive power. In viewing the results from the measurement attacks from the previous section, it can be noted that there would be a minimal impact on the DLMP as these estimators are resilient to measurement FDI attacks. The primary focus of the effects of the FDI attacks on DLMP will be the Topology attacks. Tables 12 – 14 provide the DLMP values calculated given the state of the system from one Monte-Carlo replication with topology attack . The estimate produced by the WLS and the Huber M- caused the DLMP program to diverge, where N.C stands for no-convergence where the price value tended to infinity.

Table 12: DLMP Prices for Phase - A

Node	Original (c/kWh)	WLS (c/kWh)	Huber (c/kWh)	S (c/kWh)	MM (c/kWh)
632.A	10.47	N.C	N.C	10.47	10.47
633.A	10.45	N.C	N.C	10.45	10.45
634.A	10.29	N.C	N.C	10.29	10.29
671.A	9.84	N.C	N.C	9.8	9.84
684.A	9.83	N.C	N.C	9.83	9.83
652.A	9.85	N.C	N.C	9.85	9.85
675.A	9.85	N.C	N.C	9.85	9.85

Table 13: DLMP Prices for Phase - B

Node	Original (c/kWh)	WLS (c/kWh)	Huber (c/kWh)	S (c/kWh)	MM (c/kWh)
632.B	11.4135	N.C	N.C	11.4135	11.4135
633.B	11.3972	N.C	N.C	11.3972	11.3972
634.B	11.2804	N.C	N.C	11.2804	11.2804
645.B	11.3975	N.C	N.C	11.3975	11.3975
646.B	11.3988	N.C	N.C	11.3988	11.3988
671.B	11.3883	N.C	N.C	11.3883	11.3883
675.B	11.3511	N.C	N.C	11.3511	11.3511

Table 14: DLMP Prices for Phase - C

Node	Original (c/kWh)	WLS (c/kWh)	Huber (c/kWh)	S (c/kWh)	MM (c/kWh)
632.C	11.2074	N.C	N.C	11.2074	11.2074
633.C	11.2026	N.C	N.C	11.2026	11.2026
634.C	11.1680	N.C	N.C	11.1680	11.1680
645.C	11.1958	N.C	N.C	11.1958	11.1958
646.C	11.1942	N.C	N.C	11.1942	11.1942
671.C	10.8003	N.C	N.C	10.8003	10.8003
684.C	10.7650	N.C	N.C	10.7650	10.7650
611.C	10.7176	N.C	N.C	10.7176	10.7176
675.C	10.7290	N.C	N.C	10.7290	10.7290

As these voltages become corrupted due to the FDI Topology attacks, the full impact on the system can be noted concerning the economics of the power system. Since the WLS and Huber M- broke down in every case of the Monte-Carlo simulations, the resulting errors are large. Tables 12-14 provide a clear visual of the estimate for the S- and MM- estimators resulting DLMPs, where they have retained their estimate allowing for an accurate estimate matching the original prices.

5.3.2.2   Distribution State Estimation Discussion

The redundancy of the distribution system was reduced due to the limited application of micro-PMUs in the distribution system. For analysis, measurement and topology attacks were created on Monte-Carlo simulations to evaluate the estimators over several scenarios. The computation time is recorded over the Monte-Carlo replications, and the resulting distribution of computation times are found below in Figure 15 and Table 15. At each replication, the estimators are initialized to a flat start, such that the voltages are 1 Per Unit and the angles are 0 deg, all estimators are iterative until convergence to a solution.
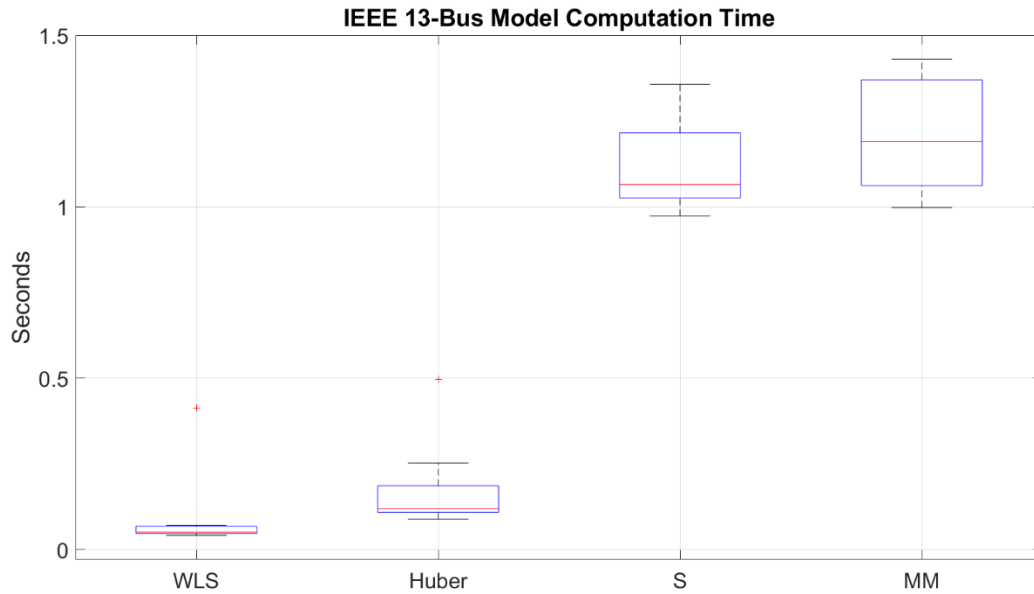
Figure 15: IEEE 13-bus model Computation Time

Table 15: Mean computation time for IEEE 13-bus model

Estimator	Computation Time (s)
WLS	0.0508
Huber-WLS	0.1185
S-WLS	1.065
MM-WLS	1.191

In summary, it has been noted in Table 9 and Figure 11 that all estimators are resilient to measurement FDI attacks when paired with the LNR bad data test. However, in the simulations for the topology attacks, it became evident that the topology attacks heavily impacted the WLS and Huber M- estimators energy causing the trading DLMP calculation to diverge. The S- and MM-estimators are highly effective for both types of attacks. The execution time we obtained seems acceptable since this is a static state estimator, but further investigation is needed for larger distribution systems.

Chapter 6   High Breakdown Point Robust Dynamic State Estimation for Transmission Systems

This chapter applies the UKF, the robust Huber M-based UKF, and the proposed robust S-based and MM-based UKF estimators to the transmission of IEEE 14-, 57-, 118-bus systems. All estimators will be implemented as centralized DSE in the first section to test their robustness and computation time. The second section illustrates the proposed robust decentralized dynamic state estimators' performance on the same transmission systems. A comparison of the decentralized DSE against the centralized DSE is provided.

6.1   Centralized Transmission Dynamic State Estimation

The dynamic simulations were generated using the MATLAB code provided in [73]. The S- and MM-regression estimators algorithms are provided in [98]. The dynamic states of the system are the speed (w) and angle (delta) of the generators [73], where the controls of the generators are neglected over the short transients. We have evaluated the estimators on the IEEE-14, 57-, and 118-bus systems provided by MATPOWER [82]. Due to space limitations, the simulations on the IEEE 57- and 118-bus systems will be shown in this first section. A series of tests are conducted to show the impact of bad data on each filter. Each test case will be evaluated using simulation in the three following scenarios:

1. The measurement vector contains clean PMU data with Gaussian noise to evaluate a baseline error in the presence of non-attacked measurement signals

2. The measurement vector containing PMU signals is corrupted due to accidental erroneous measurements or malicious FDI attacks.

3. The admittance matrix in the filters is corrupted to simulate topology errors.

The usual assumption is that the noise in the state representation is independent and identically distributed (i.i.d) Gaussian. In [116], researchers at PNNL indicated that real-life communication and measurement devices give an observed noise in PMUs which is not Gaussian. We used a Gaussian mixture model distribution to generate the measurement noise to evaluate the filters with data following approximately a Gaussian. The Gaussian mixture distribution is given by $(1 - \varepsilon)N(0, \sqrt{2}) + \varepsilon N(7,1)$ where $\varepsilon = 0.09$ and $N(\mu, \sigma)$ is the Guassian distribution with mean μ and standard deviation σ. We used the Gaussian mixture generator gmdistribution in MATLAB [117]. the mixture Gaussian distribution variable is generated and multiplied by 10^{-3} Per Unit to generate the final measurement noise.

6.1.1 Centralized IEEE 57-Bus Test Case

Within the IEEE 57-bus model, there are 14 dynamic states (angle and speed of generators) modeled by the swing equations and 114 algebraic states (voltage and angle of the buses). Figure 16 shows the one-line diagram of the IEEE 57-bus model [118].
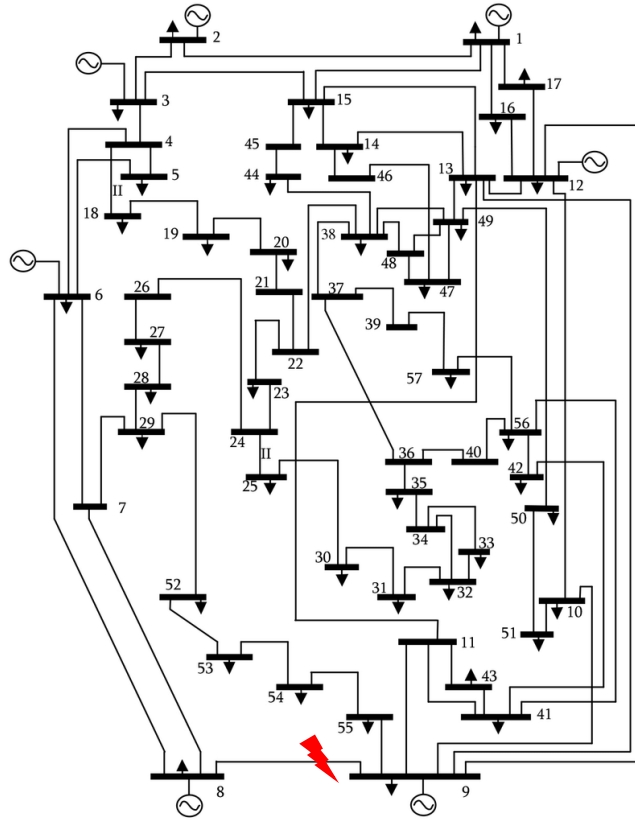
Figure 16: IEEE 57-bus model with the location of open line between bus 8-9 [119]

6.1.1.1   Measurement FDI

In this scenario, bad data is introduced into the measurements of the system in the vector $z_k^c(I)$ as given by (6.1). The scaling factor $C_k(i)$ is a random variable following a uniform distribution $U(0,1)$. Where $z_k(i)$ is the true measurement and $v_k(i)$ is the Gaussian mixture distribution indicated above.

$$z_k^c(i) = z_k(i) \cdot C_k(i) + v_k(i) \tag{6.1}$$

The set of PMU measurement vectors is shown in (6.2) that will be attacked is determined at random. P_{gen} and Q_{gen} is the real and reactive power produced by the generators in the system, $\overline{V}$ and $\overline{\theta}$ is the bus voltage and angle respectively for all system buses. Where m indicates the total amount of generators, and n indicates the total number of buses.

$$\bar{P}_{gen} = \begin{bmatrix} P_{gen_1} \\ P_{gen_2} \\ \vdots \\ P_{gen_m} \end{bmatrix} \bar{Q}_{gen} = \begin{bmatrix} Q_{gen_1} \\ Q_{gen_2} \\ \vdots \\ Q_{gen_m} \end{bmatrix} \bar{V} = \begin{bmatrix} |V|_1 \\ |V|_2 \\ \vdots \\ |V|_n \end{bmatrix} \bar{\theta} = \begin{bmatrix} \theta_1 \\ \theta_2 \\ \vdots \\ \theta_n \end{bmatrix} z_k = \begin{bmatrix} \bar{V} \\ \bar{\theta} \\ \bar{P}_{gen} \\ \bar{Q}_{gen} \end{bmatrix} \tag{6.2}$$

Four measurements are corrupted of a specific type at random depending on the selected attack vector. Such that, a potential combination of the measurement attacks can target 4 voltage magnitudes, or three bus voltages and one real power for a generator. Once the selected test simulation is run, the bad data vectors of 100 FDI attacks are created to create a reproducible scenario. Then the different estimation methods are executed to estimate the states. Furthermore, this dynamic scenario is differentiated between the robust estimators' breakdown point designation. As the line is opened, at t=2s, the breakdown point of the robust S- and MM-estimators is changed to 0.1, or 10% to begin the robust estimation. In this simulation, there at total 14 states and 142 measurements. The simulation is run for 10s with a sample rate of 50 measurements per second.

In the following, Figures 17-21 illustrate the obtained tracking results for dynamic states such as each generator's rotor speed and angle. Line 8 between buses 8 and 9 has been opened at t=2s to create a transient. The transient persists longer since there are no exciters, governors, or power system stabilizers (PSS). After the line is opened, the FDIs are randomly generated on the measurements. To provide a visual representation of the measurement attack, Figure 17 shows the data for the power produced by generator one (PG1). It displays the corrupted data stream where the generator's power measurement has been selected to contain FDI attacks. It can be noted that when the measurement value has major errors in the data stream, it could be eliminated during a sanity check. One objective of the proposed estimators is to resist those clear and errors that are less obvious.
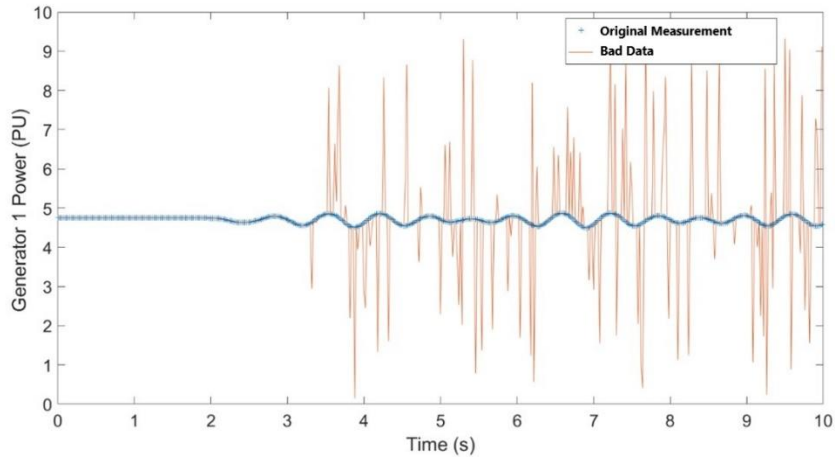
Figure 17: Measured real power supplied by generator 1 in the IEEE 57-bus system
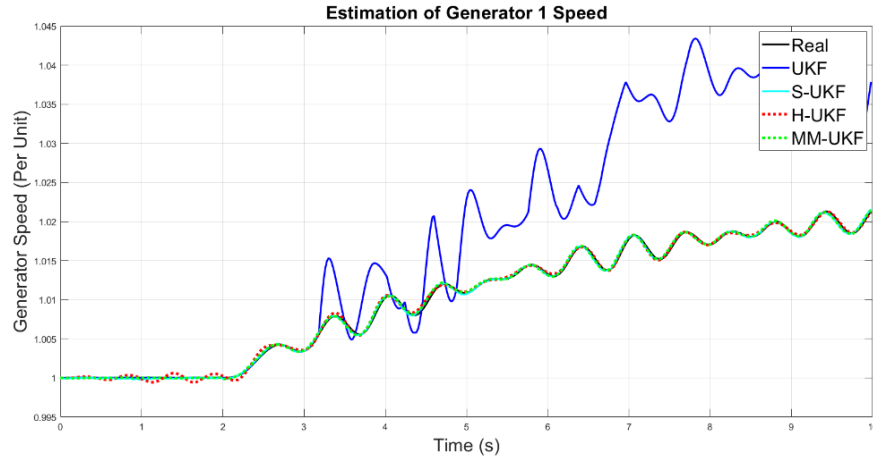
Figure 18: Centralized IEEE 57-bus model generator 1 speed estimation under measurement FDI
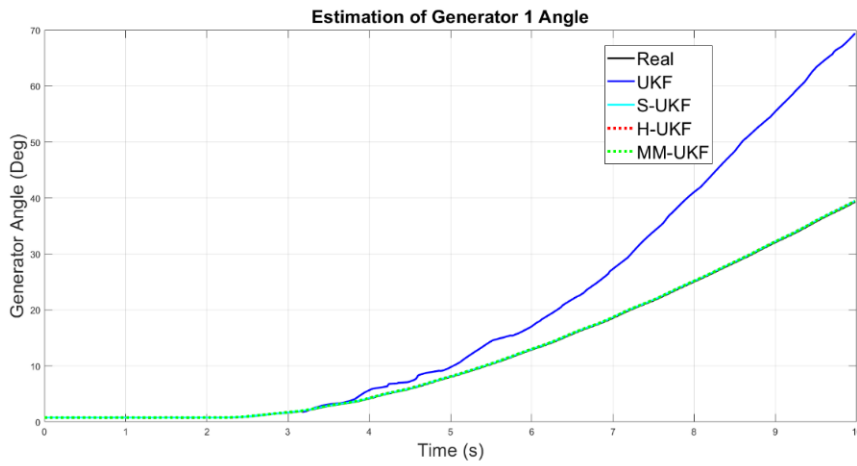
Figure 19: Centralized IEEE 57-bus model generator 1 angle estimation under measurement FDI
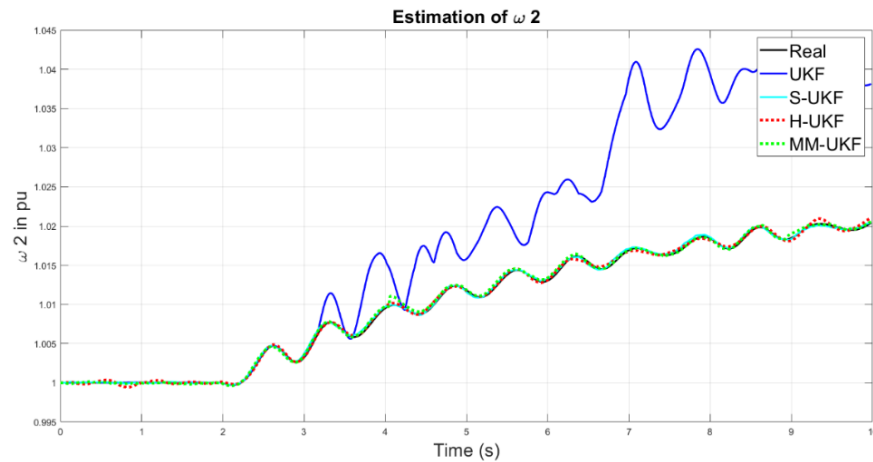
Figure 20: Centralized IEEE 57-bus model generator 2 speed estimation under measurement FDI
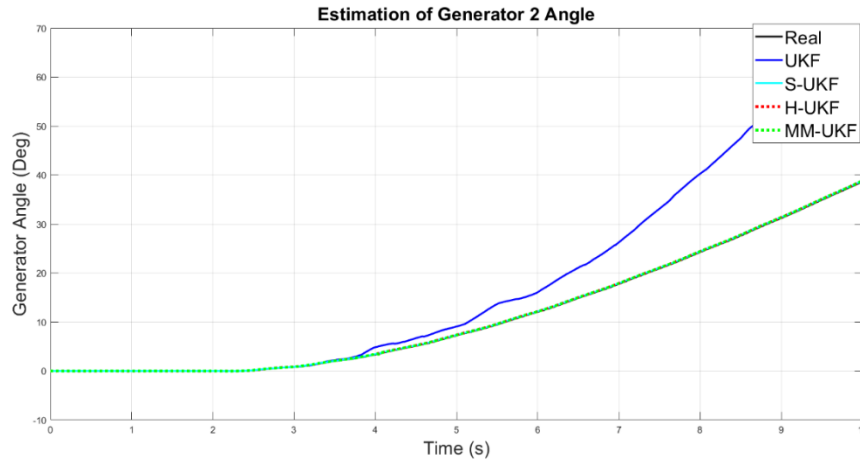
Figure 21: Centralized IEEE 57-bus model generator 2 angle estimation under measurement FDI

Table 16: Centralized IEEE 57-bus model generator RMSE with measurement FDI

Estimator	Clean Generator Speed RMSE	Generator Speed RMSE	Clean Generator Angle RMSE	Generator Angle RMSE
UKF	$2.2154 \cdot 10^{-4}$	0.0089	0.0828	7.0571
H-UKF	$2.8056 \cdot 10^{-4}$	$2.8056 \cdot 10^{-4}$	0.0829	0.0829
S-UKF	$2.1339 \cdot 10^{-4}$	$2.1339 \cdot 10^{-4}$	0.0833	0.0833
MM-UKF	$2.0828 \cdot 10^{-4}$	$2.0828 \cdot 10^{-4}$	0.0827	0.0827

From Figures 19 and 21, the UKF does not track the state accurately due to the presence of FDI attacks. The UKF has good performance when the measurements have a Gaussian noise and are not corrupted by FDI attacks. This shows the unreliability of the UKF in the presence of bad data in the measurements. Robust estimators such as the Huber M-, S-, and MM-based UKF estimators can resist the effects of bad data. Secondly, Table 16 indicates the RMSE of each estimator of related states over the duration of the simulation as indicated in (6.3).

Such that, the average RMSE was calculated again to provide the relative error of the estimators. Equation (6.3) indicates the average RMSE calculation for the dynamic scenario where i is the variable, N is the number of Monte-Carlo simulations, x_i is the actual state, and $\hat{x}_i$ is the estimated state, and nb is the number of state variables, lastly T is the total number of simulation time steps, and t is the time index. This combined RMSE will be used throughout the remaining dissertation for generator speed, generator angle, bus voltage magnitude, and bus angle.

$$Average\ RMSE = \frac{1}{T}\sum_{t=1}^{T}\sqrt{\frac{1}{nb}\sum_{i=1}^{nb}\left(x_{i,[t]} - \hat{x}_{i,[t]}\right)^2} \tag{6.3}$$

In Table 16, the UKF performance degrades as indicated by the larger RMSE values exceeding 0.02 and 18 for the speed and angle, respectively. The deviation of the rotor speed is much smaller than the deviation of the generator angle. This is due to the rotor speed being presented in per unit, and the angle in degrees. In Figure 22, the iteration computation time for each estimator is illustrated. The PC utilized for these simulations used an Intel(R) Core(TM) i7-10750H CPU @ 2.60GHz with 16GB of RAM. This recorded time was over the entirety of the estimator, such that the time recorded for the S-UKF includes a prediction and correction step. The average of these times can be found in Table 2 for a simulation over 10 seconds with a PMU reporting rate of 50 measurements per second.
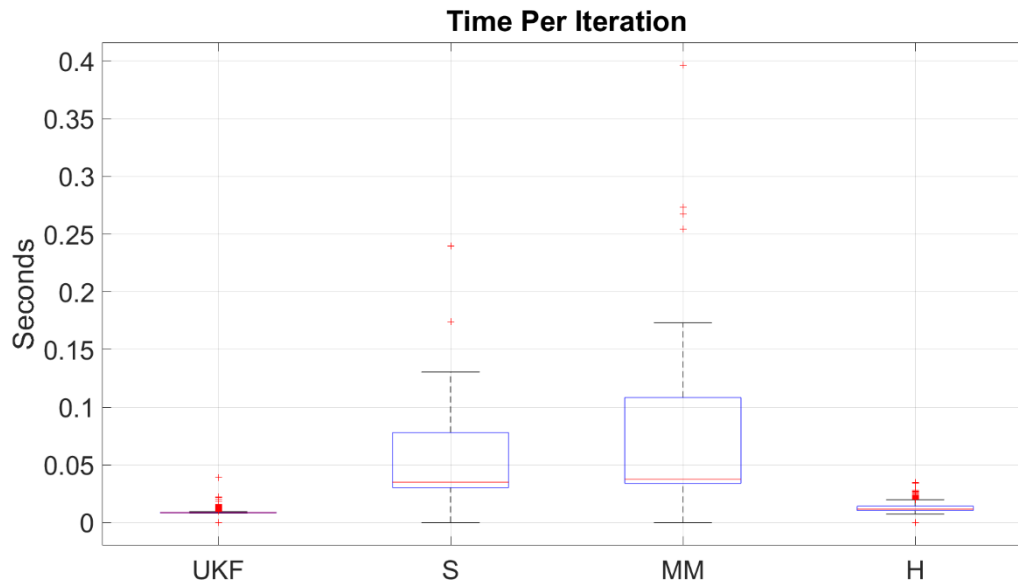
Figure 22: Distribution of iteration time for the Centralized IEEE 57-Bus model

Table 17: Mean per iteration per filter for the Centralized IEEE 57-bus model

Time Per Iteration	Time (s)
UKF	0.0089
H-UKF	0.0175
S-UKF	0.033
MM-UKF	0.036

In observing Figure 22 and Table 17, the addition of the robust estimators does increase the computation time and decrease the speed of the UKF. One important note is that each estimator uses the same LNR method for detecting and removing the bad data. Therefore, the speed of each estimator is also inhibited

due to the cycle process of removing the bad data. This simulation on the IEEE 57-bus model with measurement FDI confirmed the non-robustness of the UKF. The computation time for a smaller system such as the IEEE 57-bus system shows that processing bad data in the filter increases computation time.

6.1.1.2   IEEE 57-bus model Topology Corruption

Topology attacks were also conducted to test the hypothesis that the S- and MM- estimators are resilient against this type of attacks. In this case, the IEEE 57-bus model had the same line disconnected to create a transient on the power system, line 8-9. Secondly, topology attacks were created as indicated below in equations (6.4)-(6.5). $C_k(i)$ is a random scaling factor following a uniform distribution $U(0,1)$. Additionally, $L_k(i)$ is the impedance of a line selected at random to be corrupted where i designates the line number. The index k indicates the bad data appearance time.

1. Select a specific line for topology attack and modify the line impedance.

$$BD_{Line_{idx}}(i) = L_k(i) * C_k(i) \tag{6.4}$$

2. Rebuild the Y_{bus} matrix for the system to find $Y_{bus_{corrupted}}$

3. Replace the reduced multi-machine matrix with the corrupted matrix in the filter

$$\widehat{Y} = \left(Y_{nn} - Y_{ns} Y_{bus_{corrupted}}^{-1} Y_{sn} \right) \tag{6.5}$$
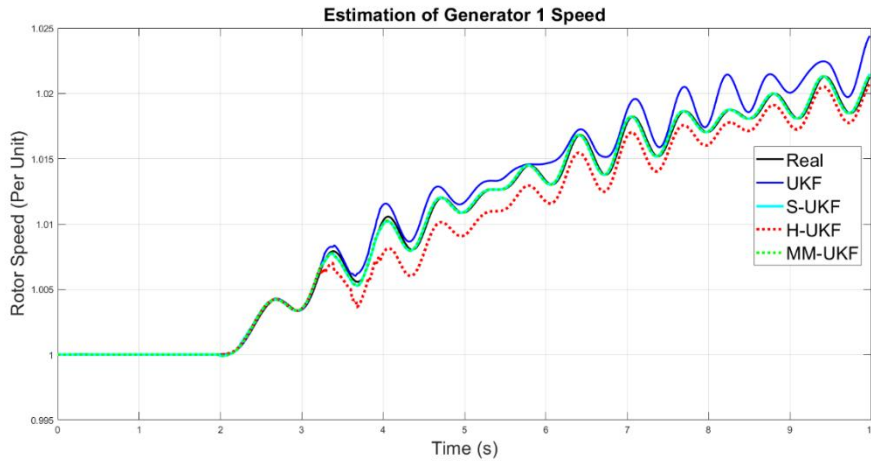
Figure 23: Centralized IEEE 57-bus model generator 1 speed estimation under topology FDI
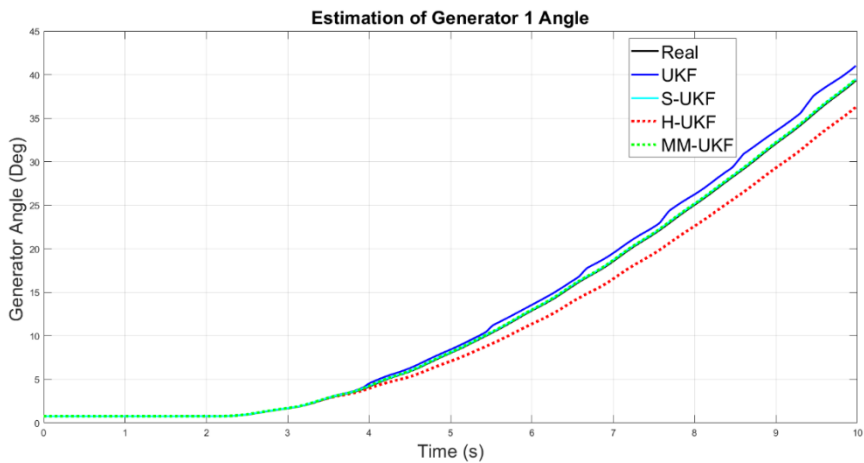
Figure 24: Centralized IEEE 57-bus model generator 1 angle estimation under topology FDI
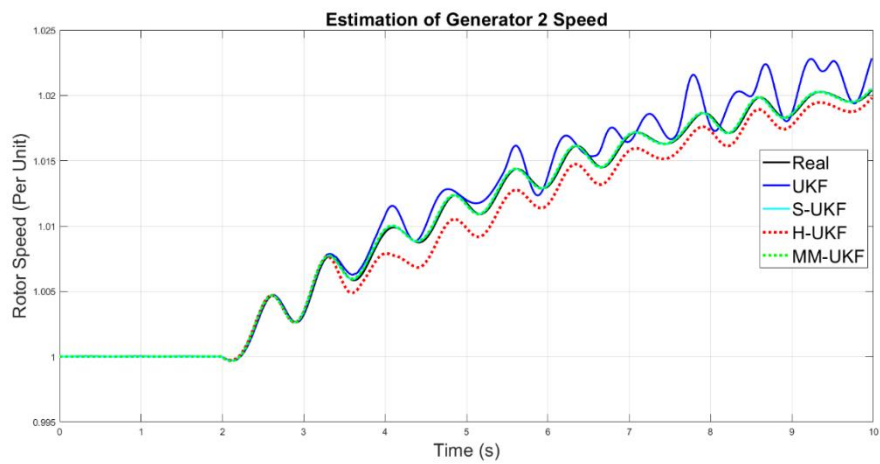
Figure 25: Centralized IEEE 57-bus model generator 2 speed estimation under topology FDI
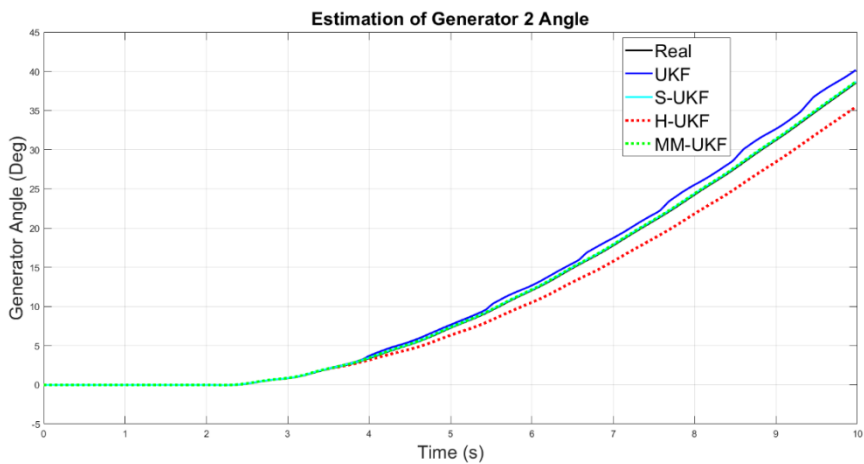
Figure 26: Centralized IEEE 57-bus model generator 2 angle estimation with topology FDI

Table 18: Centralized IEEE 57-bus model generator speed and angle RMSE for topology FDI

Estimator	UKF	Huber-UKF	S-UKF	MM-UKF
Clean Generator Speed RMSE	$2.2154 \cdot 10^{-4}$	$2.8056 \cdot 10^{-4}$	$2.1339 \cdot 10^{-4}$	$2.0828 \cdot 10^{-4}$
FDI Generator Speed RMSE	0.0028	0.0023	$3.5351 \cdot 10^{-4}$	$3.3122 \cdot 10^{-4}$
Clean Generator Angle RMSE	0.0828	0.0829	0.0833	0.0827
FDI Generator Angle RMSE	15.794	3.0223	0.0837	0.0829
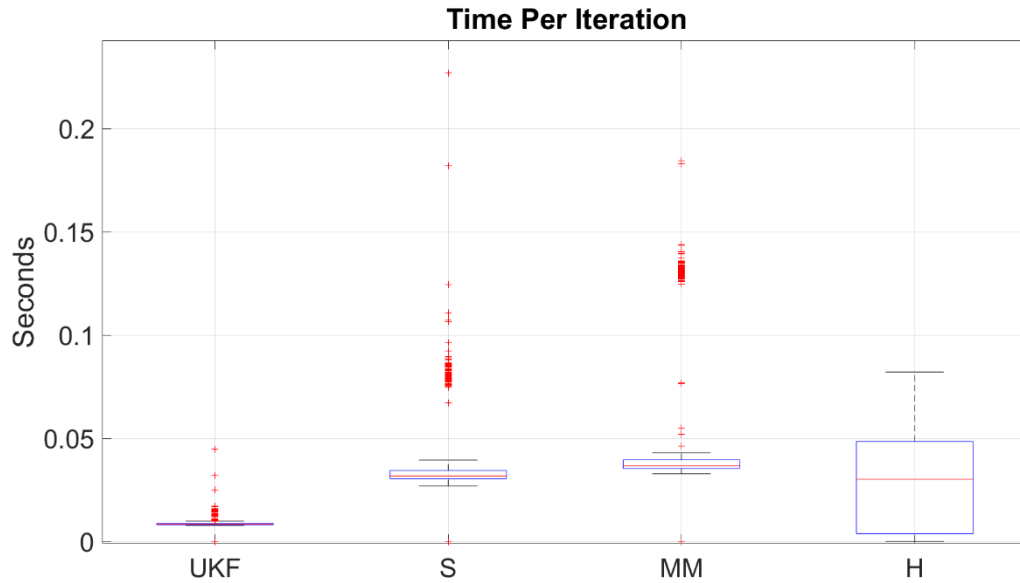
Figure 27: Centralized IEEE 57-bus model time per iteration under topology attacks

Table 19: Mean iteration time per estimator for the Centralized IEEE 57-bus model

Time Per Iteration	Time (s)
UKF	0.0089
H-UKF	0.029
S-UKF	0.034
MM-UKF	0.038

Figures 23-27 depict the states of the same two generators considered in the previous section. Both the UKF and the Huber M-based UKF did not provide robust state estimates in the presence of topology attacks. While the estimators did not completely diverge in the speed states, the tracking of the angles of the generators degraded significantly, which can be noted in the elevated RMSE as indicated in Table 18. Table 18 provides the mean iteration time of each estimator. Due to the smaller nature of the IEEE 57-bus model, the estimators provide times that are similar to times found in the literature [75] for small

systems. It should be noted that the iteration times recorded are for the total estimators' step, where the S-UKF includes the time of the execution of the S- and the correction and the prediction of the UKF.

6.1.2   *Centralized Dynamic State Estimation Applied to the IEEE 118-bus model*

After testing the IEEE 57-bus model, the IEEE 118-bus model was implemented and tested in the same format. Where line 97 between bus 38 and 65 was disconnected at t = 2s, and FDI injections start randomly afterward. The primary difference between the IEEE 57-bus model and the IEEE 118-Bus model is the number of generators. Where the IEEE 118-bus model has roughly two times the busses and also has 54 generators, thus, it has 108 dynamic states compared to 14 for the IEEE 57-bus model. The primary test for this system was to observe the behavior of all filters regarding the impact of FDI on a system with a larger amount of dynamic states.
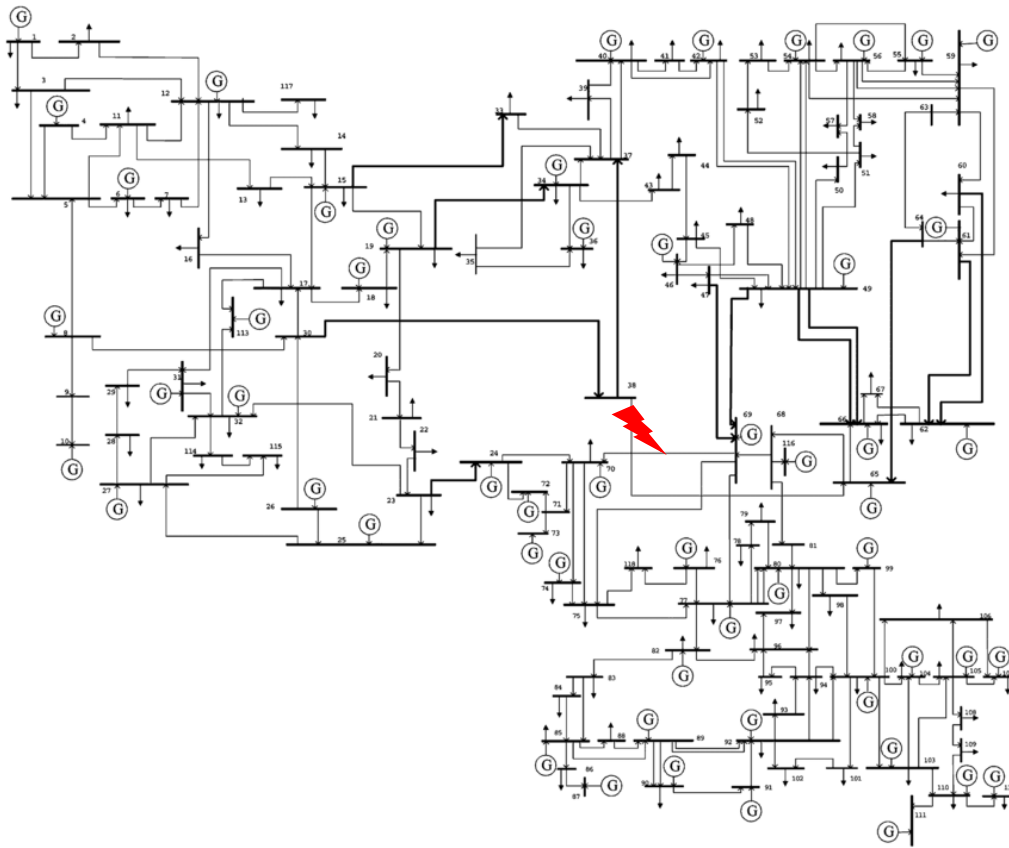
Figure 28: One-Line diagram of the IEEE 118-bus model with the location of open line [120]

6.1.2.1   IEEE 118-bus model Measurement Corruption

Similar to the IEEE 57-bus model simulations, the FDI injections are as follows: Two generators were attacked simultaneously. However, in the IEEE 118-bus model, there are 54 generators. Out of these 54 generators, 35 are synchronous condensers that supply or absorb reactive power, and 19 are generators which are supplying real and reactive power. For this simulation, there are 108 states. Figure

29 shows the per-unit power supplied by generator 5 to indicate the presence of FDI attacks. Here the FDI measurement attacks were conducted over the full system where every bus and generator has the potential for an FDI attack. For the IEEE 118-bus model there are 108 generator states, with 216 generator measurements and 236 bus measurements for a total of 452 measurements
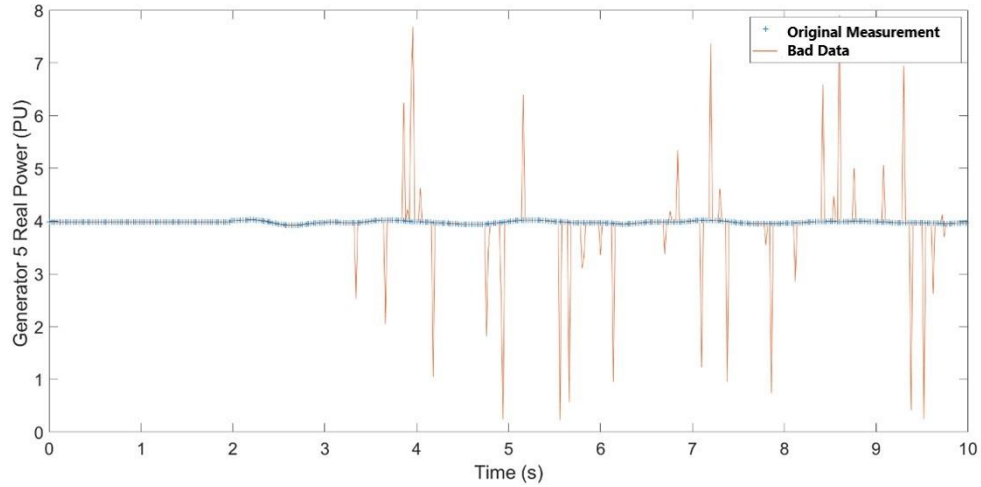
Figure 29: Measured real power supplied by generator 5 in the IEEE 118-bus system
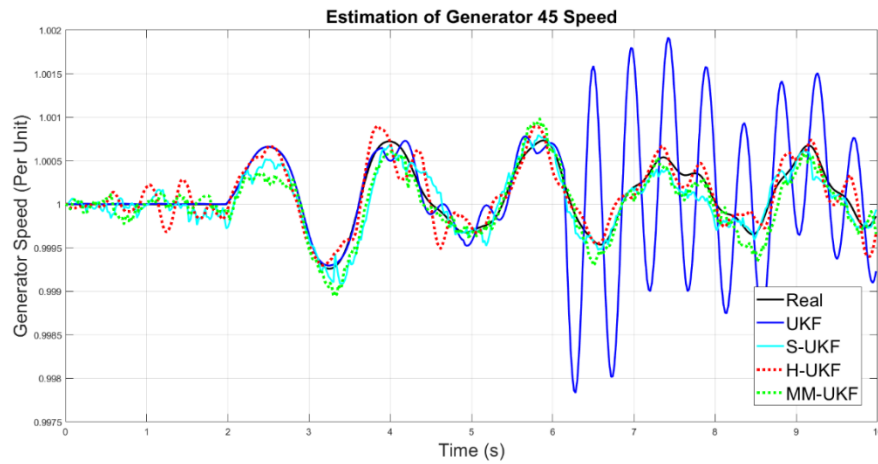
Figure 30: Centralized IEEE 118-bus model generator 45 speed estimation with measurement FDI
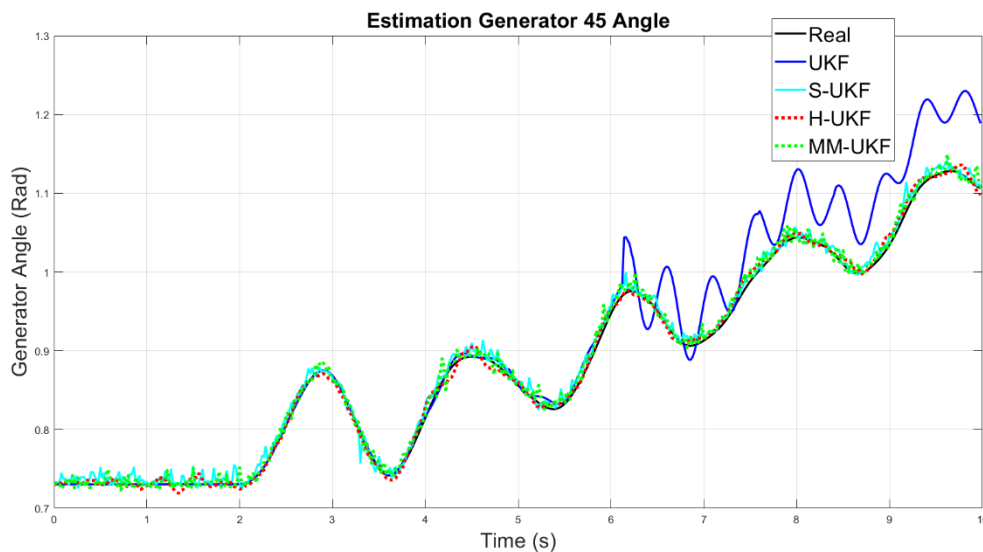
Figure 31: Centralized IEEE 118-bus model generator 45 angle estimation with measurement FDI

Table 20: Centralized IEEE 118-bus model generator RMSE for measurement FDI

Estimator	UKF	Huber-UKF	S-UKF	MM-UKF
Clean Generator Speed RMSE	$5.972 \cdot 10^{-4}$	$7.039 \cdot 10^{-4}$	$4.539 \cdot 10^{-4}$	$3.0934 \cdot 10^{-4}$
FDI Generator Speed RMSE	0.0214	$2.415 \cdot 10^{-4}$	$3.277 \cdot 10^{-4}$	$2.9447 \cdot 10^{-4}$
Clean Generator Angle RMSE	0.0035	0.0044	0.0064	0.0033
FDI Generator Angle RMSE	0.2340	0.0054	0.0062	0.0042
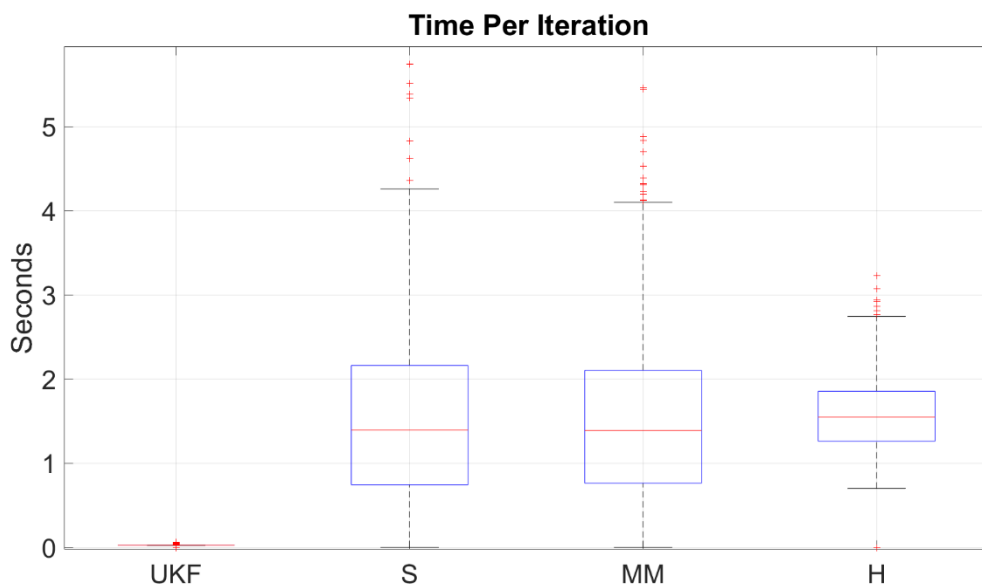
Figure 32: Total simulation time for the Centralized IEEE 118 bus model for 10s simulation

Figures 30 and 31 show similar results to the IEEE 57-bus model. The UKF degrades in the presence of FDI attacks. However, due to the number of states and related measurements, it does not fully break down. Testing the IEEE 118-bus model shows that the computation time for a system with an increased number of states, i.e., 108 states instead of the 14 in the IEEE 57-bus model, significantly increases the computation time.

Table 21: Mean per iteration per filter for the IEEE 118-bus model

Estimator	Average Iteration Time (s)
UKF	0.0276
Huber-UKF	1.5935
S-UKF	1.6777
MM-UKF	1.6288

Above in Table 21, the difference between the filters can be noticed. While the UKF diverges, it still retains a low computation time of 0.0276, a little above the simulation time step. However, the robust filters slow down with the increased states due to their higher computation expenses. It can be seen that the S- and MM-estimators slow down significantly. This is due to the computation time of the random subsamples. It takes longer to randomly find a full rank subsample when there are more states and more measurements.

6.1.2.2   IEEE 118-bus model Topology Corruption

In a similar format to the topology attacks for the IEEE 57-bus model, the IEEE 118-bus model was also used to test the attacks on a larger system. As before, the resultant topology attacks on the system are a corruption augmentation of the Y_{bus} of the system as denoted by equations (6.4)-(6.5). A total of 100 attacks throughout time were chosen.
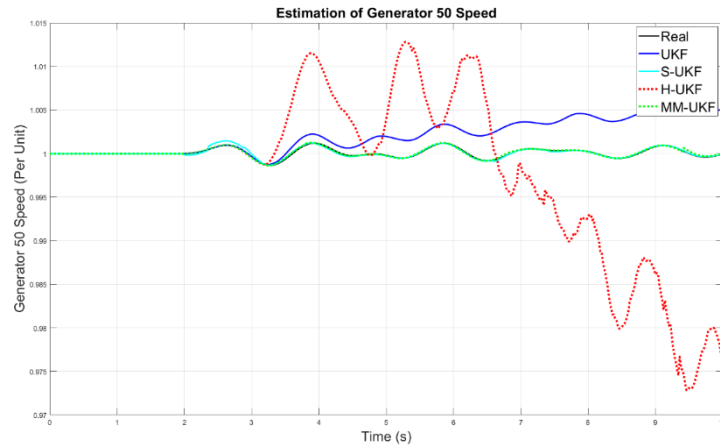
Figure 33: Centralized IEEE 118-bus model generator 50 speed estimation with topology FDI
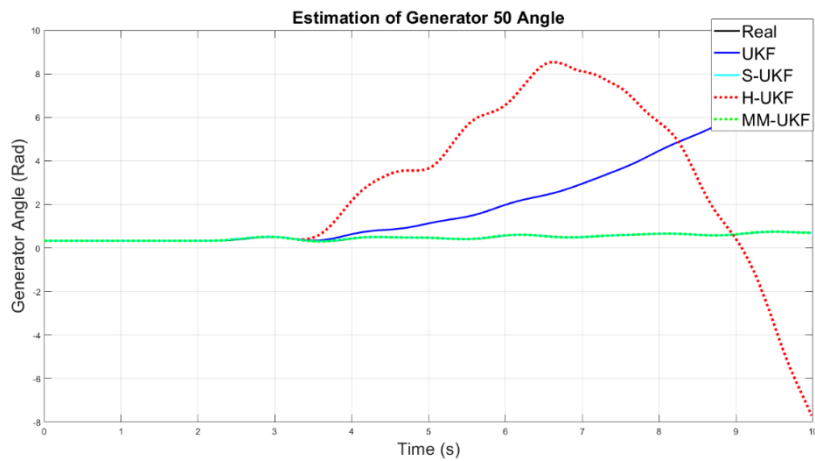
Figure 34: Centralized IEEE 118-bus model generator 50 angle estimation with topology FDI

Table 22: Centralized IEEE 118-bus model estimator RMSE for generators speed and angle states

Estimator	UKF	Huber-UKF	S-UKF	MM-UKF
Clean Generator Speed RMSE	$5.972 \cdot 10^{-4}$	$7.039 \cdot 10^{-4}$	$4.539 \cdot 10^{-4}$	$3.0934 \cdot 10^{-4}$
FDI Generator Speed RMSE	0.0019	0.1706	$1.3 \cdot 10^{-3}$	$5.1062 \cdot 10^{-4}$
Clean Generator Angle RMSE	0.00351	0.0044	0.0064	0.0033
FDI Generator Angle RMSE	1.7309	135.4004	0.054	0.034
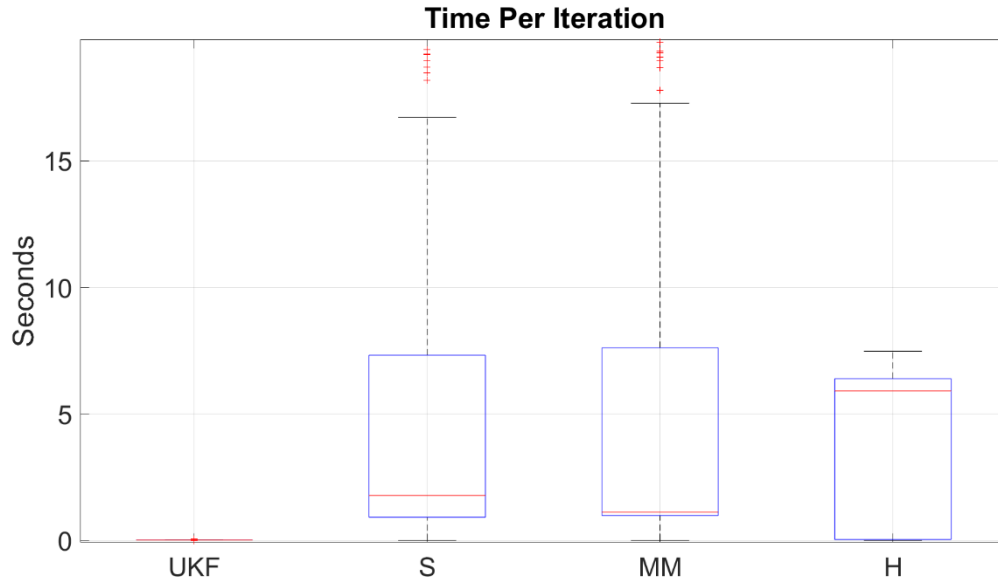
Figure 35: Iteration time for the Centralized IEEE 118-Bus model with topology FDI

Table 23: Centralized IEEE 118-bus model mean iteration time with topology FDI

Time Per Iteration	Time (s)
UKF	0.0328
H-UKF	5.914
S-UKF	1.787
MM-UKF	1.1241

Above in Figures 33 and 34, it can be noted that both the UKF and Huber-UKF have fully broken down. This was due to the multi-machine representation of the system and the reliance on the topology matrix for computations. Furthermore in Table 22, the difference between the estimators can be noticed through the RMSE errors. It is clear that the original UKF and Huber no longer provide a reliable estimate. This breakdown is reflected in Table 23 and Figure 35where the computation time has increased to 5.914 seconds for the Huber due to the Huber and the LNR method detecting too many bad data points and removing almost all measurements. The hypothesis that the S- and MM-estimators retain their robust estimate for topology attacks is confirmed and is reflected in Table 22 where the RMSE is that of the clean data.

6.2   Decentralized Transmission State Estimation

Power system decomposition has been proposed for dynamic state estimation [76] and static state estimation [21], [121], [21], [121] to enable the practical deployment of estimators on larger real systems. In references such as [21], [121], [21], [121], static state estimation resiliency of power

systems is increased. The objective is to maximize the global breakdown point of the robust static state estimator to allow for an increased number of outliers or attacks detected while ensuring the observability of the system. The increased resiliency is due to adjusting the breakdown point locally depending on the available measurement redundancy on each island. To test the full effectiveness of the robust estimators, the S- and MM-based UKF are applied to power systems in a decentralized fashion.

6.3   IEEE Test Cases Implementation and Discussion

The decentralized dynamic state robust estimators are applied to various IEEE test systems as benchmarks, i.e., the IEEE 14- and the IEEE 118-bus systems. The decentralized DSE is compared to the centralized DSE for accuracy and needed computation time. The proposed decentralized robust estimators are tested for resiliency and bad data detection evaluation.

6.3.1   Decentralized Dynamic State Estimator Applied to the IEEE 14-bus model test case

The IEEE 14-bus model consists of 14 buses and 5 generators with various loads. The IEEE 14-bus system is shown in Figure 36 and is further decomposed into cyclic and radial islands [11], [122] as designated in Table 24. A radial island is defined as a subset of buses and related topology and measurements such that it does not contain an enclosed loop. A cyclic island is a loop of buses and does not contain smaller inside cycles [118]. Therefore it's important to note the internal bus configuration may be either radial or cyclic, whereas the external system will only include tie-lines.
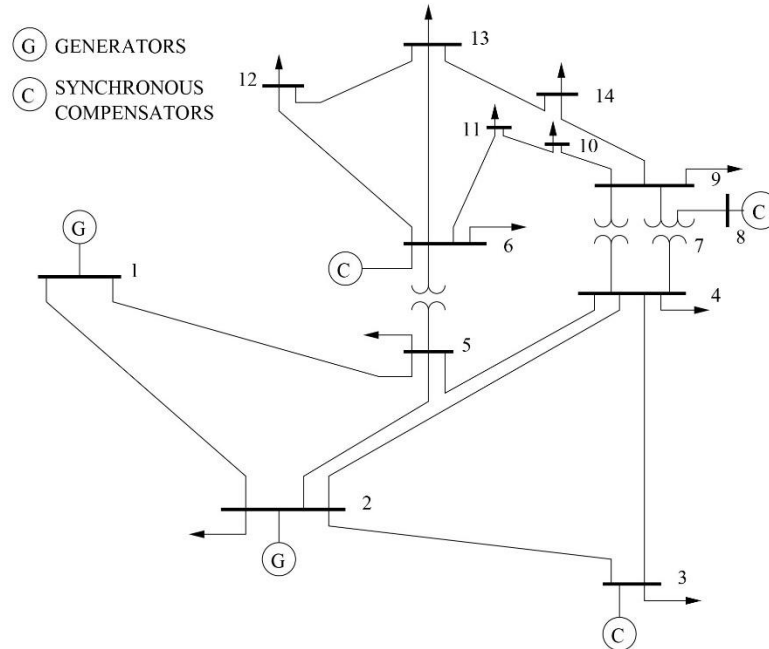
Figure 36: IEEE 14-bus model [123]

Table 24: Cyclic island designation by internal bus number for IEEE 14-Bus model

Island Number	Internal Bus Designation
1	1,2,5
2	2,4,5
3	2,3,4
4	4,7,9
5	6,12,13
6	6,9,10,11,13,14
7	4,5,6,9,10,11
8	7,8

The DSE using the UKF, the Huber M-based UKF, the S-based UKF, and MM-based UKF algorithms are implemented for each island as explained in Chapters 3 and 4. The system is simulated with clean data to determine the base RMSE and evaluate the threshold for bad data detection. The noise implemented for each measurement has an amplitude of 10^{-3} except for frequency measured at the bus, which has an amplitude of 10^{-2} for each estimator. Figures 39-47 show the estimation of island 1, which includes internal buses 1, 2, and 5 and external buses 3, 4 and 6.
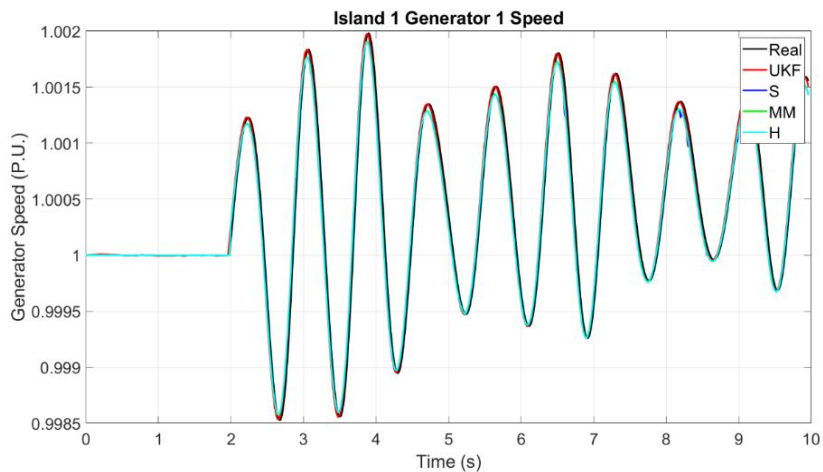
Figure 37: IEEE 14-bus model island 1 generator 1 speed estimation with clean data
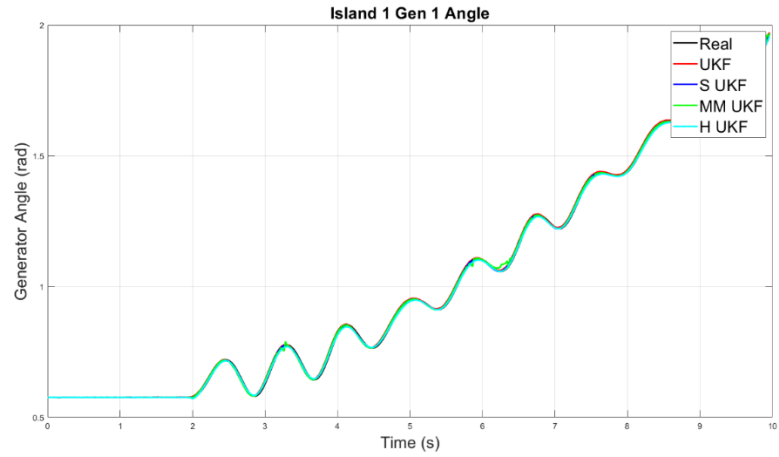
Figure 38: IEEE 14-bus model island 1 generator 1 angle estimation with clean data
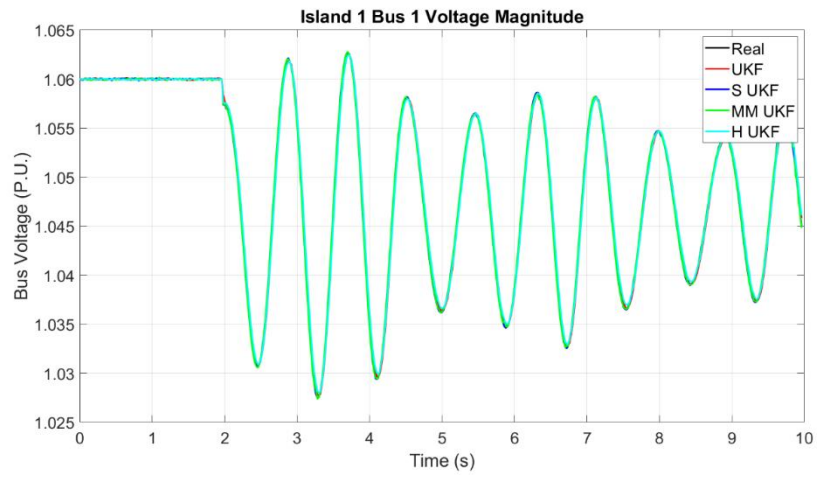
Figure 39: IEEE 14-bus model island 1 bus 1 voltage magnitude estimation with clean data
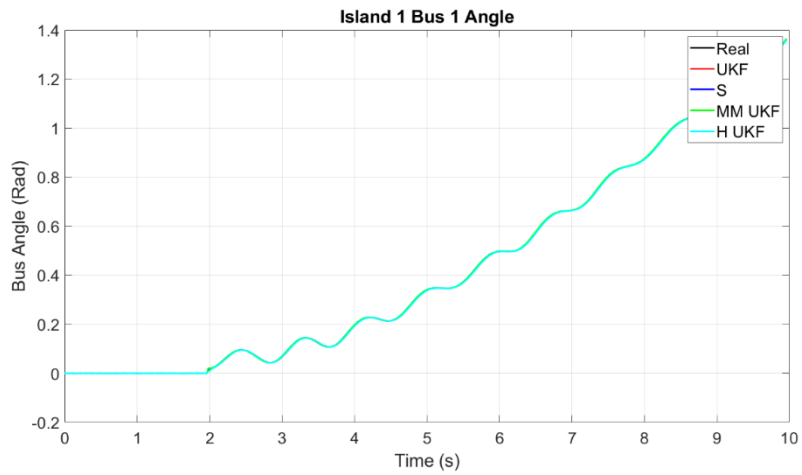
Figure 40: IEEE 14-bus model island 1 bus 1 angle estimation with clean data
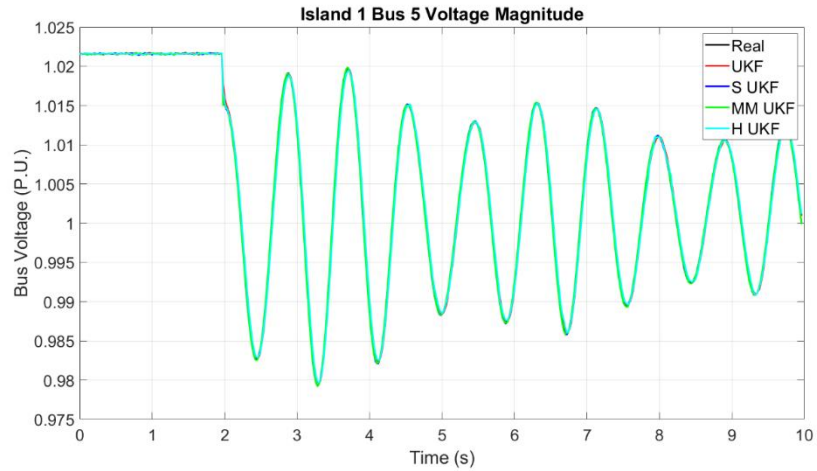
Figure 41: IEEE 14-bus model island 1 bus 5 voltage magnitude estimation with clean data
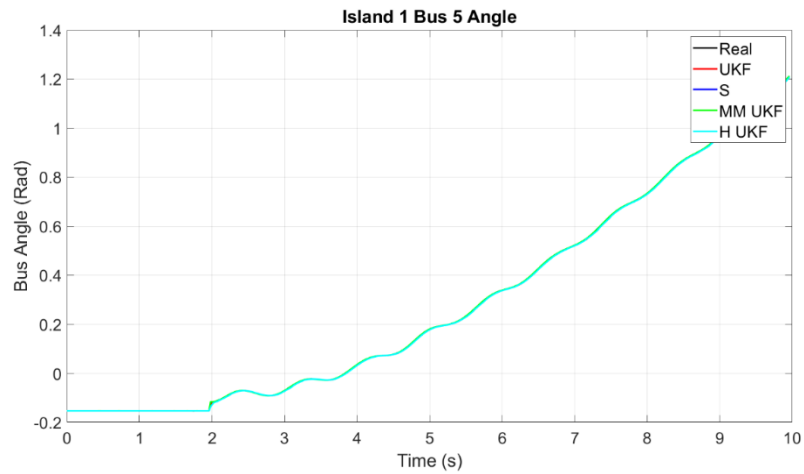
Figure 42: IEEE 14-bus model island 1 bus 5 angle estimation with clean data
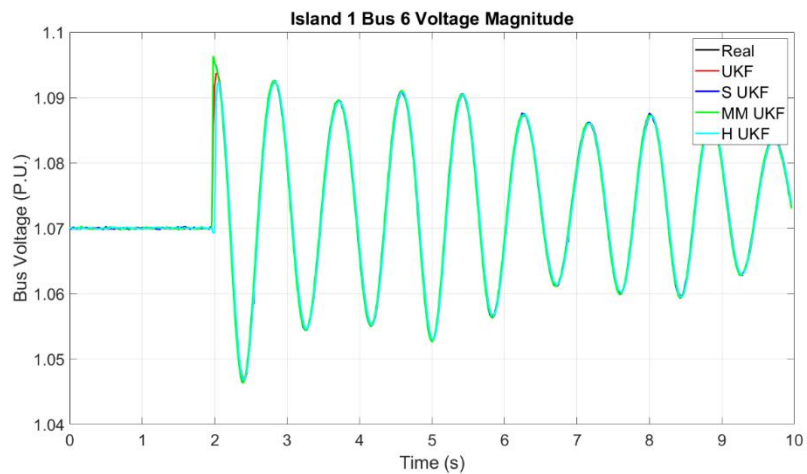
Figure 43: IEEE 14-bus model island 1 bus 6 voltage magnitude estimation with clean data
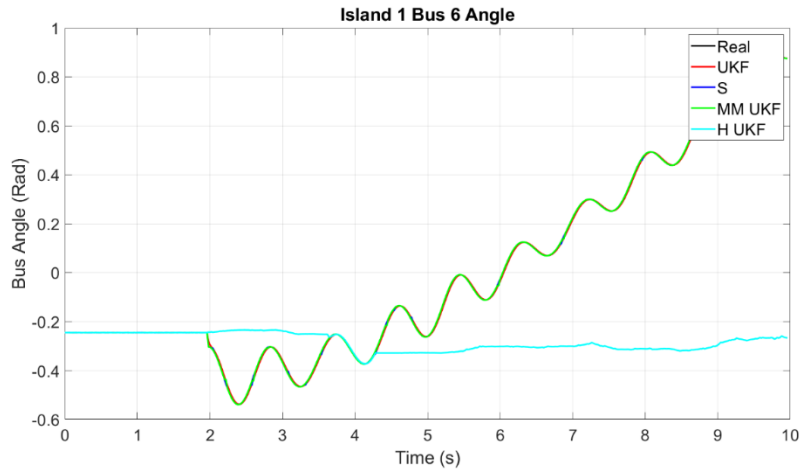
Figure 44: IEEE 14-bus model island 1 bus 6 angle estimation with clean data
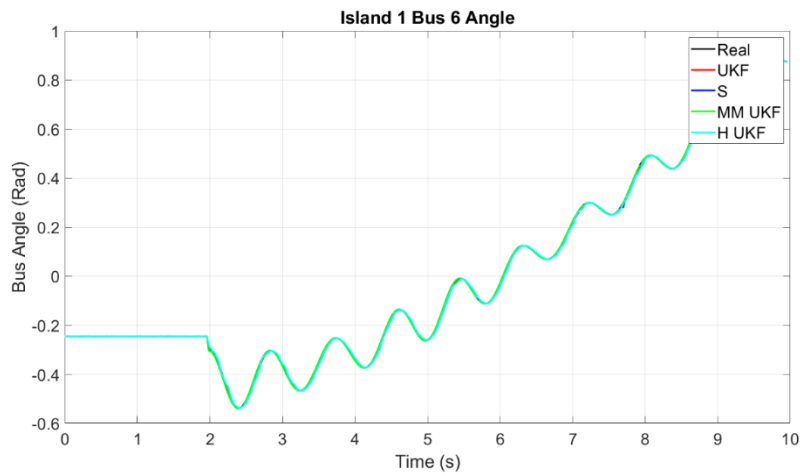
Figure 45: IEEE 14-bus model island 1 bus 6 angle estimation with clean data

Table 25: IEEE 14-bus model island 1 RMSE for dynamic generator states

RMSE	UKF	H-UKF	S-UKF	MM-UKF
Generator Speed	0.0017	0.0018	0.0024	0.0022
Generator Angle	0.0066	0.0067	0.0059	0.0059

Table 26: IEEE 14-bus model island 1 RMSE for all states contained within the island

RMSE	UKF	H-UKF	S-UKF	MM-UKF
Gen Speed 1	0.0001	0.0001	0.0001	0.0001
Gen Angle 1	0.0062	0.0061	0.0059	0.0059
Gen Speed 2	0.0001	0.0001	0.0001	0.0001
Gen Angle 2	0.0040	0.0038	0.0041	0.0039
Voltage Mag 1	0.0009	0.0004	0.0004	0.0004
Voltage Mag 2	0.0009	0.0003	0.0004	0.0004
Voltage Mag 3	0.0010	0.0009	0.0006	0.0007
Voltage Mag 4	0.0010	0.0004	0.0005	0.0005

Voltage Mag 5	0.0010	0.0002	0.0004	0.0004
Voltage Mag 6	0.0010	0.0011	0.0013	0.0014
Voltage Angle 1	0.0005	0.0005	0.0007	0.0007
Voltage Angle 2	0.0005	0.0005	0.0007	0.0007
Voltage Angle 3	0.0010	0.0006	0.0011	0.0011
Voltage Angle 4	0.0006	0.0006	0.0011	0.0011
Voltage Angle 5	0.0005	0.0005	0.0015	0.0015
Voltage Angle 6	0.0010	0.0010	0.0019	0.0012

Table 27: IEEE 14-bus model average iteration time in islands 1 and 7 with clean data

Time (s)	UKF	Huber-UKF	S-UKF	MM-UKF
Island 1	0.004061	0.01677	0.03305	0.04031
Island 7	0.01645	0.02118	0.07258	0.07872

This simulated case of the decentralized method with clean data is used =as a baseline for the RMSE error evaluation. This baseline could be used as a metric to indicate when islands have become corrupted with bad data. In examining the figures and the tables, it is important to note that the internal buses for island 1 are 1, 2, and 5, and the external buses are 3, 4 and 6. Therefore, Figure 44 and Figure 45 show that the Huber M-based UKF has broken down once the line had been disconnected between buses 5 and 6. The reason the M-based UKF has broken down is due to two variables, the loss of measurements for that island and the incorrect threshold for bad data detection. The threshold for bad data detection was determined by the average deviation of a measurement in the transient simulation found in the simulation with clean data.

6.3.1.1   Decentralized Dynamic State Estimator under Measurement False Data Injection Attacks

To test the robustness of the decentralized DSE, we inject false data into the measurement vectors at different time instants. This measurement FDI is generated by the same process as indicated in the centralized method. We use the same amount of bad data, type of corrupted data, and their magnitudes. This measurement FDI attacks are dispersed over the full IEEE 14-bus system, therefore, it's important to note that other Measurement FDI attacks may be impacting other islands. The simulations include two islands, island 1, containing buses 1, 2, and 5, and island 7 with buses 4,5,6,9,10,11. The purpose of considering these two islands is to show how the added resiliency of the islanding scheme assists in estimating internal buses. The only internal overlap between the two islands is bus 5 and the external bus overlap is 4 and 6.
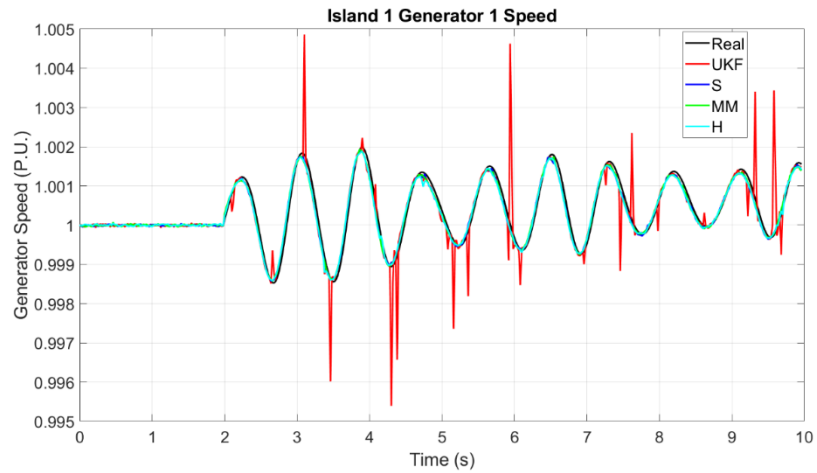
Figure 46: IEEE 14-bus model island 1 generator 1 speed estimation with measurement FDI
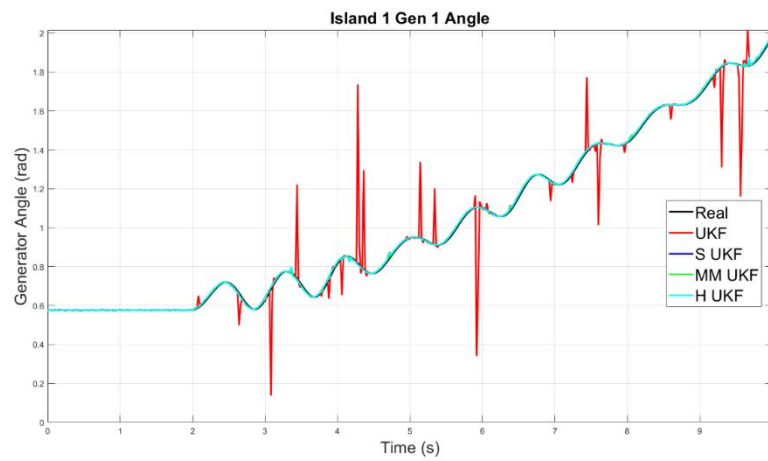
Figure 47: IEEE 14-bus model island 1 generator 1 angle estimation with measurement FDI
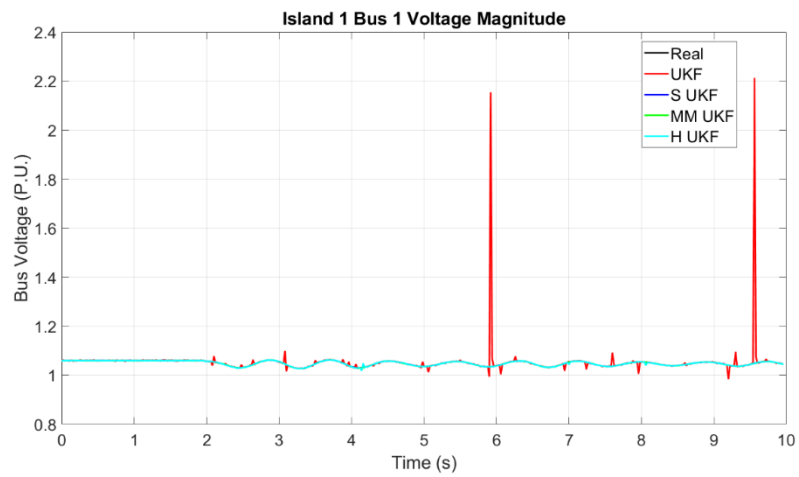
Figure 48: IEEE 14-bus model island 1 bus 1 voltage estimation with measurement FDI
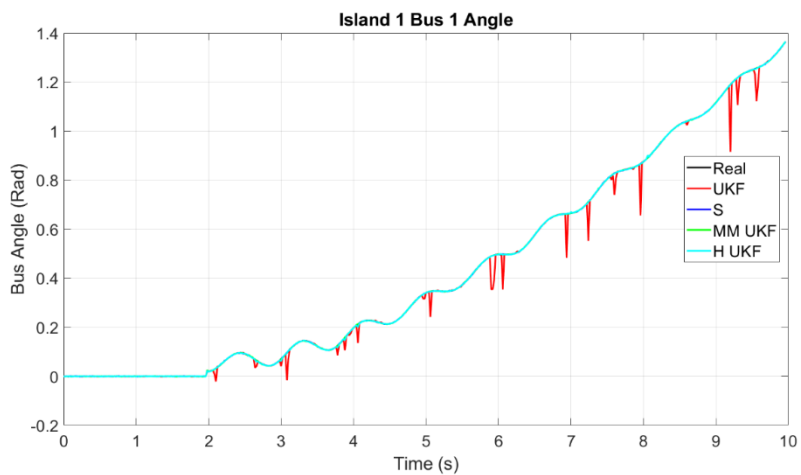
Figure 49: IEEE 14-bus model island 1 bus 1 angle estimation with measurement FDI
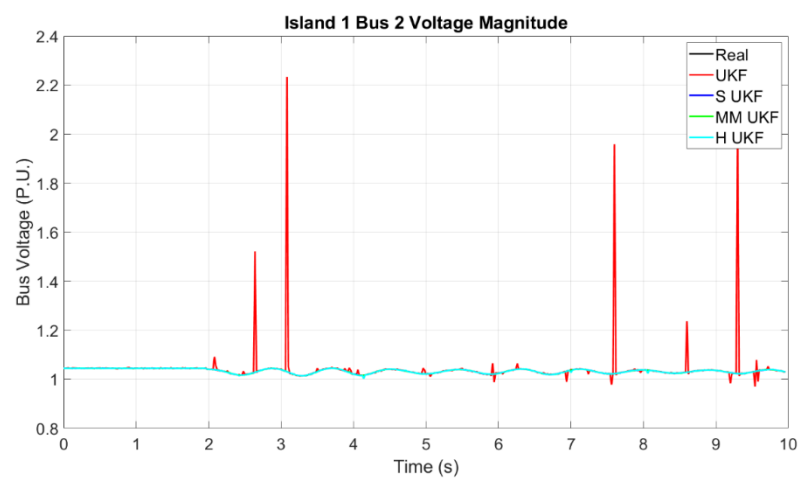
Figure 50: IEEE 14-bus model island 1 bus 2 voltage estimation with measurement FDI
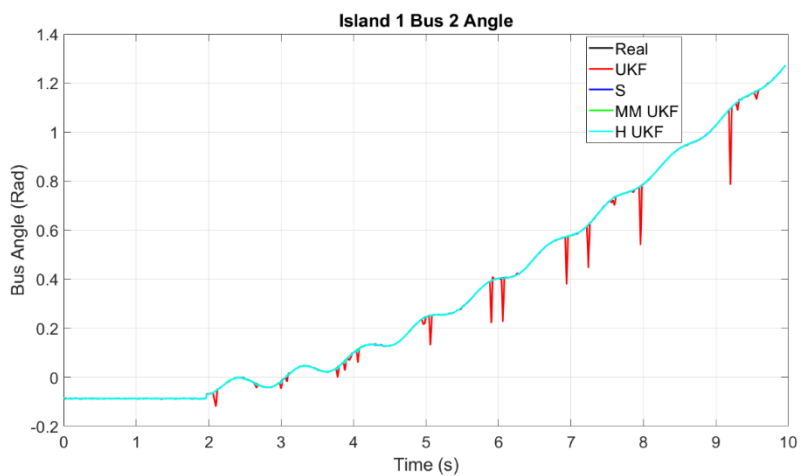
Figure 51: IEEE 14-bus model island 1 bus 3 angle estimation with measurement FDI
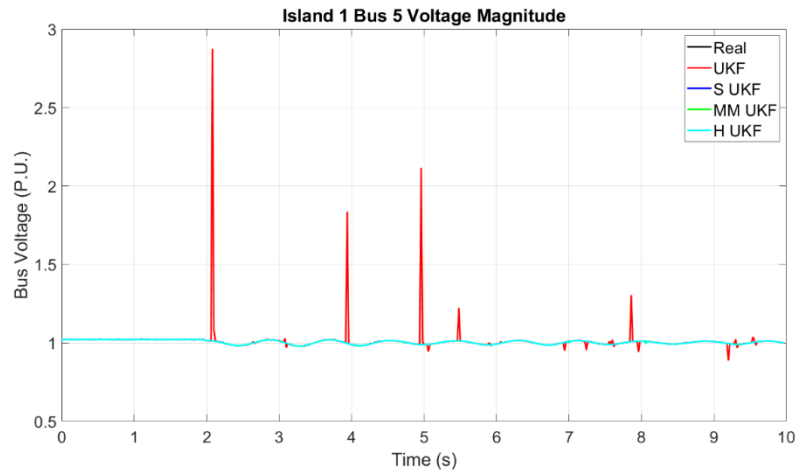
Figure 52: IEEE 14-bus model island 1 bus 5 voltage estimation with measurement FDI
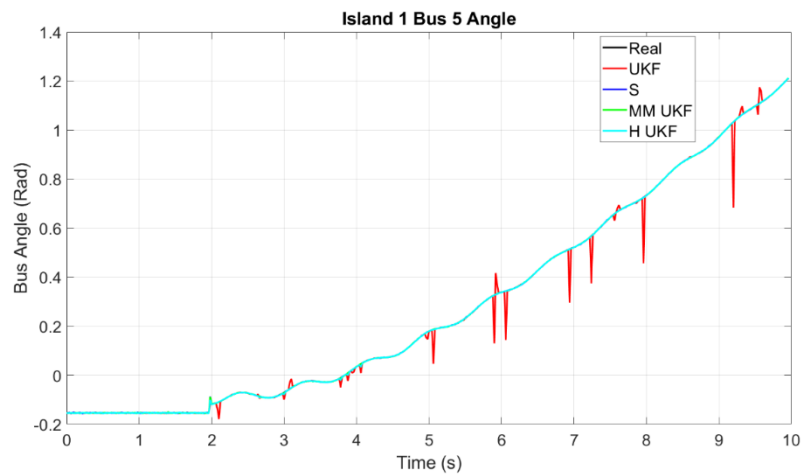
Figure 53: IEEE 14-bus model island 1 bus 5 angle estimation with measurement FDI
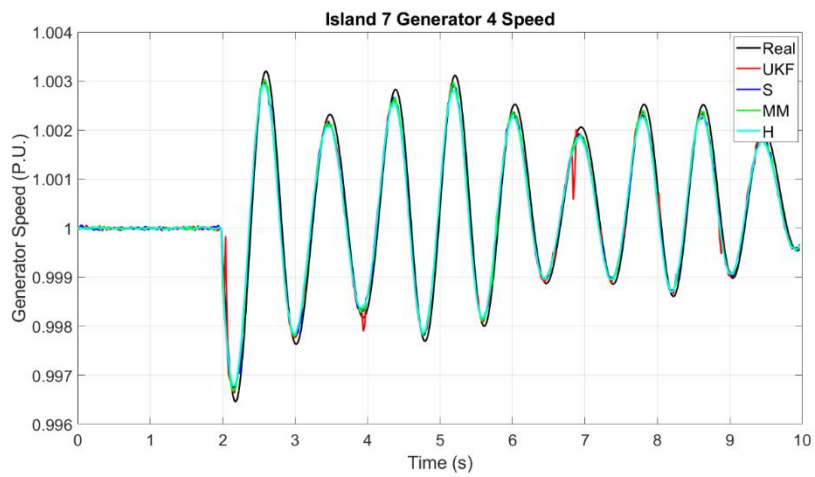
Figure 54: IEEE 14-bus model island 7 generator 4 speed estimation with measurement FDI
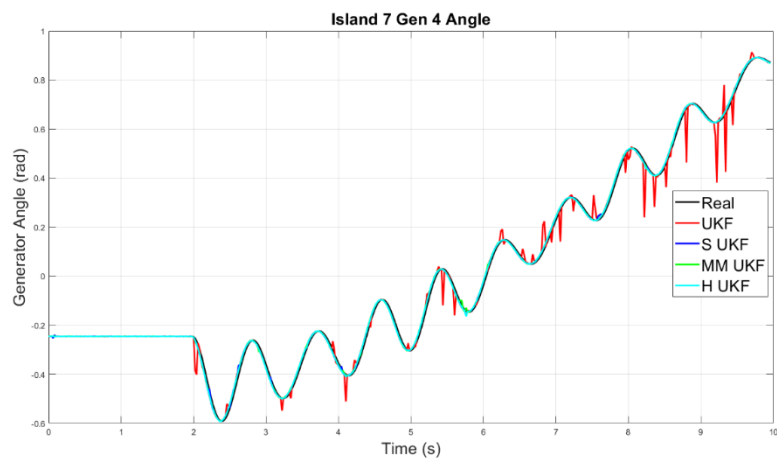
Figure 55: IEEE 14-bus model island 7 generator 4 angle estimation with measurement FDI
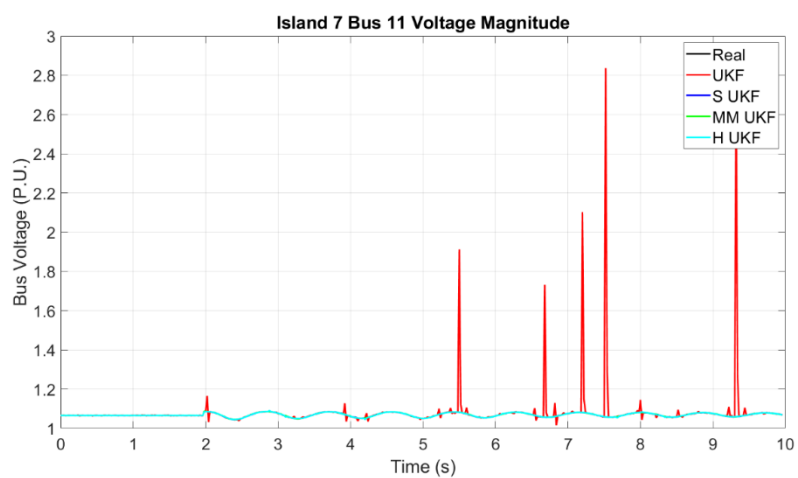
Figure 56: IEEE 14-bus model island 7 bus 11 voltage estimation with measurement FDI
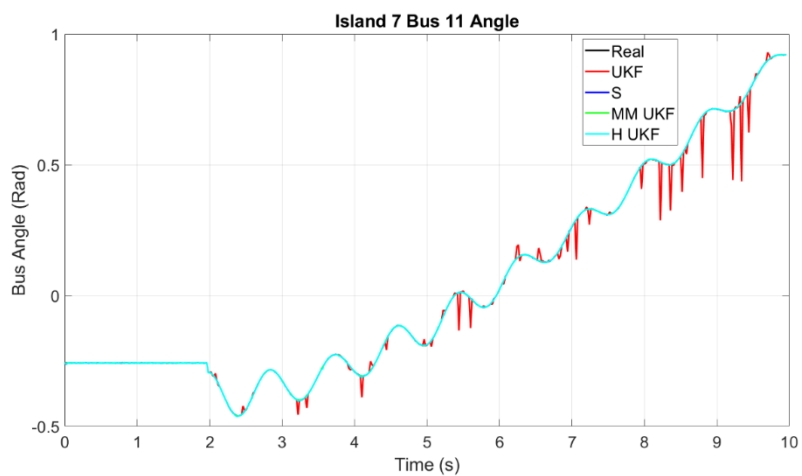
Figure 57: IEEE 14-bus model island 7 bus 11 angle estimation with measurement FDI

Table 28: IEEE 14-bus model island 1 RMSE for all states with measurement FDI

RMSE	UKF	Huber-UKF	S-UKF	MM-UKF
Gen Speed 1	0.0003	0.0001	0.0001	0.0001
Gen Speed 2	0.0001	0.0001	0.0002	0.0001
Gen Angle 1	0.0513	0.0066	0.0059	0.0059
Gen Angle 2	0.0227	0.0066	0.0041	0.004
Voltage Mag 1	0.0431	0.0006	0.0004	0.0004
Voltage Mag 2	0.0394	0.0005	0.0004	0.0004
Voltage Mag 3	0.0895	0.0010	0.0007	0.0007
Voltage Mag 4	0.0635	0.0005	0.0005	0.0005
Voltage Mag 5	0.0038	0.0004	0.0004	0.0003
Voltage Mag 6	0.0481	0.0010	0.0013	0.0016
Voltage Angle 1	0.0218	0.0014	0.0008	0.0008
Voltage Angle 2	0.0207	0.0014	0.0007	0.0007
Voltage Angle 3	0.0527	0.0033	0.0011	0.0216
Voltage Angle 4	0.0206	0.0011	0.0011	0.0011
Voltage Angle 5	0.0211	0.0012	0.0015	0.0015
Voltage Angle 6	0.0049	0.0050	0.0066	0.0067

Table 29: IEEE 14-bus model island 1 Total RMSE for all internal states with measurement FDI

RMSE	UKF	Huber	S-UKF	MM-UKF
Gen Speed Err Tot	0.0002	0.0001	0.0001	0.0001
Gen Angle Err Tot	0.0370	0.0066	0.0050	0.0049
Voltage Err Tot	0.0288	0.0005	0.0004	0.0004
Angle Err Tot	0.0212	0.0013	0.0010	0.0010

Table 30: IEEE 14-bus model island 7 RMSE for all states with measurement FDI

RMSE	UKF	Huber-UKF	S-UKF	MM-UKF
Gen Speed 4	0.0002	0.0003	0.0003	0.0002
Gen Angle 4	0.0161	0.0098	0.0100	0.0101
Voltage Mag 1	0.0466	0.0014	0.0009	0.0011
Voltage Mag 2	0.0459	0.001	0.0009	0.0009
Voltage Mag 3	0.0896	0.0012	0.0009	0.001
Voltage Mag 4	0.0647	0.0025	0.0031	0.003
Voltage Mag 5	0.0228	0.0028	0.0032	0.0031
Voltage Mag 6	0.0466	0.0015	0.0013	0.0013
Voltage Mag 7	0.0946	0.0012	0.0007	0.0007
Voltage Mag 9	0.0660	0.0008	0.001	0.0009
Voltage Mag 10	0.0458	0.0006	0.0008	0.0009
Voltage Mag 11	0.0446	0.0006	0.0004	0.0004
Voltage Mag 12	0.0471	0.0010	0.0010	0.0010
Voltage Mag 13	0.0669	0.0010	0.0007	0.0007
Voltage Mag 14	0.0474	0.0010	0.0011	0.0011
Voltage Angle 1	0.0500	0.0054	0.0147	0.0041
Voltage Angle 2	0.0025	0.0025	0.0026	0.0029
Voltage Angle 3	0.0619	0.008	0.0223	0.0222
Voltage Angle 4	0.0279	0.0017	0.0026	0.0025
Voltage Angle 5	0.0329	0.0016	0.0024	0.0022
Voltage Angle 6	0.0126	0.0010	0.0011	0.0011
Voltage Angle 7	0.0010	0.0032	0.0016	0.0016
Voltage Angle 9	0.0146	0.0008	0.0019	0.0020
Voltage Angle 10	0.0125	0.0008	0.0011	0.0011
Voltage Angle 11	0.0131	0.0008	0.0006	0.0005
Voltage Angle 12	0.0497	0.0050	0.0043	0.0043
Voltage Angle 13	0.0479	0.0038	0.0010	0.0147
Voltage Angle 14	0.0143	0.0110	0.0147	0.0014

Table 31: IEEE 14-bus model island 7 Total RMSE for internal states with measurement FDI

RMSE	UKF	Huber	S-UKF	MM-UKF
Gen Speed Err Tot	0.0002	0.0003	0.0003	0.0002
Gen Angle Err Tot	0.0161	0.0098	0.01	0.0101
Voltage Err Tot	0.0484	0.0015	0.0016	0.0016
Angle Err Tot	0.0189	0.0011	0.0016	0.0016

Table 32: IEEE 14-bus model total RMSE for all islands with measurement FDI

RMSE	UKF	Huber	S-UKF	MM-UKF
Gen Speed Err Tot	0.0002	0.0003	0.0003	0.0002
Gen Angle Err Tot	0.0164	0.0097	0.0099	0.0099
Voltage Err Tot	0.0506	0.0008	0.0009	0.0010
Angle Err Tot	0.0211	0.0019	0.0021	0.0021

Table 33: IEEE 14-bus model average iteration time in islands 1 and 7

RMSE	UKF (s)	Huber-UKF (s)	S-UKF (s)	MM-UKF (s)
Island 1	0.00640	0.02290	0.03406	0.03998
Island 7	0.01727	0.02697	0.07313	0.07831

Figures 46 – 57 and Table 32 confirm the non-robustness of the UKF since its tracking is degraded and its RMSE is inflated in the presence of measurement FDI attacks. Furthermore, the attack instants can be identified due to red spikes in the UKF state estimates. Notably, the Huber-, S-, and MM-estimators reject all measurement FDI attacks. Row 13 in Table 30 designates the RMSE of the voltage magnitude of bus 3 and shows a degradation in the S-, MM- and Huber M-based UKF. This degradation is due to the estimated states being located externally to the considered island. The external bus estimations are degraded since no external power flow information outside of tie-lines is considered in the decentralized internal estimator.

6.3.1.2   <u>Decentralized Dynamic State Estimator under topology attacks or regressor outliers</u>

Due to the distributed nature of the decentralized state estimators, they no longer rely on the Kron reduced multi-machine Y_{bus}, as is the case for the centralized DSE. This change means that the original topology corruption attack needs to target the individual lines of the system, instead of the reduced Kron matrix. The topology attacks are generated in two steps:

1. Modify a selected line impedance

$$BD_{Line_{idx}}(i) = L_k(i) * C_k(i) \tag{6.6}$$

2. Rebuild Y_{bus} matrix for each island.

The scaling factor $C_k(I)$ is 0.01 to simulate a line opening. Additionally, $L_k(i)$ is a line in the span of the transmission line which is selected at random to be corrupted. k indicates the amount of pieces of FDI. The same simulation scenario is presented where the line between bus 5 and 6 is disconnected to induce a transient at t=2 seconds. The line between bus 1 and bus 5 is selected for the topology attack. The impact can be seen below in Figures 58 to 72.
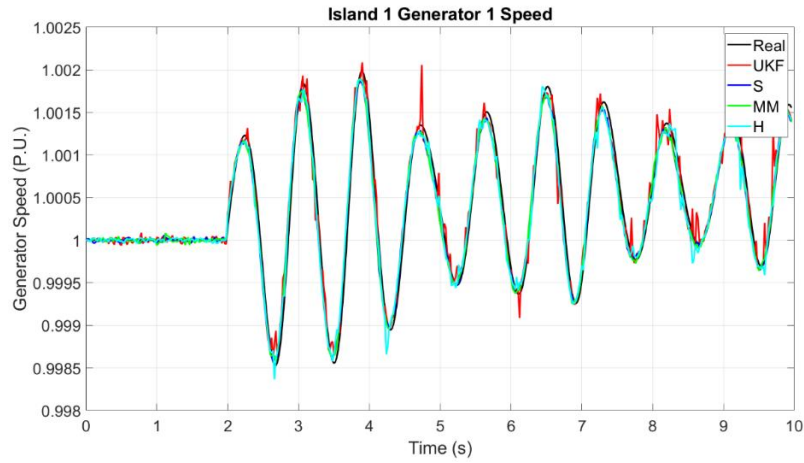
Figure 58: IEEE 14-bus model island 1 generator 1 speed estimation with topology FDI
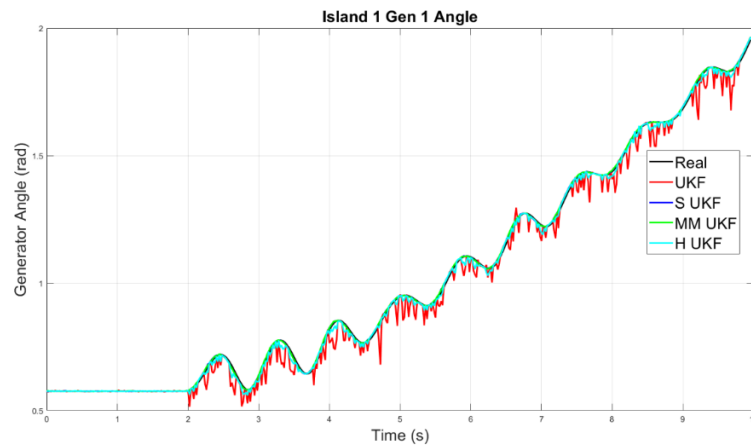
Figure 59: IEEE 14-bus model island 1 generator 1 angle estimation with topology FDI
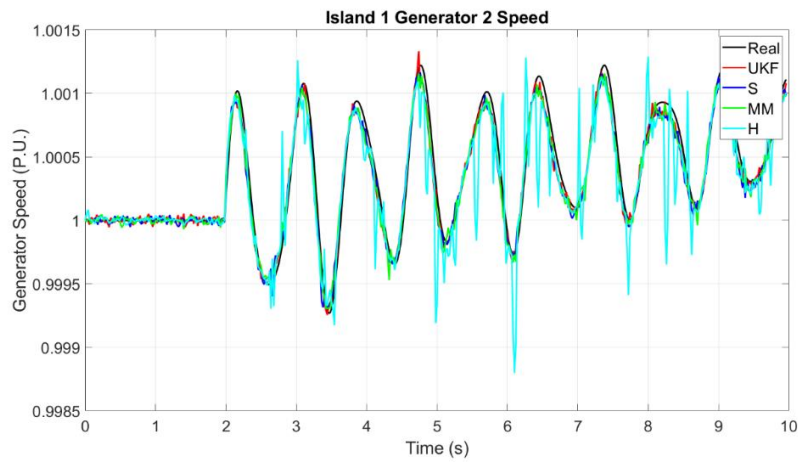
Figure 60: IEEE 14-bus model island 1 generator 2 speed estimation with topology FDI
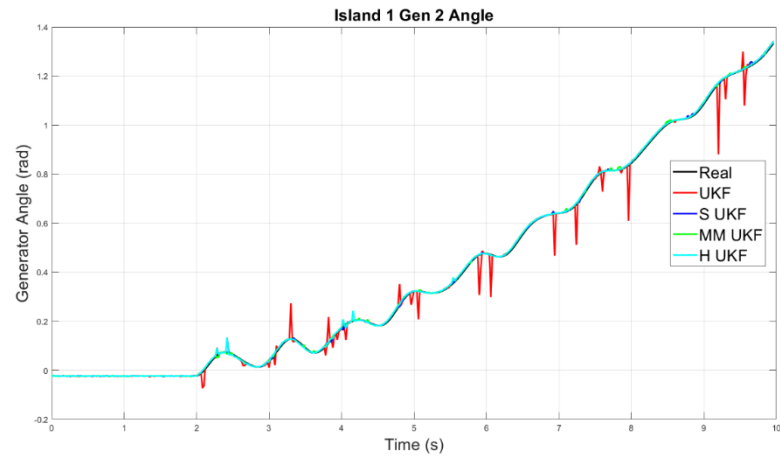
Figure 61: IEEE 14-bus model island 1 generator 2 angle estimation with topology FDI
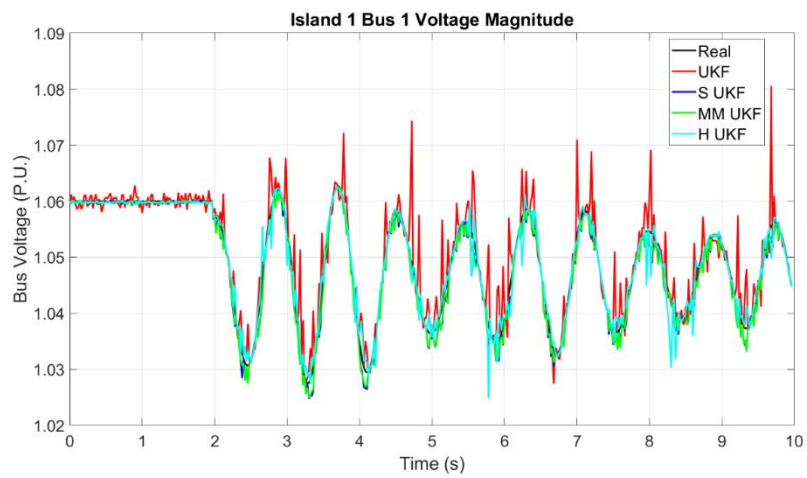
Figure 62: IEEE 14-bus model island 1 bus 1 voltage estimation with topology FDI
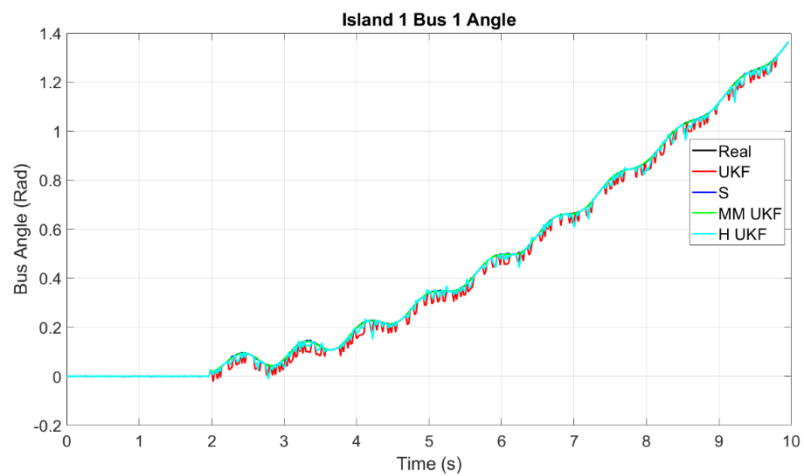
Figure 63: IEEE 14-bus model island 1 bus 1 angle estimation with topology FDI
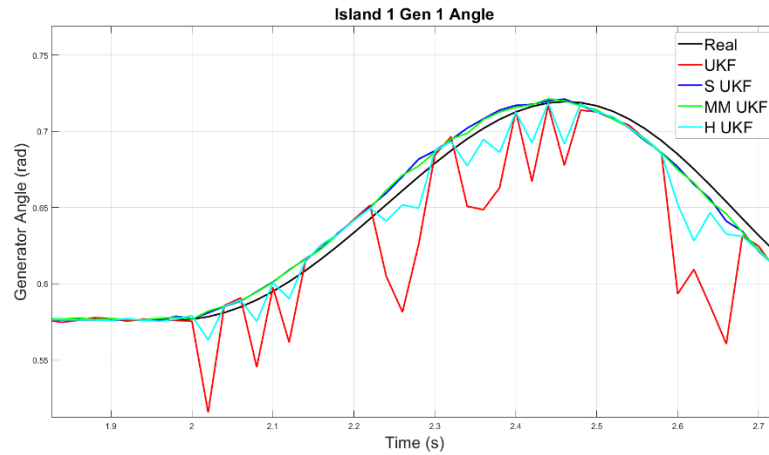
Figure 64: IEEE 14-bus model island 1 bus 1 angle estimation with topology FDI zoomed
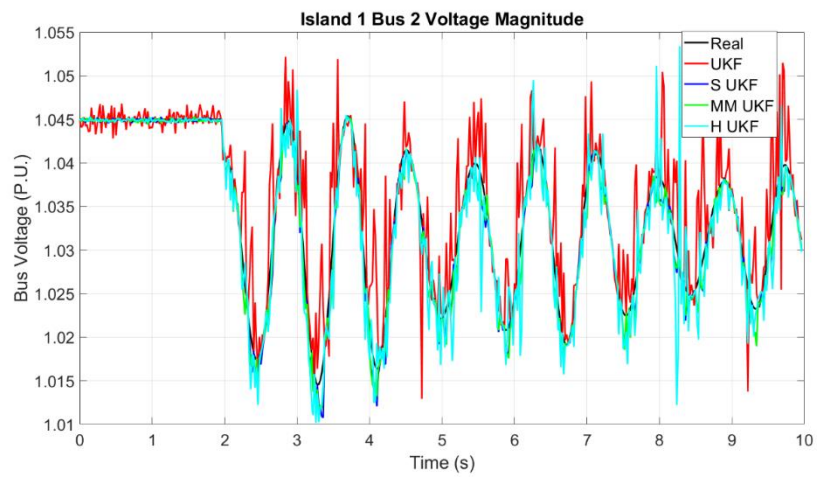
Figure 65: IEEE 14-bus model island 1 bus 2 voltage estimation with topology FDI
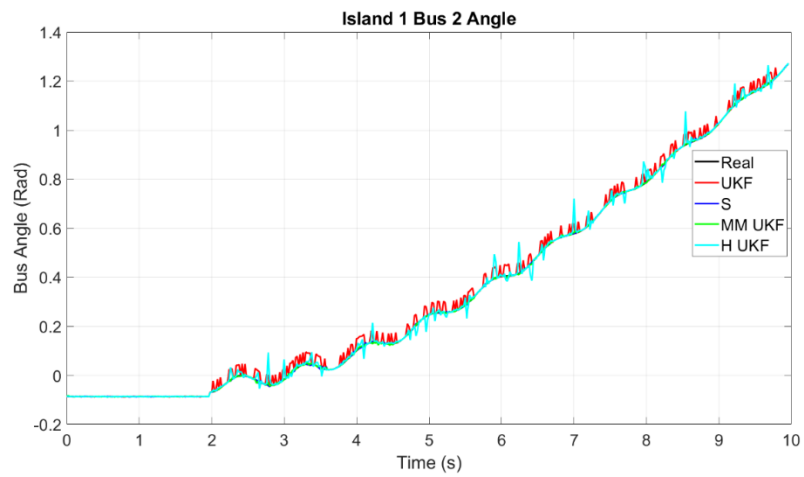
Figure 66: IEEE 14-bus model island 1 bus 2 angle estimation with topology FDI
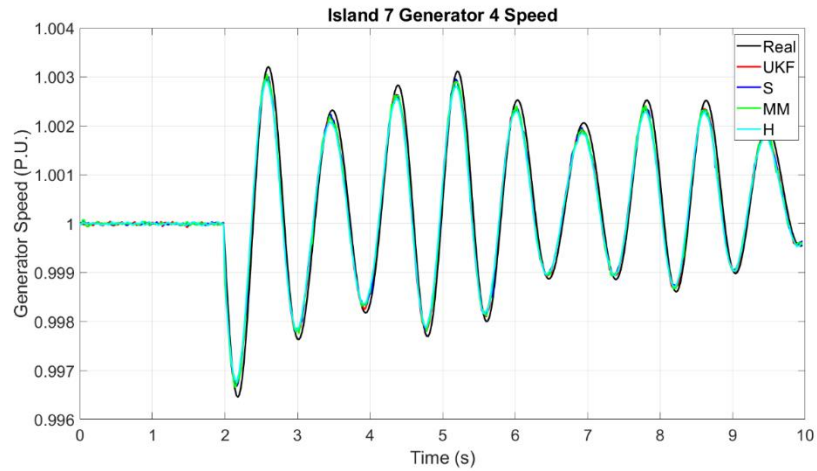
Figure 67: IEEE 14-bus model island 7 generator 4 speed estimation with topology FDI
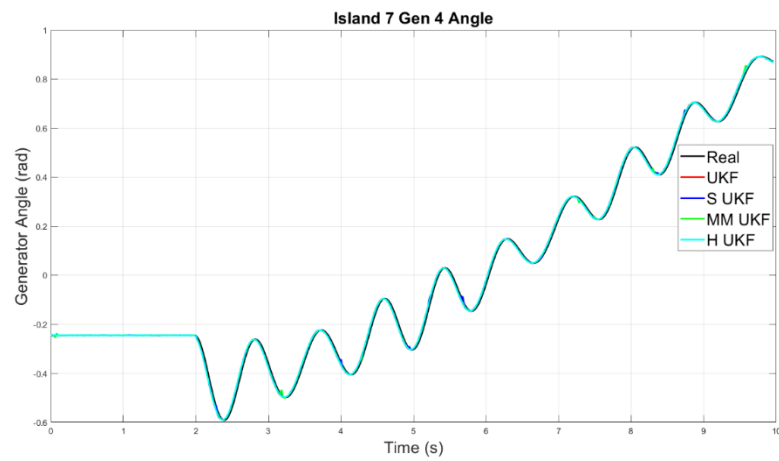
Figure 68: IEEE 14-bus model island 7 generator 4 angle estimation with topology FDI
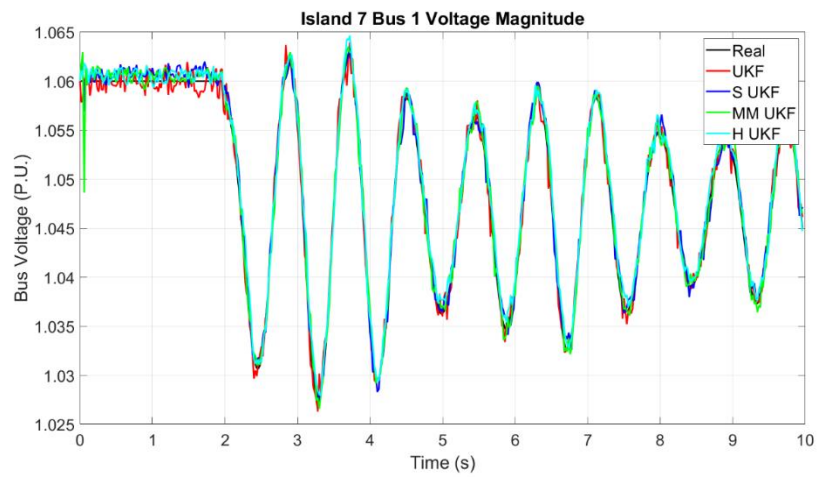
Figure 69: IEEE 14-bus model island 7 bus 1 voltage estimation with topology FDI
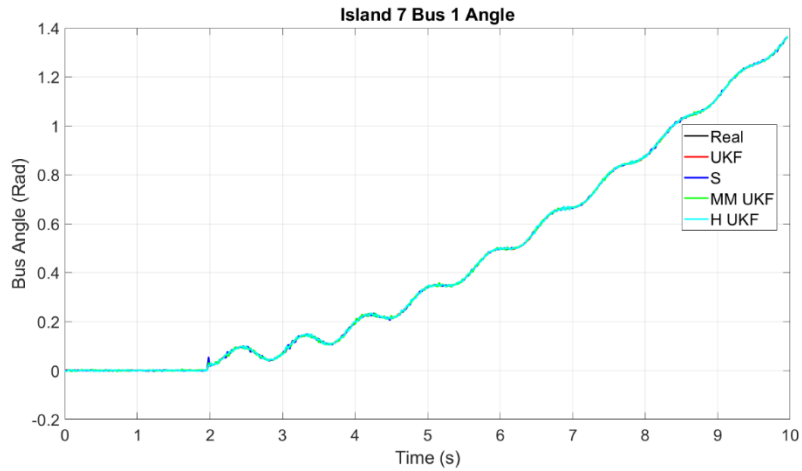
Figure 70: IEEE 14-bus model island 7 bus 1 angle estimation with topology FDI
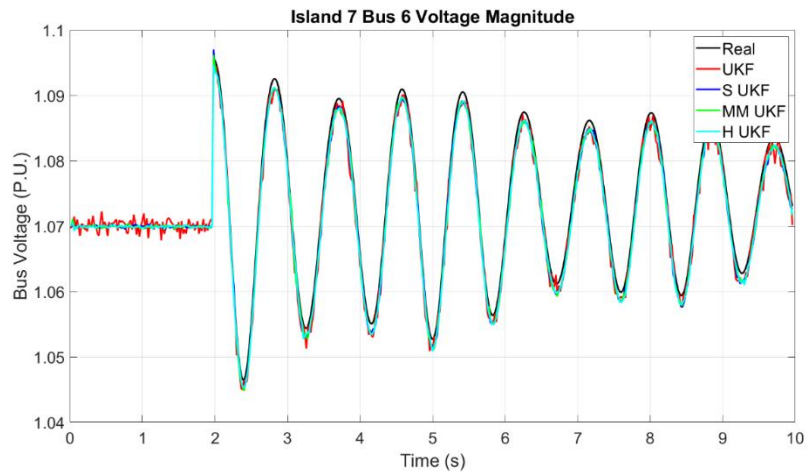
Figure 71: IEEE 14-bus model island 7 bus 6 voltage estimation with topology FDI
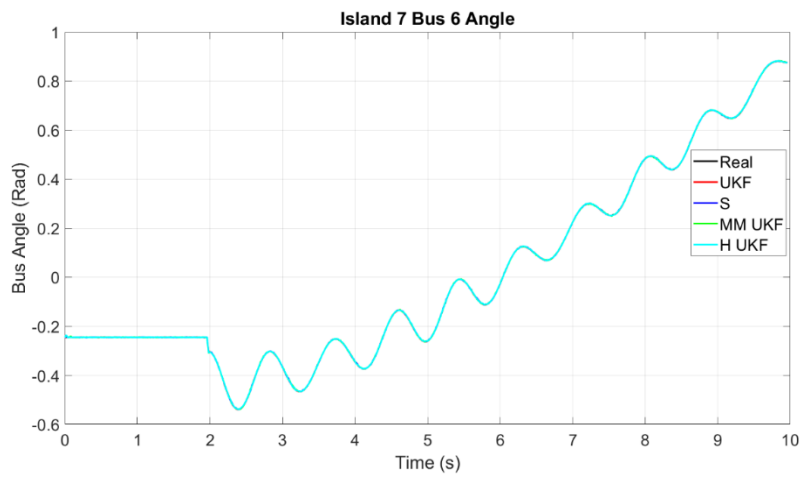
Figure 72: IEEE 14-bus model island 7 bus 6 angle estimation with topology FDI

Table 34: IEEE 14-bus model island 1 RMSE for all states with topology FDI

RMSE	UKF	Huber-UKF	S-UKF	MM-UKF
Gen Speed 1	0.0002	0.0002	0.0001	0.0001
Gen Speed 2	0.0001	0.0002	0.0001	0.0001
Gen Angle 1	0.0357	0.0123	0.0059	0.0059
Gen Angle 2	0.0253	0.0133	0.0044	0.0044
Voltage Mag 1	0.0045	0.0018	0.0015	0.0015
Voltage Mag 2	0.0049	0.0025	0.0017	0.0017
Voltage Mag 3	0.001	0.0224	0.0007	0.0007
Voltage Mag 4	0.001	0.0024	0.0007	0.0007
Voltage Mag 5	0.0038	0.0019	0.0004	0.0004
Voltage Mag 6	0.001	0.0019	0.0031	0.0015
Voltage Angle 1	0.0225	0.0151	0.0020	0.0015
Voltage Angle 2	0.0248	0.0203	0.0026	0.0022
Voltage Angle 3	0.0065	0.0194	0.0026	0.0026
Voltage Angle 4	0.0017	0.0078	0.0022	0.0021
Voltage Angle 5	0.0045	0.0056	0.0015	0.0022
Voltage Angle 6	0.0010	0.0125	0.0031	0.0031

Table 35: IEEE 14-bus model island 1 Total RMSE for all internal states with topology FDI

RMSE	UKF	Huber-UKF	S-UKF	MM-UKF
Gen Speed Total	0.0001	0.0002	0.0001	0.0001
Gen Angle Total	0.0305	0.0128	0.0052	0.0052
Voltage Total	0.0044	0.002	0.0012	0.0012
Angle Total	0.0173	0.0137	0.0021	0.0020

Table 36: IEEE 14-bus model island 7 RMSE for all states with topology FDI

RMSE	UKF	Huber-UKF	S-UKF	MM-UKF
Gen Speed 4	0.0002	0.0003	0.0002	0.0002
Gen Angle 4	0.01	0.0095	0.0098	0.01
Voltage Mag 1	0.001	0.001	0.001	0.001
Voltage Mag 2	0.001	0.001	0.0009	0.0009
Voltage Mag 3	0.001	0.0008	0.0008	0.0008
Voltage Mag 4	0.0028	0.0032	0.003	0.003
Voltage Mag 5	0.0031	0.0033	0.0032	0.0031
Voltage Mag 6	0.0016	0.0013	0.0013	0.0013
Voltage Mag 7	0.001	0.0006	0.0007	0.0007
Voltage Mag 9	0.0013	0.0009	0.0009	0.0009
Voltage Mag 10	0.0012	0.0008	0.0008	0.0008
Voltage Mag 11	0.0009	0.0004	0.0004	0.0004
Voltage Mag 12	0.001	0.0007	0.0009	0.001
Voltage Mag 13	0.001	0.0005	0.0007	0.0007
Voltage Mag 14	0.001	0.001	0.0011	0.001
Voltage Angle 1	0.001	0.0032	0.0035	0.0034
Voltage Angle 2	0.001	0.0025	0.0027	0.0028
Voltage Angle 3	0.001	0.0025	0.0026	0.0025
Voltage Angle 4	0.0008	0.0015	0.0016	0.0016
Voltage Angle 5	0.0009	0.0014	0.0015	0.0014
Voltage Angle 6	0.0006	0.0011	0.001	0.0012
Voltage Angle 7	0.001	0.0015	0.0016	0.0016
Voltage Angle 9	0.0005	0.0017	0.0018	0.0017
Voltage Angle 10	0.0005	0.0008	0.0009	0.0009
Voltage Angle 11	0.0004	0.0004	0.0004	0.0005
Voltage Angle 12	0.0009	0.004	0.0043	0.0041
Voltage Angle 13	0.0009	0.0008	0.0008	0.0009
Voltage Angle 14	0.001	0.0013	0.0013	0.0013

Table 37: IEEE 14-bus model island 7 Total RMSE for all internal states with topology FDI

RMSE	UKF	Huber-UKF	S-UKF	MM-UKF
Gen Speed Total	0.0002	0.0003	0.0002	0.0002
Gen Angle Total	0.0099	0.0095	0.0099	0.0098
Voltage Total	0.001	0.0006	0.0009	0.001
Angle Total	0.0018	0.0020	0.0020	0.0020

Table 38: IEEE 14-bus model total RMSE for all islands with topology FDI

RMSE	UKF	Huber-UKF	S-UKF	MM-UKF
Gen Speed Total	0.0002	0.0002	0.0002	0.0002
Gen Angle Total	0.0153	0.0092	0.0071	0.0071
Voltage Total	0.0023	0.0012	0.001	0.0009
Angle Total	0.0060	0.0041	0.0026	0.0027

Table 39: IEEE 14-bus model island 1 and 7 average iteration time with topology FDI

	UKF (s)	Huber-UKF (s)	S-UKF (s)	MM- UKF(s)
Island 1	0.007231	0.02721	0.03565	0.03895
Island 7	0.01727	0.02863	0.07166	0.07484

With the topology attacks originating in island 1, the results confirm that due to the islanding scheme, the impact of the attacks is limited to island 1estimation. This is due to the network connection of the two islands where the generated topology attack did not impact any of the internal lines in island 7. Figures 67-72 show that island 7 tracking is not impacted by the topology attacks and the whole system RMSE does not show this limited impact. Figure 64 depicts a zoomed-in stream of data of Figure 63. The figures shows the impact of the topology attacks on the Huber M-based UKF. The impact of attacks is limited in this scenario. This effect is diluted in the RMSE calculations. Table 35 shows the related RMSE for island 1 where the topology attack is located. Table 38 confirms the increased RMSE for the UKF and Huber M-based UKF. The Figures and Tables confirm that the S- and MM-based UKF are resistant to the topology attacks when tracking the dynamic states.

6.3.2 *Decentralized Dynamic State Estimator Applied to the IEEE 118-bus test case*

In this section, the dynamic state estimators are applied to track the states of the larger IEEE 118-bus system. The IEEE 118-bus system is decomposed into islands for the estimation as proposed in [121]. The different islands are displayed in Table 40 on the next page, where there are 65 islands ranging from 2 buses to 10 buses. Those islands were found using a graph theory approach to maximize the number of attacks or outliers detected, as proposed in [121]. A transient is generated by opening the same previous line between bus 38 and 65 at t=2s. We show the obtained dynamic estimation on the clean measurement data scenario, measurement with FDI attacks, and perceived topology corrupted by FDI. Two islands are chosen to illustrate the obtained results in the simulation results.

Table 40:Island decomposition for the IEEE 118-bus model

Island Number	Internal Bus Designation	Island Number	Internal Bus Designation
1	110,112	34	15,17,18,19
2	110,111	35	17,31,32,113
3	86,87	36	24,70,71,72
4	71,73	37	27,32,114,115
5	68,116	38	3,5,11,12
6	12,117	39	34,35,36,37
7	9,10	40	45,46,48,49
8	85,86	41	75,76,77,118
9	8,9	42	77,78,79,80
10	100,103,104	43	77,80,82,96
11	103,104,105	44	80,98,99,100
12	105,106,107	45	89,90,91,92
13	37,39,40	46	92,100,101,102
14	4,5,11	47	103,105,108,109,110
15	40,41,42	48	11,12,13,14,15
16	47,49,69	49	12,14,15,16,17
17	54,55,56	50	27,28,29,31,32
18	54,55,59	51	49,51,52,53,54
19	54,56,59	52	49,50,54,56,57
20	59,60,61	53	49,51,54,56,58
21	60,61,62	54	49,69,65,66,68
22	62,66,67	55	5,6,7,11,12
23	69,70,75	56	68,69,77,80,81
24	69,75,77	57	61,62,64,65,66,67
25	70,74,75	58	17,18,19,30,34,37,38
26	80,96,97	59	5,8,11,13,15,17,30
27	83,84,85	60	15,17,18,19,30,33,37,38
28	85,88,89	61	34,37,40,42,43,44,45,49
29	92,94,100	62	49,54,59,61,62,63,64,66
30	92,93,94	63	17,18,19,20,21,22,23,31,32
31	94,95,96	64	82,83,85,89,92,93,94,95,96
32	1,2,3,12	65	17,18,19,20,21,22,23,25,26,30
33	100,104,105,106		

6.3.2.1   Decentralized Dynamic State Estimator under clean data

Figures 73-80 depict the decentralized dynamic state estimation results for islands 11 and 65. The chosen islands represent a small island of three internal buses and the largest island with ten buses. Due to limited space, only a couple islands will be shown visually below. The tracking results and computation times are shown for these two islands.
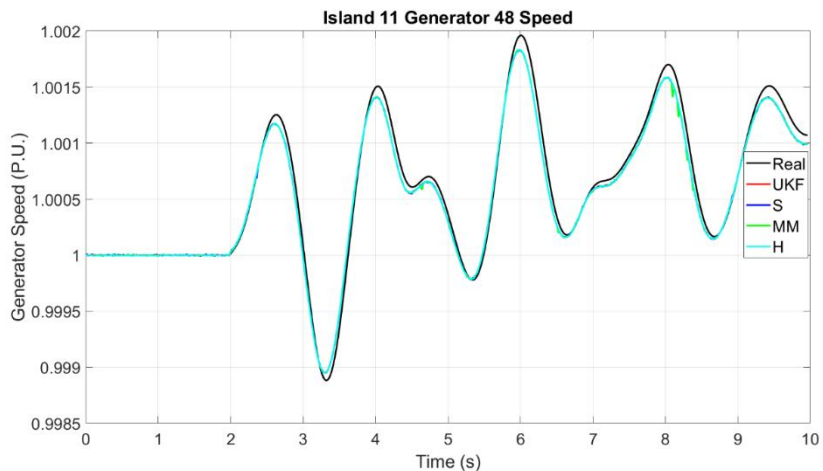
Figure 73: IEEE 118-bus model island 11 generator 48 speed estimation for with clean data
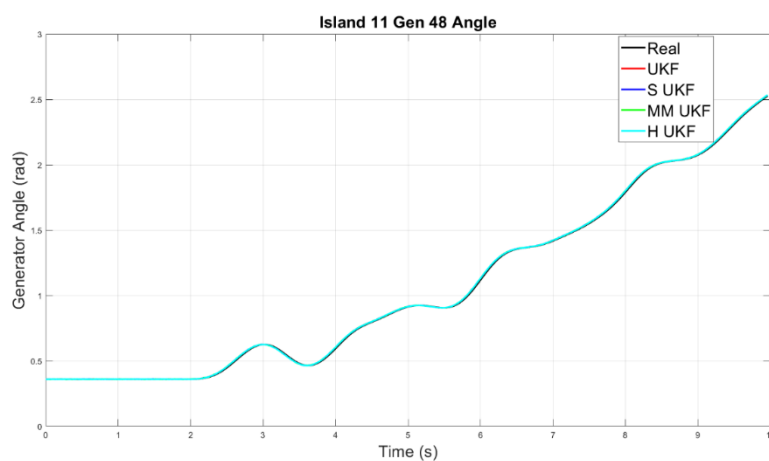
Figure 74: IEEE 118-bus model island 11 generator 48 angle estimation with clean data
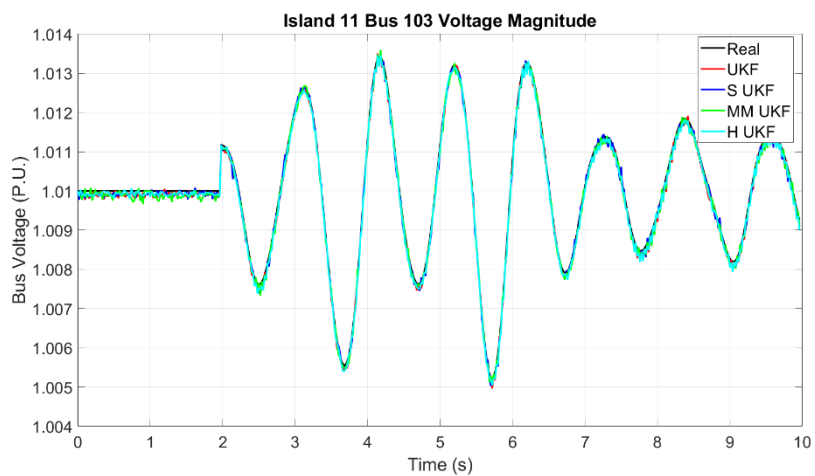
Figure 75: IEEE 118-bus model island 11 bus 103 voltage estimation with clean data
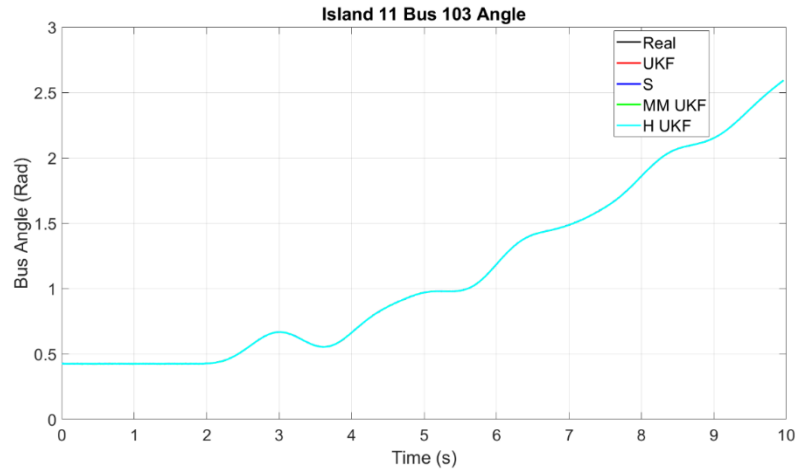
Figure 76: IEEE 118-bus model island 11 bus 103 angle magnitude estimation with clean data
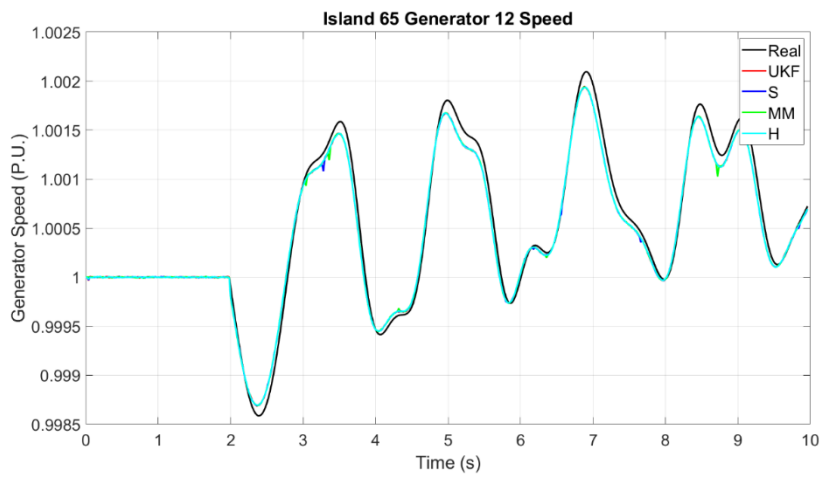
Figure 77: IEEE 118-bus model island 65 generator 12 speed estimation with clean data
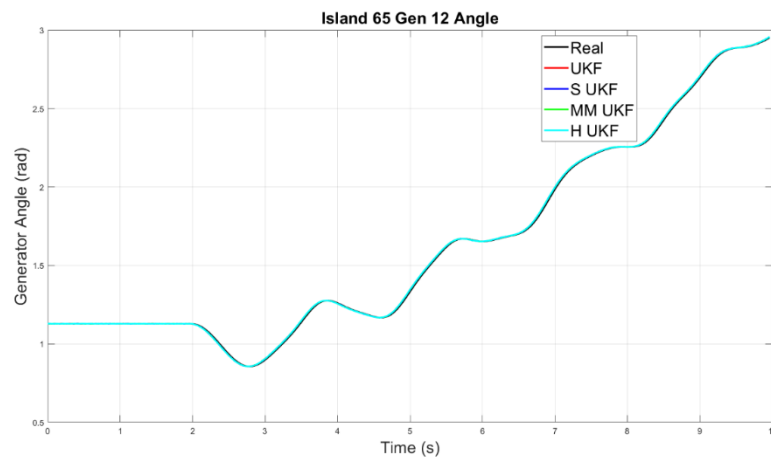
Figure 78: IEEE 118-bus model island 65 generator 12 angle estimation with clean data
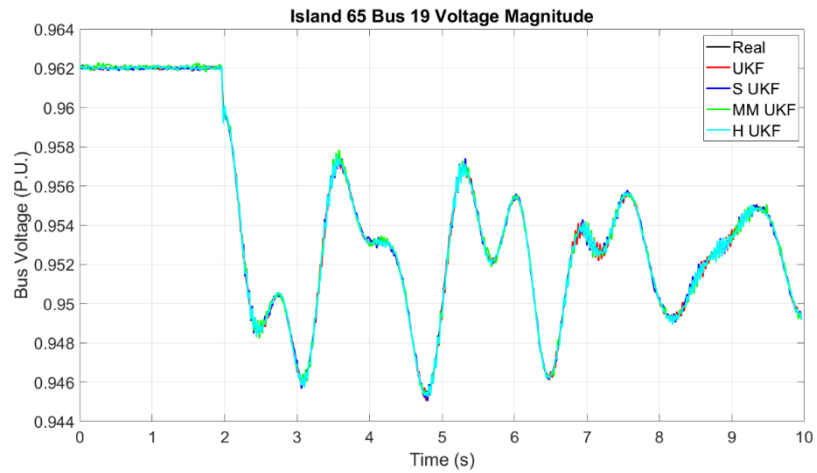
Figure 79: IEEE 118-bus model island 65 bus 19 voltage estimation with clean data
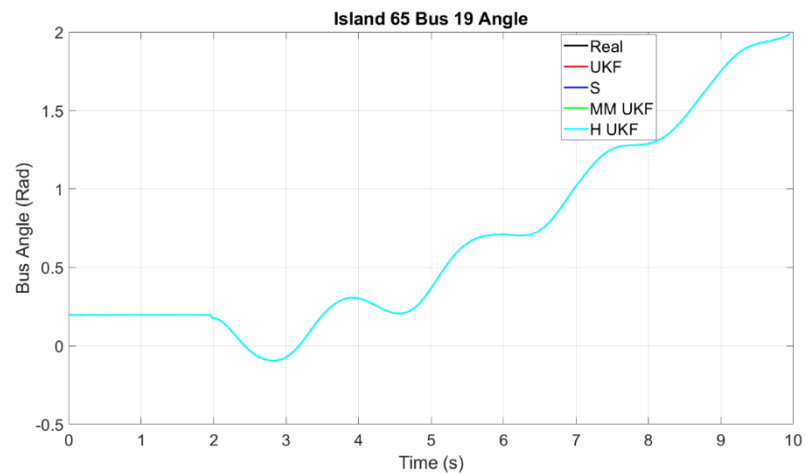
Figure 80: IEEE 118-bus model island 65 bus 19 voltage angle estimation with clean data

Table 41: IEEE 118-bus model island 11 RMSE for all states with clean data

RMSE	UKF	Huber-UKF	S-UKF	MM-UKF
Gen Speed 45	0.0001	0.0001	0.0001	0.0001
Gen Speed 46	0.0001	0.0001	0.0001	0.0001
Gen Speed 47	0.0001	0.0001	0.0002	0.0001
Gen Angle 45	0.0052	0.0052	0.0052	0.0052
Gen Angle 46	0.0054	0.0054	0.0055	0.0055
Gen Angle 47	0.0057	0.0057	0.0058	0.0058
Voltage Mag 92	0.0001	0.0001	0.0001	0.0001
Voltage Mag 94	0.0001	0.0001	0.0001	0.0001
Voltage Mag 98	0.0001	0.0001	0.0001	0.0001
Voltage Mag 99	0.0001	0.0001	0.0001	0.0001
Voltage Mag 100	0.0001	0.0001	0.0001	0.0001
Voltage Mag 101	0.0001	0.0001	0.0001	0.0001
Voltage Mag 103	0.0001	0.0001	0.0001	0.0001
Voltage Mag 104	0.0001	0.0001	0.0001	0.0001
Voltage Mag 105	0.0001	0.0001	0.0001	0.0001
Voltage Mag 106	0.0001	0.0001	0.0001	0.0001
Voltage Mag 110	0.0001	0.0001	0.0001	0.0001
Voltage Angle 92	0.0001	0.0001	0.0009	0.0004
Voltage Angle 94	0.0001	0.0001	0.0006	0.0005
Voltage Angle 98	0.0001	0.0001	0.0008	0.0006
Voltage Angle 99	0.0001	0.0001	0.0006	0.0006
Voltage Angle 100	0.0002	0.0002	0.0002	0.0002
Voltage Angle 101	0.0001	0.0001	0.0010	0.0010
Voltage Angle 103	0.0002	0.0002	0.0002	0.0002
Voltage Angle 104	0.0001	0.0001	0.0001	0.0001
Voltage Angle 105	0.0001	0.0001	0.0001	0.0001
Voltage Angle 106	0.0001	0.0001	0.0010	0.0003
Voltage Angle 110	0.0001	0.0001	0.0007	0.0005

Table 42: IEEE 118-bus model island 11 Total RMSE for all internal states with clean data

RMSE	UKF	Huber-UKF	S-UKF	MM-UKF
Gen Speed Tot	0.0001	0.0001	0.0002	0.0001
Gen Angle Tot	0.0057	0.0057	0.0059	0.0057
Voltage Tot	0.0001	0.0001	0.0001	0.0001
Angle Tot	0.0001	0.0001	0.0002	0.0002

Table 43: IEEE 118-bus model island 65 RMSE for all states with clean data

RMSE	UKF	Huber-UKF	S-UKF	MM-UKF
Gen Speed 8	0.0001	0.0001	0.0001	0.0001
Gen Speed 9	0.0001	0.0001	0.0001	0.0001
Gen Speed 11	0.0001	0.0001	0.0001	0.0001
Gen Speed 12	0.0001	0.0001	0.0001	0.0001
Gen Angle 8	0.0065	0.0065	0.0065	0.0065
Gen Angle 9	0.0066	0.0066	0.0066	0.0066
Gen Angle 11	0.0060	0.0060	0.0060	0.0060
Gen Angle 12	0.0062	0.0062	0.0062	0.0062
Voltage Mag 8	0.0001	0.0001	0.0001	0.0001
Voltage Mag 15	0.0001	0.0001	0.0001	0.0001
Voltage Mag 16	0.0001	0.0001	0.0001	0.0001
Voltage Mag 17	0.0001	0.0001	0.0001	0.0001
Voltage Mag 18	0.0001	0.0001	0.0001	0.0001
Voltage Mag 19	0.0001	0.0001	0.0001	0.0001
Voltage Mag 20	0.0001	0.0001	0.0001	0.0001
Voltage Mag 21	0.0001	0.0001	0.0001	0.0001
Voltage Mag 22	0.0001	0.0001	0.0001	0.0001
Voltage Mag 23	0.0001	0.0001	0.0001	0.0001
Voltage Mag 24	0.0001	0.0001	0.0001	0.0001
Voltage Mag 25	0.0001	0.0001	0.0001	0.0001
Voltage Mag 26	0.0001	0.0001	0.0001	0.0001
Voltage Mag 27	0.0001	0.0001	0.0001	0.0001
Voltage Mag 30	0.0001	0.0001	0.0001	0.0001
Voltage Mag 31	0.0001	0.0001	0.0001	0.0001
Voltage Mag 32	0.0001	0.0001	0.0001	0.0001
Voltage Mag 34	0.0001	0.0001	0.0001	0.0002
Voltage Mag 38	0.0001	0.0001	0.0001	0.0001
Voltage Mag 113	0.0001	0.0001	0.0001	0.0001
Voltage Angle 8	0.0001	0.0001	0.0001	0.0001
Voltage Angle 15	0.0001	0.0001	0.0001	0.0002
Voltage Angle 16	0.0001	0.0001	0.0020	0.0026
Voltage Angle 17	0.0001	0.0001	0.0001	0.0001
Voltage Angle 18	0.0001	0.0002	0.0001	0.0001
Voltage Angle 19	0.0002	0.0002	0.0002	0.0002
Voltage Angle 20	0.0002	0.0002	0.0002	0.0002
Voltage Angle 21	0.0002	0.0002	0.0002	0.0002
Voltage Angle 22	0.0002	0.0002	0.0002	0.0002
Voltage Angle 23	0.0002	0.0002	0.0002	0.0002
Voltage Angle 24	0.0001	0.0001	0.0001	0.0001
Voltage Angle 25	0.0002	0.0002	0.0002	0.0002
Voltage Angle 26	0.0001	0.0002	0.0002	0.0002
Voltage Angle 27	0.0001	0.0001	0.0004	0.0004
Voltage Angle 30	0.0001	0.0001	0.0001	0.0001
Voltage Angle 31	0.0001	0.0001	0.0014	0.0010
Voltage Angle 32	0.0001	0.0001	0.0001	0.0006
Voltage Angle 34	0.0001	0.0001	0.0003	0.0007
Voltage Angle 38	0.0001	0.0001	0.0008	0.0009
Voltage Angle 113	0.0001	0.0001	0.0006	0.0004

Table 44: IEEE 118-bus model island 65 Total RMSE for all internal states with clean data

RMSE	UKF	Huber-UKF	S-UKF	MM-UKF
Gen Speed Total	0.0001	0.0001	0.0001	0.0001
Gen Angle Total	0.0063	0.0063	0.0063	0.0063
Voltage Total	0.0001	0.0001	0.0001	0.0001
Angle Total	0.0001	0.0002	0.0002	0.0002

Table 45: IEEE 118-bus model Total RMSE for all internal states with clean data

RMSE	UKF	Huber-UKF	S-UKF	MM-UKF
Gen Speed Total	0.0001	0.0001	0.0001	0.0001
Gen Angle Total	0.0057	0.0057	0.0058	0.0058
Voltage Total	0.0001	0.0001	0.0001	0.0001
Angle Total	0.0002	0.0003	0.0004	0.0004

Table 46: IEEE 118-bus model mean iteration time with clean data

	UKF (s)	Huber-UKF (s)	S-UKF (s)	MM-UKF (s)
Island 1	0.009005	0.001999	0.05016	0.05523
Island 65	0.0275	0.05724	0.2057	0.1891

Tables 41 and 43 display the RMSE for all internal and external buses on islands 11 and 65. Tables 42 and 44 provide the mean of the internal buses RMSE of the two islands. Table 45 shows the RMSE of all the islands, and with inspection, all the estimators provide similar RMSE values. Table 46 provides the mean iteration times of the simulation.

6.3.2.2 Decentralized Dynamic State Estimator under Measurement False Data Injection Attacks

For analytics, the procedure to generate FDI attacks was the same as the IEEE 14-Bus model simulations. However, due to the increased size of the IEEE 118-bus model, the size of the FDI attack vector was increased to 200 in time to create a noticeable impact on the decentralized tracking. In Figures 81-90, the effect of the FDI attacks on the estimation is displayed. Island 11 was not impacted by many FDI attacks, and two buses are plotted for island 65, bus 17, and 19.
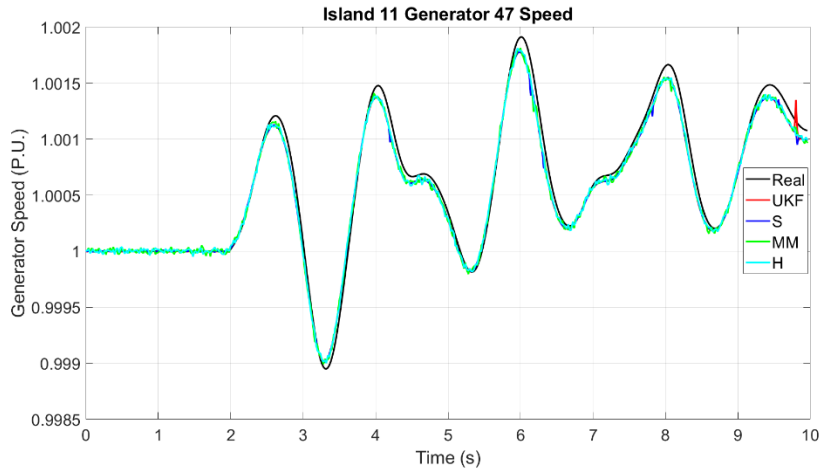
Figure 81: IEEE 118-bus model island 11 generator 47 speed estimation with measurement FDI
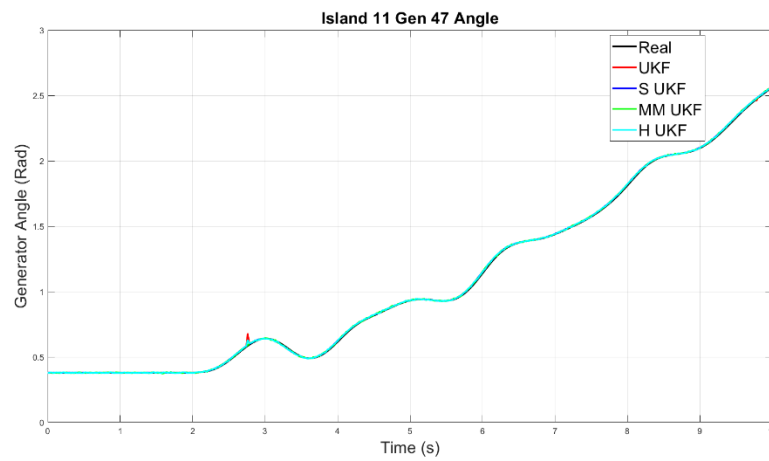
Figure 82: IEEE 118-bus model island 11 generator 47 angle estimation with measurement FDI
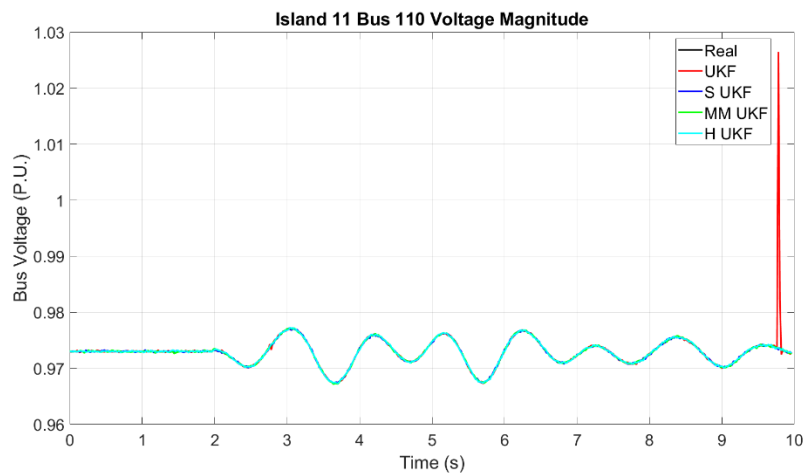
Figure 83: IEEE 118-bus model island 11 bus 100 voltage estimation with measurement FDI
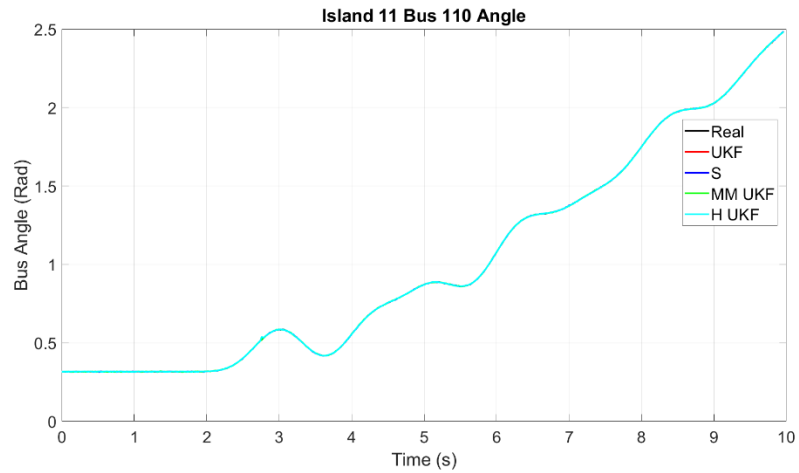
Figure 84: IEEE 118-bus model island 11 bus 110 angle estimation with measurement FDI
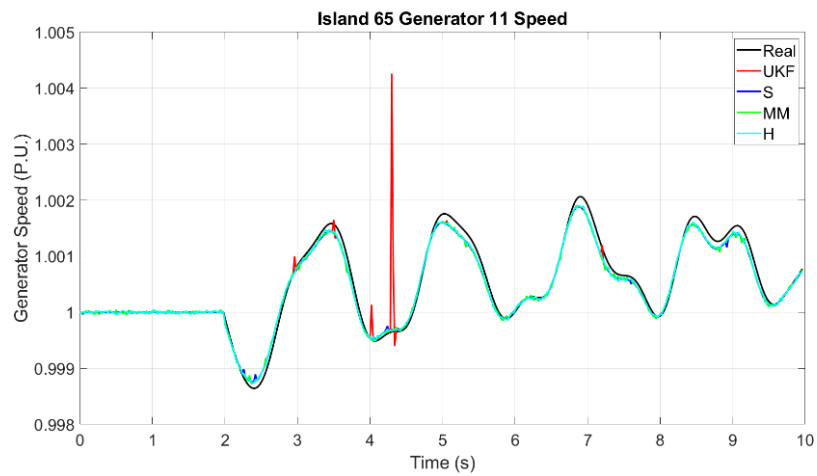
Figure 85: IEEE 118-bus model island 65 generator 11 speed estimation with measurement FDI
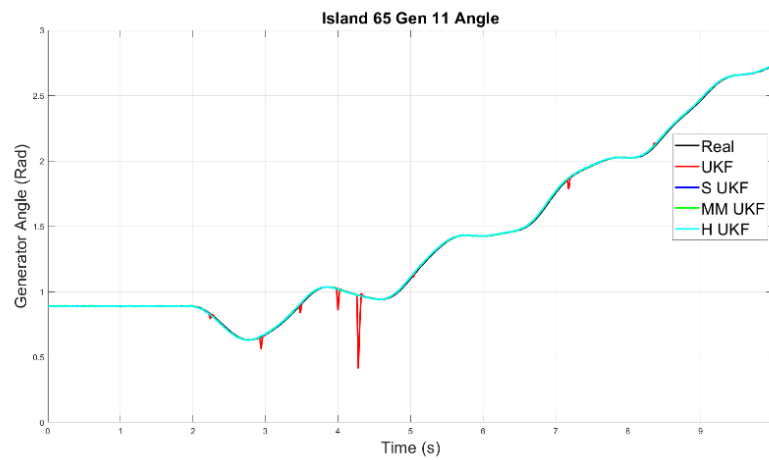
Figure 86: IEEE 118-bus model island 65 generator 11 angle estimation with measurement FDI
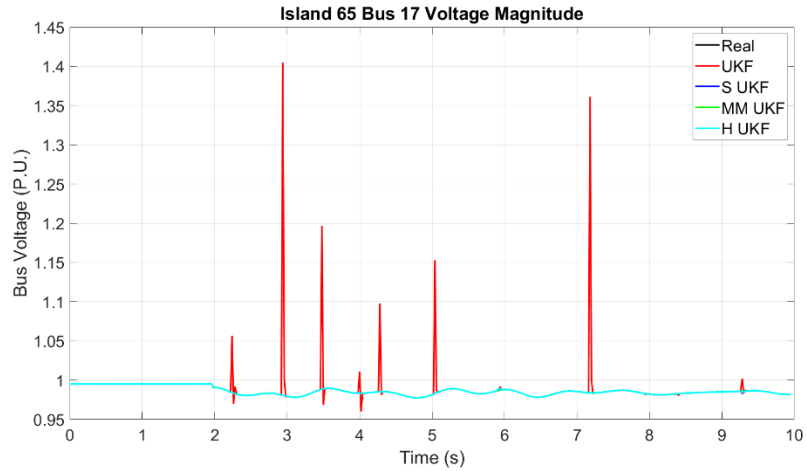
Figure 87: IEEE 118-bus model island 11 bus 107 voltage estimation with measurement FDI
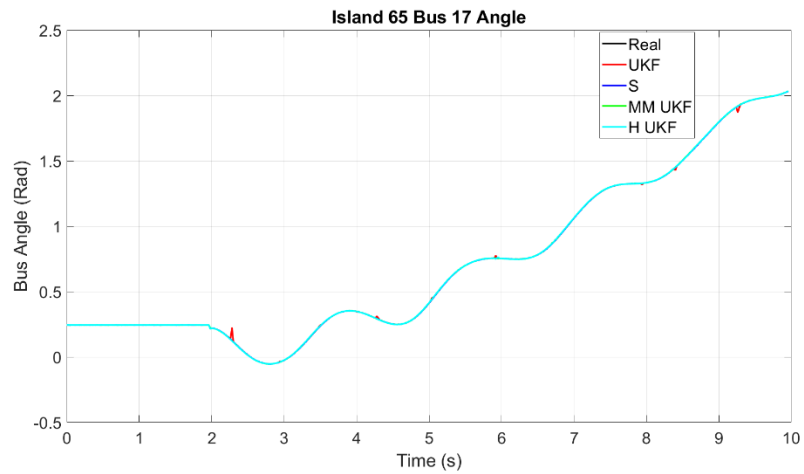
Figure 88: IEEE 118-bus model island 65 bus 17 angle estimation with measurement FDI
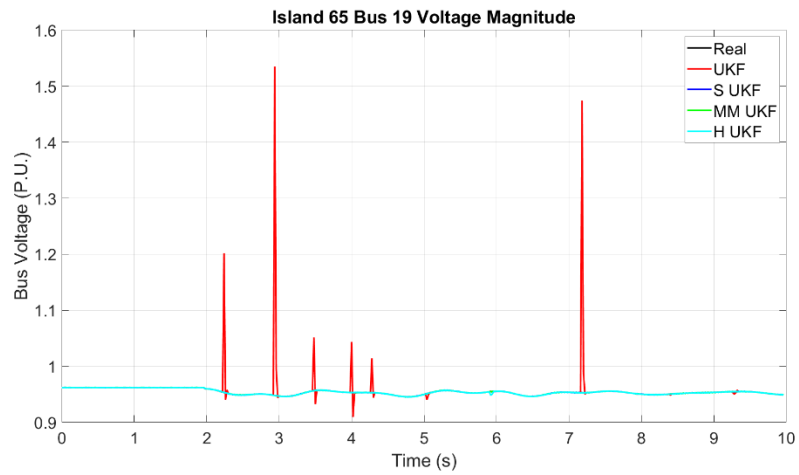
Figure 89: IEEE 118-bus model island 65 bus 19 voltage estimation with measurement FDI
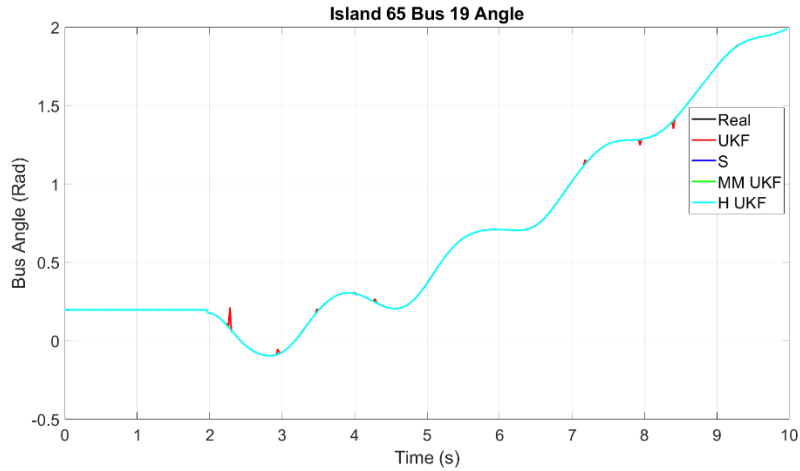
Figure 90: IEEE 118-bus model island 65 bus 19 angle estimation with measurement FDI

Table 47: IEEE 118-bus model island 11 RMSE for all states with measurement FDI

RMSE	UKF	Huber-UKF	S-UKF	MM-UKF
Gen Speed 46	0.0002	0.0001	0.0001	0.0002
Gen Speed 47	0.0001	0.0001	0.0001	0.0001
Gen Speed 48	0.0001	0.0001	0.0001	0.0001
Gen Angle 46	0.0145	0.0105	0.0053	0.051
Gen Angle 47	0.0081	0.0057	0.0057	0.0055
Gen Angle 48	0.0097	0.0061	0.0059	0.0059
Voltage Mag 100	0.1616	0.0001	0.0001	0.0001
Voltage Mag 103	0.0804	0.0002	0.0001	0.0002
Voltage Mag 104	0.0661	0.0003	0.0002	0.0003
Voltage Mag 105	0.0486	0.0001	0.0002	0.0001
Voltage Mag 106	0.0403	0.0003	0.0002	0.0003
Voltage Mag 107	0.0119	0.0002	0.0001	0.0001
Voltage Mag 108	0.0305	0.0003	0.0002	0.0003
Voltage Mag 110	0.0241	0.0001	0.0001	0.0001
Voltage Angle 100	0.0063	0.0016	0.0006	0.0016
Voltage Angle 103	0.0052	0.0013	0.0005	0.0013
Voltage Angle 104	0.0054	0.0005	0.0005	0.0006
Voltage Angle 105	0.0072	0.0004	0.0005	0.0005
Voltage Angle 106	0.0071	0.0011	0.0014	0.0013
Voltage Angle 107	0.0022	0.0011	0.0014	0.0012
Voltage Angle 108	0.0365	0.001	0.0012	0.0011
Voltage Angle 110	0.0062	0.0010	0.0010	0.0009

Table 48: IEEE 118-bus model island 65 RMSE for all states with measurement FDI

RMSE	UKF	Huber-UKF	S-UKF	MM-UKF
Gen Speed 8	0.0001	0.0001	0.0001	0.0001
Gen Speed 9	0.0001	0.0001	0.0001	0.0001
Gen Speed 11	0.0002	0.0001	0.0001	0.0001
Gen Speed 12	0.0003	0.0001	0.0001	0.0001
Gen Angle 8	0.0106	0.0067	0.0067	0.0065
Gen Angle 9	0.0095	0.0065	0.0065	0.0064
Gen Angle 12	0.0293	0.0057	0.0059	0.0058
Gen Angle 12	0.0381	0.0061	0.0062	0.0061
Voltage Mag 8	0.1129	0.0001	0.0001	0.0001
Voltage Mag 15	0.0373	0.0003	0.0003	0.0003
Voltage Mag 16	0.0044	0.0001	0.0001	0.0001
Voltage Mag 17	0.0289	0.0002	0.0002	0.0001
Voltage Mag 18	0.0441	0.0007	0.0004	0.0003
Voltage Mag 19	0.0376	0.0004	0.0002	0.0002
Voltage Mag 20	0.0475	0.0002	0.0001	0.0001
Voltage Mag 21	0.0546	0.0002	0.0001	0.0001
Voltage Mag 22	0.0758	0.0002	0.0001	0.0002
Voltage Mag 23	0.0248	0.0001	0.0001	0.0001
Voltage Mag 24	0.0176	0.0001	0.0001	0.0001
Voltage Mag 25	0.0325	0.0002	0.0002	0.0001
Voltage Mag 26	0.0301	0.0004	0.0002	0.0004
Voltage Mag 27	0.0187	0.0003	0.0002	0.0002
Voltage Mag 30	0.0298	0.0004	0.0002	0.0003
Voltage Mag 31	0.2142	0.0001	0.0001	0.0021
Voltage Mag 32	0.0074	0.0001	0.0001	0.0001
Voltage Mag 34	0.0038	0.0001	0.0001	0.0001
Voltage Mag 38	0.0356	0.0002	0.0001	0.0006
Voltage Mag1 13	0.0262	0.0004	0.0001	0.0002
Voltage Angle 8	0.0028	0.0015	0.0012	0.0014
Voltage Angle 15	0.0075	0.0015	0.0010	0.0016
Voltage Angle 16	0.0012	0.0015	0.0014	0.0017
Voltage Angle 17	0.0053	0.0015	0.0004	0.0014
Voltage Angle 18	0.0084	0.0005	0.0005	0.0005
Voltage Angle 19	0.0072	0.0006	0.0005	0.0006
Voltage Angle 20	0.0071	0.0005	0.0003	0.0005
Voltage Angle 21	0.0056	0.0004	0.0003	0.0004
Voltage Angle 22	0.0029	0.0004	0.0003	0.0004
Voltage Angle 23	0.003	0.0006	0.0005	0.0005
Voltage Angle 24	0.0023	0.0007	0.0011	0.0011
Voltage Angle 25	0.0079	0.0005	0.0004	0.0005
Voltage Angle 26	0.0093	0.0003	0.0004	0.0003
Voltage Angle 27	0.0038	0.0004	0.0015	0.0005
Voltage Angle 30	0.0035	0.0004	0.0003	0.0003
Voltage Angle 31	0.0649	0.0258	0.0013	0.0013
Voltage Angle 32	0.0012	0.0010	0.0010	0.0011
Voltage Angle 34	0.0009	0.0011	0.0013	0.0011
Voltage Angle 38	0.0054	0.0008	0.001	0.0009
Voltage Angle 113	0.0065	0.0045	0.0009	0.0009

Table 49: IEEE 118-bus model island 11 Total RMSE with measurement FDI

RMSE	UKF	Huber-UKF	S-UKF	MM-UKF
Gen Speed Total	0.0001	0.0001	0.0001	0.0001
Gen Angle Total	0.0108	0.0074	0.0056	0.0054
Voltage Total	0.065	0.0002	0.0002	0.0002
Angle Total	0.0059	0.0007	0.0005	0.0008

Table 50: IEEE 118-bus model island 65 Total RMSE with measurement FDI

RMSE	UKF	Huber-UKF	S-UKF	MM-UKF
Gen Speed Total	0.0002	0.0001	0.0001	0.0001
Gen Angle Total	0.0219	0.0062	0.0063	0.0062
Voltage Total	0.0406	0.0003	0.0002	0.0002
Angle Total	0.006	0.0006	0.0004	0.0006

Table 51: IEEE 118-bus model total RMSE for all internal states with measurement FDI

RMSE	UKF	Huber-UKF	S-UKF	MM-UKF
Gen Speed Total	0.0001	0.0001	0.0001	0.0001
Gen Angle Total	0.0108	0.0064	0.0064	0.0064
Voltage Total	0.0045	0.0004	0.0004	0.0003
Angle Total	0.0098	0.0011	0.001	0.001

Table 52: IEEE 118-bus model mean iteration time with measurement FDI

Time (s)	UKF	Huber-UKF (s)	S-UKF (s)	MM-UKF (s)
Island 10	0.01142	0.02392	0.05372	0.05748
Island 65	0.03036	0.0648	0.1893	0.2172

The above figures show that the robust filters can identify the bad data and reject it. The non-robust UKF is impacted by bad data and gives estimation spikes in Figures 81-90. Tables 47-51 confirm an inflated RMSE of the UKF compared to the robust estimators. However, Tables 47 and 48 show the detailed internal and external buses RMSE estimation in the islands. Tables 49 and 50 indicate the internal bus RMSE. Analyzing the internal buses is of more interest in this case. In Table 51, the total RMSE for all islands and internal buses is presented. The table results confirm that the robust estimators reject the FDI attacks on the measurements. Table 52 provides the mean iteration times, where the required computation time is similar to the clean data scenario.

6.3.2.3   Decentralized Dynamic State Estimator under Topology Attacks

Topology attacks are generated on the IEEE 118-bus system by modifying the Y_{bus} as applied to the IEEE14 bus system. Furthermore, the number of topology attacks has been increased. In this case, 20

lines are attacked at once, with 75 attacks created in time. This simulation differs from the IEEE 14-bus model in that the attacks are spread out over all lines to show the distributed state estimation robustness.
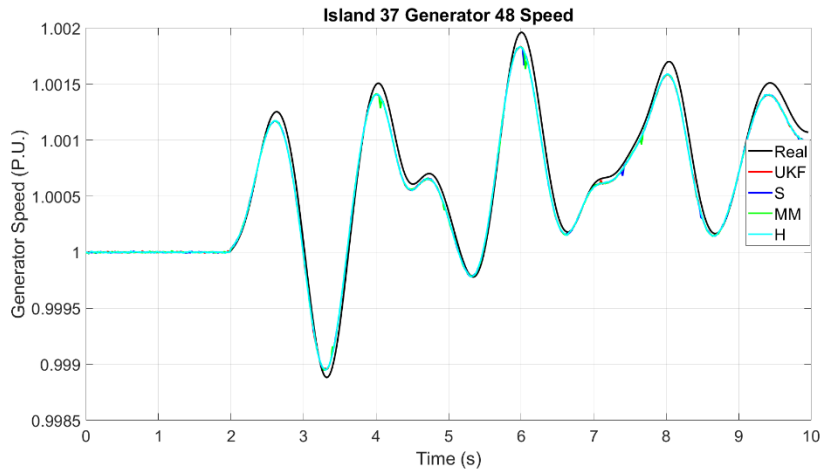
Figure 91: IEEE 118-bus model island 37 generator 47 speed estimation with topology FDI
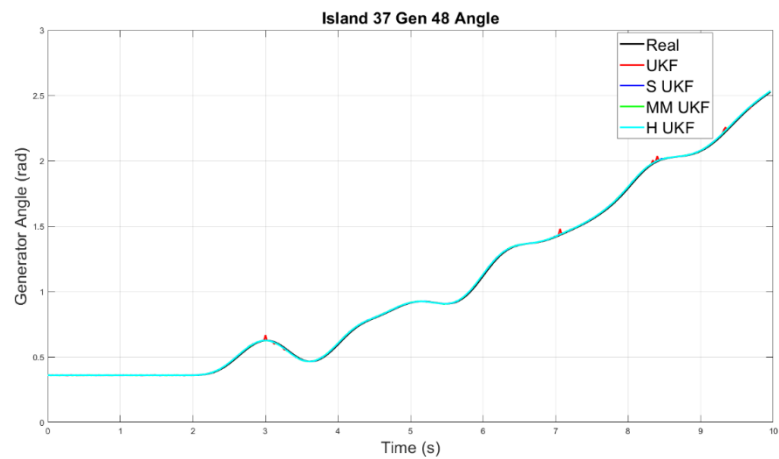
Figure 92: IEEE 118-bus model island 37 generator 47 speed estimation with topology FDI
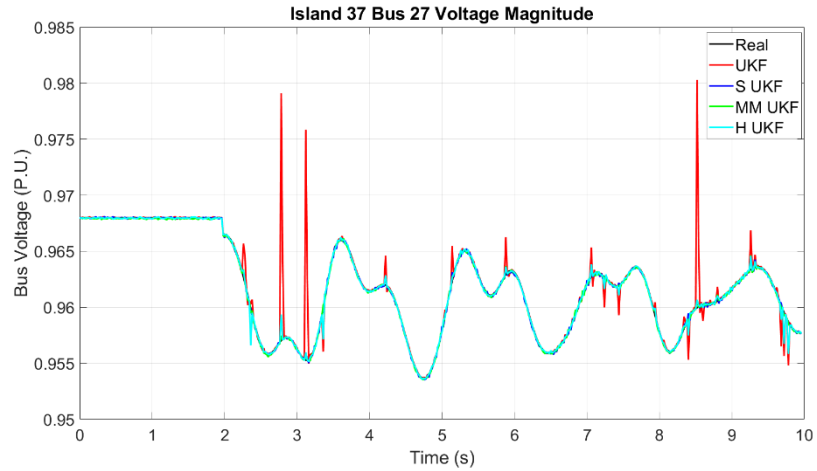
Figure 93: IEEE 118-bus model island 37 bus 27 voltage estimation with topology FDI
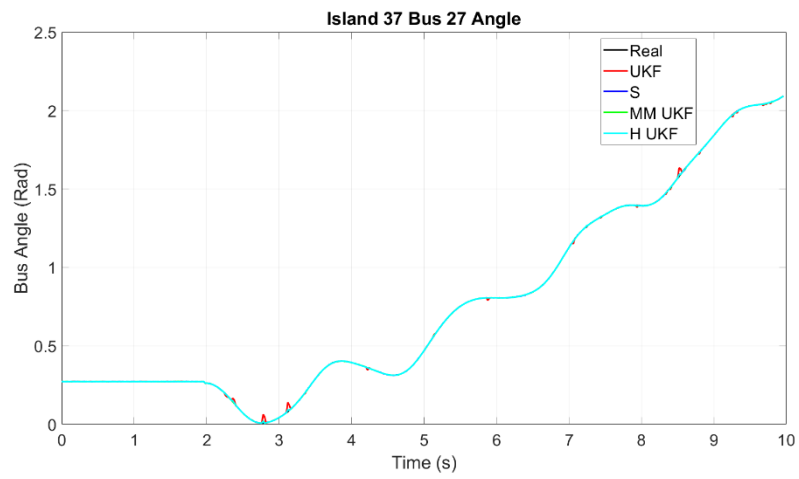
Figure 94: IEEE 118-bus model island 37 bus 27 voltage angle estimation with topology FDI
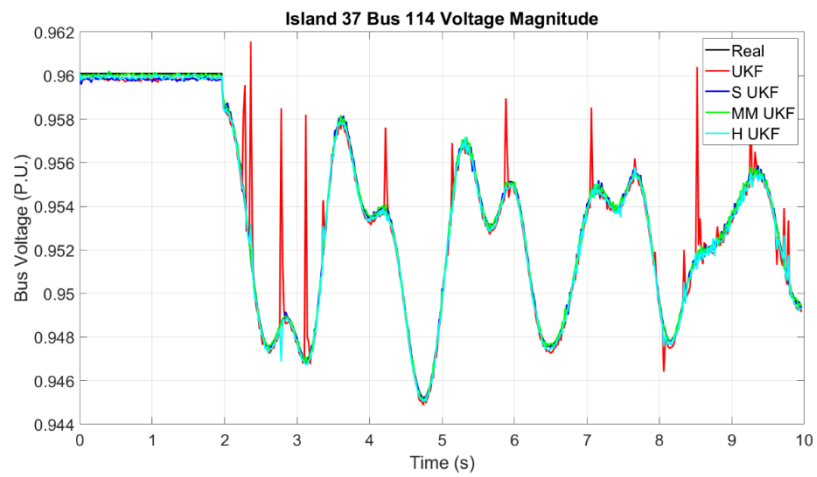
Figure 95: IEEE 118-bus model island 37 bus 114 voltage estimation with topology FDI
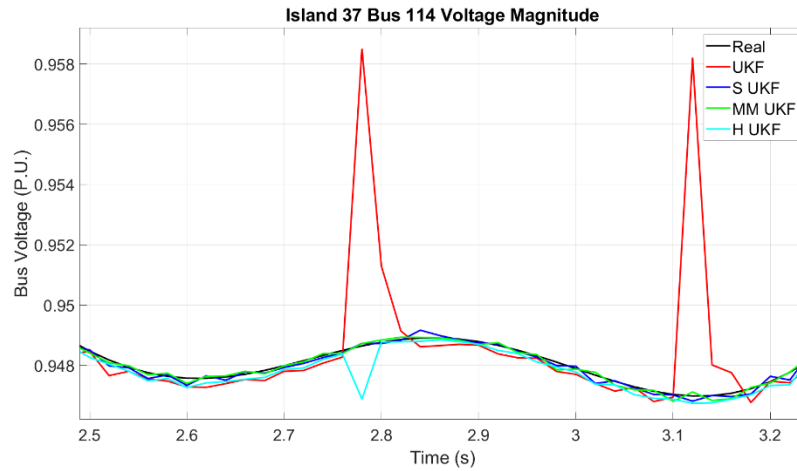
Figure 96: IEEE 118-bus model island 37 bus 114 voltage estimation with topo. FDI zoomed
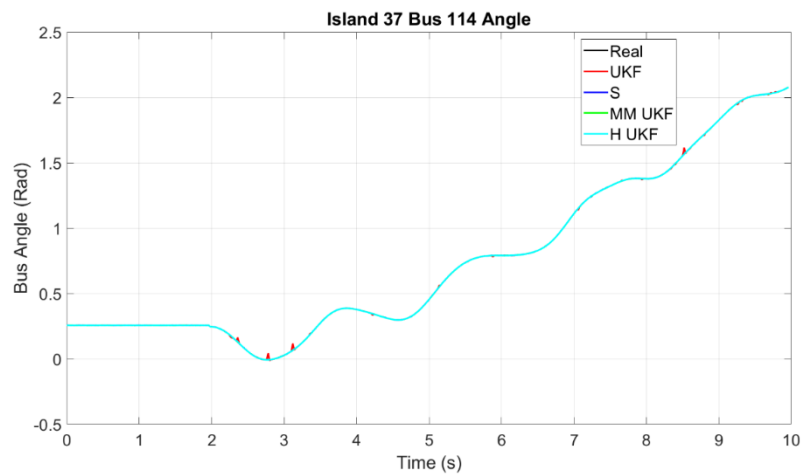
Figure 97: IEEE 118-bus model island 37 bus 114 angle estimation with topology FDI
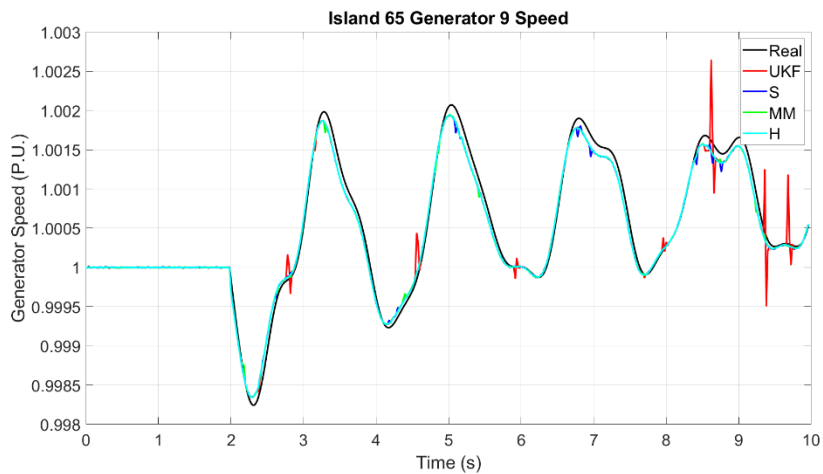
Figure 98: IEEE 118-bus model island 65 generator 47 speed estimation with topology FDI
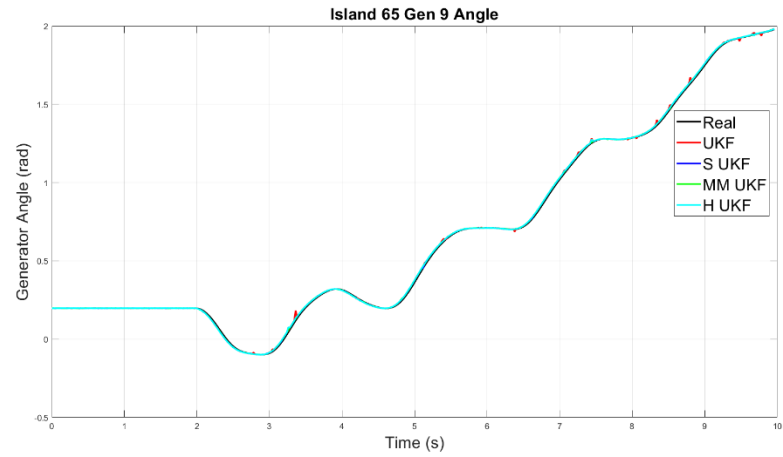
Figure 99: IEEE 118-bus model island 65 generator 47 speed estimation with topology FDI
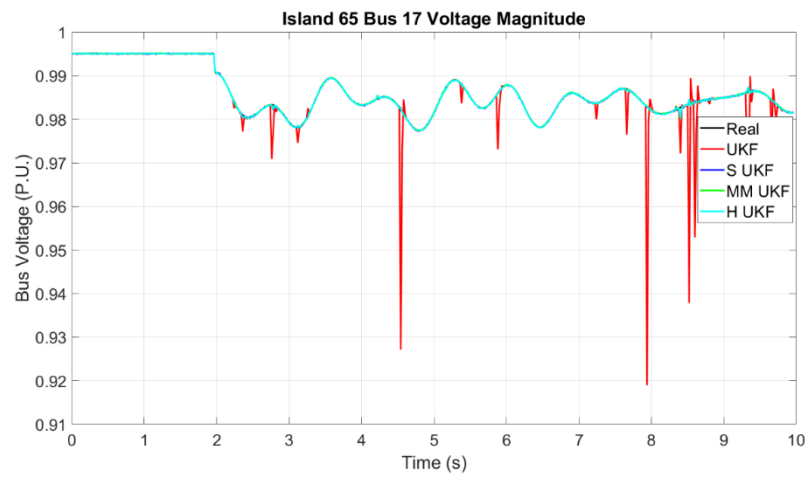
Figure 100: IEEE 118-bus model island 65 bus 17 voltage estimation with topology FDI
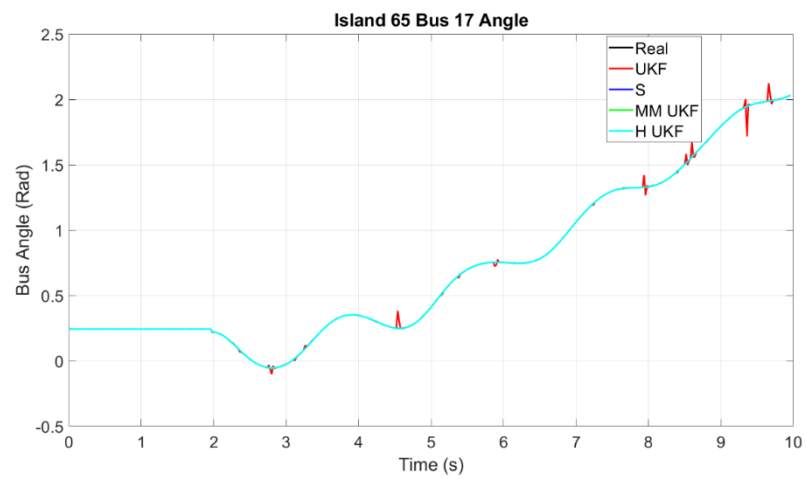
Figure 101: IEEE 118-bus model island 65 bus 17 voltage angle estimation with topology FDI
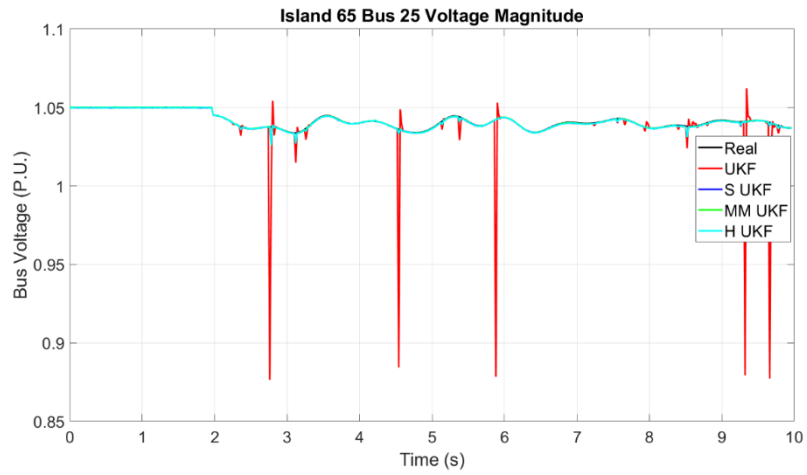
Figure 102: IEEE 118-bus model island 65 bus 25 voltage estimation with topology FDI
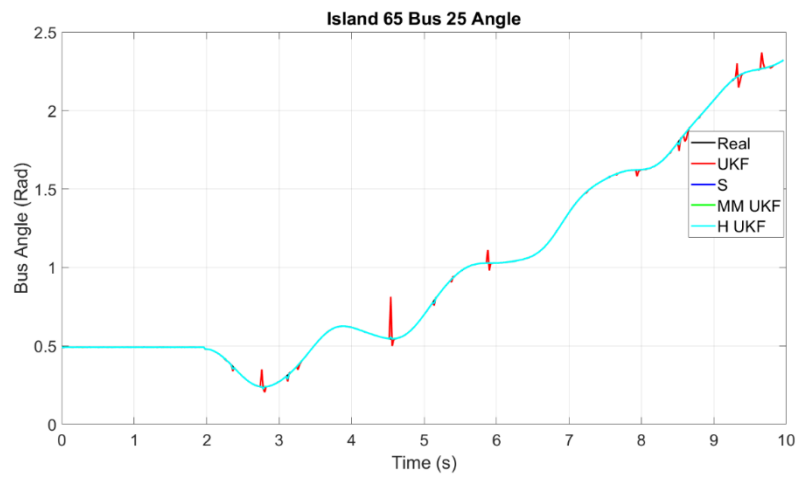
Figure 103: IEEE 118-bus model island 65 bus 25 voltage angle estimation with topology FDI

Table 53: IEEE 118-bus model island 37 RMSE for all states with topology FDI

RMSE	UKF	Huber-UKF	S-UKF	MM-UKF
Gen Speed 13	0.0001	0.0001	0.0001	0.0001
Gen Speed 15	0.0001	0.0001	0.0001	0.0001
Gen Angle 13	0.0081	0.0066	0.0065	0.0066
Gen Angle 15	0.0081	0.0066	0.0066	0.0066
Voltage Mag 23	0.0011	0.0001	0.0001	0.0001
Voltage Mag 25	0.0039	0.0001	0.0001	0.0001
Voltage Mag 27	0.0018	0.0003	0.0002	0.0002
Voltage Mag 28	0.0009	0.0002	0.0001	0.0001
Voltage Mag 31	0.0007	0.0001	0.0001	0.0001
Voltage Mag 32	0.0012	0.0003	0.0003	0.0003
Voltage Mag 113	0.0013	0.0001	0.0001	0.0001
Voltage Mag 114	0.0011	0.0003	0.0002	0.0001
Voltage Mag 115	0.0010	0.0002	0.0002	0.0001
Voltage Angle 23	0.0088	0.0021	0.0015	0.0014
Voltage Angle 25	0.0086	0.0016	0.0014	0.0011
Voltage Angle 27	0.0058	0.0011	0.0011	0.0011
Voltage Angle 28	0.0184	0.0013	0.001	0.0008
Voltage Angle 31	0.0063	0.0012	0.0011	0.0010
Voltage Angle 32	0.0055	0.0009	0.0009	0.0009
Voltage Angle 113	0.0037	0.0012	0.001	0.0011
Voltage Angle 114	0.0045	0.0005	0.0004	0.0004
Voltage Angle 115	0.0045	0.0005	0.0004	0.0004

Table 54: IEEE 118-bus model island 65 RMSE for all states with topology FDI

RMSE	UKF	Huber-UKF	S-UKF	MM-UKF
Gen Speed 8	0.0001	0.0001	0.0001	0.0001
Gen Speed 9	0.0001	0.0001	0.0001	0.0001
Gen Speed 11	0.0002	0.0001	0.0001	0.0001
Gen Speed 12	0.0001	0.0001	0.0001	0.0001
Gen Angle 8	0.0084	0.0064	0.0064	0.0064
Gen Angle 9	0.0088	0.0065	0.0065	0.0065
Gen Angle 11	0.0174	0.0059	0.0059	0.0059
Gen Angle 12	0.0196	0.0062	0.0062	0.0062
Voltage Mag 8	0.0128	0.0001	0.0001	0.0001
Voltage Mag 15	0.0099	0.0003	0.0002	0.0003
Voltage Mag 16	0.0028	0.0001	0.0001	0.0001
Voltage Mag 17	0.0049	0.0002	0.0002	0.0002
Voltage Mag 18	0.0044	0.0003	0.0003	0.0003
Voltage Mag 19	0.0048	0.0005	0.0004	0.0004
Voltage Mag 20	0.0029	0.0005	0.0005	0.0005
Voltage Mag 21	0.0033	0.0005	0.0006	0.0006
Voltage Mag 22	0.0056	0.0009	0.0008	0.0007
Voltage Mag 23	0.0136	0.0009	0.0009	0.0009
Voltage Mag 24	0.0139	0.0002	0.0001	0.0001
Voltage Mag 25	0.0163	0.0008	0.0008	0.0008
Voltage Mag 26	0.0153	0.0006	0.0006	0.0006
Voltage Mag 27	0.0176	0.0002	0.0002	0.0006
Voltage Mag 30	0.0054	0.0002	0.0002	0.0002
Voltage Mag 31	0.0071	0.0001	0.0001	0.0001
Voltage Mag 32	0.005	0.0002	0.0001	0.0001
Voltage Mag 34	0.0012	0.0004	0.0001	0.0001
Voltage Mag 38	0.0124	0.0002	0.0001	0.0002
Voltage Mag 113	0.0172	0.0002	0.0002	0.0002
Voltage Angle 8	0.0798	0.0016	0.0019	0.0014
Voltage Angle 15	0.0315	0.0014	0.0011	0.0012
Voltage Angle 16	0.017	0.0015	0.0015	0.0015
Voltage Angle 17	0.0166	0.0006	0.0005	0.0006
Voltage Angle 18	0.0144	0.0006	0.0007	0.0006
Voltage Angle 19	0.018	0.0008	0.0008	0.0008
Voltage Angle 20	0.0134	0.0015	0.0012	0.0012
Voltage Angle 21	0.0139	0.0019	0.0015	0.0014
Voltage Angle 22	0.0165	0.0026	0.0023	0.0018
Voltage Angle 23	0.0175	0.0026	0.0026	0.0025
Voltage Angle 24	0.0601	0.0017	0.0017	0.0018
Voltage Angle 25	0.0167	0.0021	0.0022	0.0021
Voltage Angle 26	0.0105	0.0015	0.0016	0.0015
Voltage Angle 27	0.0244	0.0006	0.0006	0.0006
Voltage Angle 30	0.0069	0.0004	0.0003	0.0003
Voltage Angle 31	0.0177	0.0013	0.0015	0.0014
Voltage Angle 32	0.0699	0.0016	0.0010	0.0010
Voltage Angle 34	0.0544	0.0012	0.0013	0.0051
Voltage Angle 38	0.0741	0.0008	0.0009	0.0009
Voltage Angle 113	0.0296	0.0007	0.0009	0.0008

Table 55: IEEE-118 bus model Island 37 RMSE for internal states with topology FDI

RMSE	UKF	Huber-UKF	S-UKF	MM-UKF
Gen Speed Total	0.0001	0.0001	0.0001	0.0001
Gen Angle Total	0.0081	0.0066	0.0066	0.0066
Voltage Total	0.0013	0.0003	0.0002	0.0002
Angle Total	0.0082	0.0015	0.0014	0.0013

Table 56: IEEE 118-bus model island 65 RMSE for internal states with topology FDI

RMSE	UKF	Huber- UKF	S- UKF	MM- UKF
Gen Speed Total	0.0001	0.0001	0.0001	0.0001
Gen Angle Total	0.0135	0.0063	0.0063	0.0063
Voltage Total	0.0076	0.0005	0.0005	0.0005
Angle Total	0.0145	0.0015	0.0014	0.0013

Table 57: IEEE 118-bus model total RMSE with topology FDI for all Islands

RMSE	UKF	Huber-UKF	S-UKF	MM-UKF
Gen Speed Total	0.0001	0.0001	0.0001	0.0001
Gen Angle Total	0.0108	0.0064	0.0064	0.0064
Voltage Total	0.0045	0.0004	0.0004	0.0003
Angle Total	0.0098	0.0011	0.0010	0.0010

Table 58: IEEE 118-bus model mean iteration time with topology FDI

	UKF	Huber-UKF (s)	S-UKF (s)	MM-UKF (s)
Island 37	0.01142	0.02392	0.05372	0.05748
Island 65	0.03036	0.0648	0.1893	0.2172

In Tables 53-57, the RMSE results for the different distributed dynamic state estimators presented is presented. Tables 53 and 54 provide the RMSE for all related states of the islands. The internal buses and their related RMSE are presented in Tables 55 and 56. Table 57 displays the mean of all RMSE values across all islands. The mean of the iteration time (i.e., one prediction and correction) for each dynamic estimator is presented in Table 58. The Huber M-based UKF computation time has increased computation time due to falsely identifying data as outliers. In Figures 91-103, it can be noted that the topology attacks impact the UKF. Similar to the decentralized DSE applied to the IEEE 14-bus system, Figure 97 indicates a similar trend to where the Huber M- based UKF and the UKF are impacted by topology attacks. Depending on the magnitude of the attack, the effect might not be clearly reflected in the RMSE values. In this, it's important to note that the metric of the RMSE shows the impact of the

FDI attacks when the magnitude is large enough. It may be concluded that the S- and MM-based UKF estimators provide resiliency against topology attacks for this simulation scenario from the figures.

6.3.3   *Simulation Discussion*

In this chapter, the results obtained may be split into two steps. The centralized DSE was first implemented to track dynamic states of simulated IEEE systems during a transient. To test the centralized test system, the various cases were tested. Firstly, a clean data case was tested to determine a base case for each estimator. Next, a measurement attack was commenced to corrupt the received measurements. Lastly, the topology of the system was attacked to fully test the abilities of the estimators. After the centralized cases were evaluated the decentralized DSEs were evaluated for the same cases.

Table 59: IEEE 118-Bus model mean iteration time for simulations conducted with clean data

Mean Iteration Time	UKF (s)	Huber-UKF (s)	S-UKF (s)	MM-UKF (s)
Centralized IEEE 118-bus model	0.0276	1.5935	1.6777	1.6288
Decentralized IEEE 118-bus model Island 1	0.009005	0.001999	0.05016	0.05523
Decentralized IEEE 118-bus model Island 65	0.0275	0.05724	0.2057	0.1891

The benefit of islanding becomes apparent for the robust estimators from Table 59. The traditional UKF has roughly the same estimation speed for the largest selected island in the system. However, robust estimators can significantly reduce their estimation computation time by reducing the tracked states achieved by the decentralized approach. The process is to execute the DSEs on the islands in parallel. Notice that these obtained times still do not fit with a DSE completed at the PMU reporting rates of 50 samples per second. These times could be decreased further by reducing the random samples in the S- and MM-, parallelizing estimators, and decomposing the system to minimize computation time instead of maximizing the breakdown point as considered in this thesis. This will be investigated in the future.

Figures 32 and 33 show that the centralized UKF and centralized Huber M-based UKF diverged when tracking under FDI attacks. With the application of the islanding, Figures 63 and 64 indicate the UKF and Hubers M-based UKF's ability to converge to a value after the attack. However, the decentralized UKF and Huber M-based UKF are still impacted by topology attacks, as denoted in Figure 64. This supports the need for high-breakdown point robust estimators, i.e., the S- and MM- estimators. In both the centralized and decentralized methods, they provide resiliency to measurement and topology attacks.

Chapter 7   Summary, and Future Work

This dissertation proposes highly robust static distribution state estimation and PMU-based robust distributed dynamic state estimation applied to transmission systems. A high breakdown robust regression S-estimator and Modified M, an a MM-estimator proposed in robust statistics theory, have been implemented and adapted to offer robustness for power systems monitoring. Simulation results illustrate the applications and the performance of these robust estimators in the presence of errors and false data injection (FDI) attacks.

The first application implemented robust estimators to a polyphase distribution system. The proposed robust state estimation module has integrated the cross-coupling modeling for unbalanced distribution systems. The two robust estimators are applied to a modified IEEE 13-bus model with different scenarios of measurements redundancy to provide realistic conditions for distribution systems. Furthermore, previously proposed estimators in the literature, such as the weighted least squares (WLS) with a bad data module (BDD) and the Huber M-estimator, have been implemented. The benefit of the considered robust S-estimator and MM-estimator is that they offer robustness to measurement and topology attacks, which is not the case for the M-estimator and the WLS with BDD. The latter estimators can resist only measurement attacks but are vulnerable to topology attacks. This enhanced resiliency obtained with the proposed estimators protected the energy trading application, which relies on the system's state. The calculated distribution locational marginal pricing (DLMP) is immune to the adverse effects of cyberattacks targeting both topology and measurements through the use of proposed robust estimators.

The second objective of this thesis is to enable robust dynamic state estimation for large wide-area monitoring systems using phasor measurement units (PMUs). The approach involves implementing the S-based and MM-based Unscented Kalman filter (UKF) over several islands. The correction step of the UKF algorithm is reformulated as a batch-mode regression, and the two high breakdown point robust estimators offered the robustness of the whole filter.

Simulations on the centralized multi-machine IEEE 14-bus and 57-bus systems show that the proposed robust S-based and MM-based UKF offer superior performance compared with the classical UKF, the Huber M-based UKF. This is especially true when attacks target the topology. Three scenarios are considered: clean PMU data and correct topology model, false data injection (FDI) in measurements, and topology FDI. The computation time of the estimators is given to evaluate of scaling of the estimators to large power systems. To enable the scaling of these estimators, we have decided to

implement a decentralized or distributed, decentralized robust DSE to allow filtering and tracking of large-systems states.

To decentralize the estimators from the traditional centralized estimation technique, the power system was decomposed into smaller islands. These small islands were designated by internal and external buses connected via tie-lines to create a dynamic mathematical model which relates the internal buses to generators allowing the islands' states to be estimated independently. This was achieved by deriving a relationship between the change of the power outputs of the generators and the voltage magnitude and angle of each bus to create dynamic and algebraic states. Simulations were conducted to evaluate the performance of the distributed robust S-based and MM-based UKF over multiple IEEE test cases. Firstly, the IEEE 14-bus system is decomposed into 8 islands and the IEEE 118-bus model into 65 islands as proposed for static state estimation [121]. The DSE estimation error of the two proposed methods, the UKF, and the Huber M-based UKF are shown on the smallest and largest bus number islands in Chapter 6. These simulations confirm the superiority of the proposed estimators compared to the UKF and Huber M-based UKF, the results may be provided upon request.

For the considered scenarios, it was apparent that the decoupling of the islands from the Kron reduced centralized power system model assisted greatly in the resiliency of the estimators. Where originally the UKF and Huber M-based UKF were fully impacted by the topology FDI and diverged in their estimations. Through the islanding scheme of decentralization and the removal of the Kron based topology matrix H, the UKF and Huber M-based UKF were still impacted by FDI, however did not diverge. Furthermore, the S-based and MM-based UKF rejected both the measurement FDI and topology FDI. We can conclude that the proposed application of high breakdown point S- and MM-estimators is suitable for robust dynamic estimation for large-scale power grids.

7.1   Recommendations for Future Work

When analyzing the results, potential avenues for future work have been identified. The islanding scheme could be improved to maximize the detection of attacks in a dynamic time frame. The algorithm proposed by [121] to decompose the larger IEEE 118-bus model into cyclic and radial islands with a minimum of 2 buses. The logic is that this decomposition will increase the number of attacks detected in the whole system. However, the approach considered the context of static state estimation, and further investigation might reveal that the dynamic modeling should result in a different islanding approach. While the objective of this work is not to propose an algorithm to decompose the system to increase the number of cyberattacks detected, this could be an important future research direction.

Reducing further the computation time of the robust estimators is also a very important factor in determining the decomposition of the system into islands. This will be investigated in the future. Furthermore, observability and maximum breakdown points analysis would be worth exploring. A new decomposition approach considering the PMU placement and a metric assessing cyber-security can result from research evaluating the observability and breakdown point assessment.

Recently, authors have proposed the GM-based UKF executed as a centralized DSE that can resist topology attacks. Theoretically the S- and MM- estimators can reach a higher breakdown point value than the GM as the state dimension increases; however, it's unclear how this translates into power systems practice when the regressor matrix is sparse, and the system is islanded. A future investigation is to compare all three estimators in the distributed dynamic state estimation.

In islanding the estimators, engineering judgment has been employed to determine the level of measurement and state noise each estimator may encounter. In the future, it would be beneficial to incorporate noise estimation, explicitly process noise and measurement noise Q and R, for the Kalman filters. This evaluation would be beneficial as the estimators will experience different levels of noise across a large system. Furthermore, if the researcher is utilizing the largest normalized residuals method, it could be used to assist in generating the threshold used for the bad data detection.

Chapter 8   References

[1]   F. C. Schweppe and J. Wildes, "Power System Static-State Estimation, Part I: Exact Model," *IEEE Trans. Power Appar. Syst.*, vol. PAS-89, no. 1, pp. 120–125, 1970, doi: 10.1109/TPAS.1970.292678.

[2]   F. C. Schweppe and D. B. Rom, "Power System Static-State Estimation, Part II: Approximate Model," *IEEE Trans. Power Appar. Syst.*, vol. PAS-89, no. 1, pp. 125–130, 1970, doi: 10.1109/TPAS.1970.292679.

[3]   F. C. Schweppe, "Power System Static-State Estimation, Part III: Implementation," *IEEE Trans. Power Appar. Syst.*, vol. PAS-89, no. 1, pp. 130–135, 1970, doi: 10.1109/TPAS.1970.292680.

[4]   R. E. Larson and L. P. Hajdu, "Potential applications and on-line implementation of power system state estimation," U.S. Department of Energy, Jan. 1969. doi: 10.2172/6990187.

[5]   R. E. Larson, J. Peschon, and W. F. Tinney, "State Estimation in Power Systems Part I: Theory and Feasibility," *IEEE Trans. Power Appar. Syst.*, vol. PAS-89, no. 3, pp. 345–352, 1970, doi: 10.1109/TPAS.1970.292711.

[6]   R. E. Larson, W. F. Tinney, L. P. Hajdu, and D. S. Piercy, "State Estimation in Power Systems Part II: Implementation and Applications," *IEEE Trans. Power Appar. Syst.*, vol. PAS-89, no. 3, pp. 353–363, 1970, doi: 10.1109/TPAS.1970.292712.

[7]   A. S. Debs and R. E. Larson, "A Dynamic Estimator for Tracking the State of a Power System," *IEEE Trans. Power Appar. Syst.*, vol. PAS-89, no. 7, pp. 1670–1678, 1970, doi: 10.1109/TPAS.1970.292822.

[8]   M. Brown Do Coulto Filho, J. Duncan Glover, and A. M. Leite da Silva, "State Estimators with Forecasting Capability," in *Power System Computation Conference*, 1993, vol. 2, pp. 689–696.

[9]   K. A. Clements and P. W. Davis, "Detection and identification of topology errors in electric power systems," *IEEE Trans. Power Syst.*, vol. 3, no. 4, pp. 1748–1753, 1988, doi: 10.1109/59.192991.

[10]   F. F. Wu and E. L. Wen-Hsiung, "Detection of topology errors by state estimation," *IEEE Trans. Power Syst.*, vol. 4, no. 1, pp. 176–183, 1989, doi: 10.1109/59.32475.

[11]   Y. Chakhchoukh and H. Ishii, "Coordinated Cyber-Attacks on the Measurement Function in Hybrid State Estimation," *IEEE Trans. Power Syst.*, vol. 30, no. 5, pp. 2487–2497, 2015, doi:

10.1109/TPWRS.2014.2357182.

[12]   A. Von Meier, E. Stewart, A. McEachern, M. Andersen, and L. Mehrmanesh, "Precision Micro-Synchrophasors for Distribution Systems: A Summary of Applications," *IEEE Trans. Smart Grid*, vol. 8, no. 6, pp. 2926–2936, Nov. 2017, doi: 10.1109/TSG.2017.2720543.

[13]   C. Rakpenthai and S. Uatrongjit, "WLAV based state estimation of power system using pseudo-voltage measurements," *2014 Int. Electr. Eng. Congr. iEECON 2014*, Oct. 2014, doi: 10.1109/IEECON.2014.6925973.

[14]   M. Huang, Z. Wei, G. Sun, and H. Zang, "Hybrid State Estimation for Distribution Systems with AMI and SCADA Measurements," *IEEE Access*, vol. 7, pp. 120350–120359, 2019, doi: 10.1109/ACCESS.2019.2937096.

[15]   S. Chakrabarti, E. Kyriakides, G. Ledwich, and A. Ghosh, "Inclusion of PMU current phasor measurements in a power system state estimator," *IET Gener. Transm. Distrib.*, vol. 4, no. 10, pp. 1104–1115, 2010, doi: 10.1049/iet-gtd.2009.0398.

[16]   A. Abur and A. Gómez Expósito, *Power system state estimation : theory and implementation*. CRC Press, 2004.

[17]   M. Göl and A. Abur, "LAV based robust state estimation for systems measured by PMUs," *IEEE Trans. Smart Grid*, vol. 5, no. 4, pp. 1808–1814, 2014, doi: 10.1109/TSG.2014.2302213.

[18]   M. Göl and A. Abur, "A modified Chi-Squares test for improved bad data detection," in *2015 IEEE Eindhoven PowerTech*, 2015, pp. 1–5. doi: 10.1109/PTC.2015.7232283.

[19]   Y. Chakhchoukh, H. Lei, and B. K. Johnson, "Diagnosis of Outliers and Cyber Attacks in Dynamic PMU-Based Power State Estimation," *IEEE Trans. Power Syst.*, vol. 35, no. 2, pp. 1188–1197, 2020, doi: 10.1109/TPWRS.2019.2939192.

[20]   J. Zhao *et al.*, "Power System Dynamic State Estimation: Motivations, Definitions, Methodologies, and Future Work," *IEEE Trans. Power Syst.*, vol. 34, no. 4, pp. 3188–3198, Jul. 2019, doi: 10.1109/TPWRS.2019.2894769.

[21]   G. Jia, "Distributed Dynamic Multi-area State Estimation with Fusion Technique," Ph.D. dissertation, Oregon State University, 2019.

[22]   J. Zhao, M. Netto, and L. Mili, "A Robust Iterated Extended Kalman Filter for Power System Dynamic State Estimation," *IEEE Trans. Power Syst.*, vol. 32, no. 4, pp. 3205–3216, Jul. 2017,

doi: 10.1109/TPWRS.2016.2628344.

[23] D. Doshi and M. Chankaya, "Particle Filter Based State Estimation of Power System," *Proc. - 2017 Int. Conf. Recent Trends Electr. Electron. Comput. Technol. ICRTEECT 2017*, vol. 2017-December, pp. 77–82, Dec. 2017, doi: 10.1109/ICRTEECT.2017.33.

[24] W. S. Rosenthal, A. M. Tartakovsky, and Z. Huang, "Ensemble Kalman Filter for Dynamic State Estimation of Power Grids Stochastically Driven by Time-Correlated Mechanical Input Power," *IEEE Trans. Power Syst.*, vol. 33, no. 4, Jul. 2018, doi: 10.1109/TPWRS.2017.2764492.

[25] R. A. Maronna, R. D. Martin, and V. J. Yohai, *Robust Statistics: Theory and Methods*. wiley, 2006. doi: 10.1002/0470010940.

[26] A. Monticelli, *State Estimation in Electric Power Systems*. Springer US, 1999. doi: 10.1007/978-1-4615-4999-4.

[27] A. Bretas, N. Bretas, J. B. A. London, and B. Carvalho, *Cyber-physical power systems state estimation*. Elsevier, 2021.

[28] C. A. Fantin, J. A. D. Massignan, M. R. Castillo, and J. B. A. London, "Observability, redundancy and gross error processing in state estimation using SCADA and synchronized phasor measurements," *2015 IEEE Eindhoven PowerTech, PowerTech 2015*, 2015, doi: 10.1109/PTC.2015.7232434.

[29] Y.-F. Huang, S. Werner, J. Huang, N. Kashyap, and V. Gupta, "State Estimation in Electric Power Grids: Meeting New Challenges Presented by the Requirements of the Future Grid," *IEEE Signal Process. Mag.*, vol. 29, no. 5, pp. 33–43, 2012, doi: 10.1109/MSP.2012.2187037.

[30] D. A. Haughton and G. T. Heydt, "A linear state estimation formulation for smart distribution systems," *IEEE Trans. Power Syst.*, vol. 28, no. 2, pp. 1187–1195, 2013, doi: 10.1109/TPWRS.2012.2212921.

[31] A. G. Phadke and J. S. Thorp, *Synchronized phasor measurements and their applications*. Springer, 2008.

[32] K. Dehghanpour, Z. Wang, J. Wang, Y. Yuan, and F. Bu, "A survey on state estimation techniques and challenges in smart distribution systems," *IEEE Trans. Smart Grid*, vol. 10, no. 2, pp. 2312–2322, 2019, doi: 10.1109/TSG.2018.2870600.

[33]   C. N. Lu, J. H. Teng, and B. S. Chang, "Power system network topology error detection," *IEE Proc. Gener. Transm. Distrib.*, vol. 141, no. 6, pp. 623–629, Nov. 1994, doi: 10.1049/IP-GTD:19941482.

[34]   L. Mili and G. Steeno, "A robust estimation method for topology error identification," *IEEE Trans. Power Syst.*, vol. 14, no. 4, pp. 1469–1476, 1999, doi: 10.1109/59.801932.

[35]   G. N. Korres and P. J. Katsikas, "Identification of circuit breaker statuses in WLS state estimator," *IEEE Trans. Power Syst.*, vol. 17, no. 3, pp. 818–825, Aug. 2002, doi: 10.1109/TPWRS.2002.800943.

[36]   A. Monticelli and F. F. Wu, "Network observability: Theory," *IEEE Trans. Power Appar. Syst.*, vol. PAS-104, no. 5, pp. 1042–1048, 1985, doi: 10.1109/TPAS.1985.323454.

[37]   M. Ayres and P. H. Haley, "Bad Data Groups in Power System State Estimation," *IEEE Trans. Power Syst.*, vol. 1, no. 3, pp. 1–7, 1986, doi: 10.1109/TPWRS.1986.4334946.

[38]   J. B. A. London, A. S. Bretas, and N. G. Bretas, "Algorithms to solve qualitative problems in power system state estimation," *Int. J. Electr. Power Energy Syst.*, vol. 26, no. 8, pp. 583–592, Oct. 2004, doi: 10.1016/J.IJEPES.2004.04.004.

[39]   A. A. Augusto, M. B. D. C. Filho, and J. C. S. De Souza, "Low-cardinality critical k-tuples in measurement sets for state estimation," *2013 IEEE Grenoble Conf. PowerTech, POWERTECH 2013*, 2013, doi: 10.1109/PTC.2013.6652169.

[40]   G. N. Korres and G. C. Contaxis, "Identification and updating of minimally dependent sets of measurements in state estimation," *IEEE Trans. Power Syst.*, vol. 6, no. 3, pp. 999–1005, 1991, doi: 10.1109/59.119239.

[41]   G. Liang, J. Zhao, F. Luo, S. R. Weller, and Z. Y. Dong, "A Review of False Data Injection Attacks Against Modern Power Systems," *IEEE Trans. Smart Grid*, vol. 8, no. 4, pp. 1630–1638, 2017, doi: 10.1109/TSG.2015.2495133.

[42]   J. Zhao, G. Zhang, M. La Scala, and Z. Wang, "Enhanced robustness of state estimator to bad data processing through multi-innovation analysis," *IEEE Trans. Ind. Informatics*, vol. 13, no. 4, pp. 1610–1619, Aug. 2017, doi: 10.1109/TII.2016.2626782.

[43]   K. Pan, A. Teixeira, M. Cvetkovic, and P. Palensky, "Cyber Risk Analysis of Combined Data Attacks Against Power System State Estimation," *IEEE Trans. Smart Grid*, vol. 10, no. 3, pp. 3044–3056, May 2019, doi: 10.1109/TSG.2018.2817387.

[44]   Y. Liu, P. Ning, and M. K. Reiter, "False data injection attacks against state estimation in electric power grids," *ACM Trans. Inf. Syst. Secur.*, vol. 14, no. 1, p. 33, Jun. 2011, doi: 10.1145/1952982.1952995.

[45]   J. Kim and L. Tong, "On topology attack of a smart grid: Undetectable attacks and countermeasures," *IEEE J. Sel. Areas Commun.*, vol. 31, no. 7, pp. 1294–1305, 2013, doi: 10.1109/JSAC.2013.130712.

[46]   A. Sharma, "A combined survey on distribution system state estimation and false data injection in cyber - physical power distribution networks," *IET Cyber-Physical Syst. Theory Appl.*, no. October 2020, pp. 41–62, 2021, doi: 10.1049/cps2.12000.

[47]   H. Zhang, B. Liu, and H. Wu, "Smart Grid Cyber-Physical Attack and Defense: A Review," *IEEE Access*, vol. 9, no. December 2015, pp. 29641–29659, 2021, doi: 10.1109/ACCESS.2021.3058628.

[48]   Y. Song, X. Liu, Z. Li, M. Shahidehpour, and Z. Li, "Intelligent data attacks against power systems using incomplete network information: a review," *J. Mod. Power Syst. Clean Energy*, vol. 6, no. 4, pp. 630–641, 2018, doi: 10.1007/s40565-018-0427-z.

[49]   M. Ferdowsi, A. Benigni, A. Lowen, B. Zargar, A. Monti, and F. Ponci, "A scalable data-driven monitoring approach for distribution systems," *IEEE Trans. Instrum. Meas.*, vol. 64, no. 5, pp. 1292–1305, 2015, doi: 10.1109/TIM.2015.2398991.

[50]   Y. Weng, R. Negi, C. Faloutsos, and M. D. Ilic, "Robust Data-Driven State Estimation for Smart Grid," *IEEE Trans. Smart Grid*, vol. 8, no. 4, pp. 1956–1967, 2017, doi: 10.1109/TSG.2015.2512925.

[51]   J. Yan, B. Tang, and H. He, "Detection of false data attacks in smart grid with supervised learning," *Proc. Int. Jt. Conf. Neural Networks*, vol. 2016-Octob, pp. 1395–1402, 2016, doi: 10.1109/IJCNN.2016.7727361.

[52]   J. Chen *et al.*, "Impact analysis of false data injection attacks on power system static security assessment," *J. Mod. Power Syst. Clean Energy*, vol. 4, no. 3, pp. 496–505, 2016, doi: 10.1007/s40565-016-0223-6.

[53]   M. Ganjkhani, S. N. Fallah, S. Badakhshan, S. Shamshirband, and K. wing Chau, "A novel detection algorithm to identify false data injection attacks on power system state estimation," *Energies*, vol. 12, no. 11, pp. 1–19, 2019, doi: 10.3390/en12112209.

[54] L. Che, X. Liu, Z. Li, and Y. Wen, "False Data Injection Attacks Induced Sequential Outages in Power Systems," *IEEE Trans. Power Syst.*, vol. 34, no. 2, pp. 1513–1523, Mar. 2019, doi: 10.1109/TPWRS.2018.2871345.

[55] P. J. Rousseeuw and A. M. Leroy, *Robust regression and outlier detection*. Wiley, 1987.

[56] P. J. Huber, "Robust Estimation of a Location Parameter," *Ann. Math. Stat.*, vol. 35, no. 1, pp. 73–101, Mar. 1964, doi: 10.1214/AOMS/1177703732.

[57] H. M. Merrill and F. C. Schweppe, "Bad data suppression in power system static state estimation," *IEEE Trans. Power Appar. Syst.*, vol. PAS-90, no. 6, pp. 2718–2725, 1971, doi: 10.1109/TPAS.1971.292925.

[58] C. H. Ho, H. C. Wu, S. C. Chan, and Y. Hou, "A Robust Statistical Approach to Distributed Power System State Estimation with Bad Data," *IEEE Trans. Smart Grid*, vol. 11, no. 1, pp. 517–527, Jan. 2020, doi: 10.1109/TSG.2019.2924496.

[59] C. Xu and A. Abur, "A fast and robust linear state estimator for very large scale interconnected power grids," *IEEE Trans. Smart Grid*, vol. 9, no. 5, pp. 4975–4982, Sep. 2018, doi: 10.1109/TSG.2017.2676348.

[60] M. Gol and A. Abur, "A hybrid state estimator for systems with limited number of PMUs," *IEEE Trans. Power Syst.*, vol. 30, no. 3, pp. 1511–1517, May 2015, doi: 10.1109/TPWRS.2014.2344012.

[61] L. Mili, V. Phaniraj, and P. J. Rousseeuw, "Least Median Of Squares Estimation In Power Systems," *IEEE Trans. Power Syst.*, vol. 6, no. 2, pp. 511–523, 1991, doi: 10.1109/59.76693.

[62] L. Mili and P. J. Rousseeuw, "Robust State Estimation of Electric Power Systems," *IEEE Trans. Circuits Syst. I Fundam. Theory Appl.*, vol. 41, no. 5, pp. 349–358, 1994, doi: 10.1109/81.296336.

[63] P. J. Rousseeuw, "Least Median of Squares Regression," *J. Am. Stat. Assoc.*, vol. 79, no. 388, pp. 871–880, 1984.

[64] P. J. Huber and E. M. Ronchetti, *Robust Statistics*. Wiley, 2011. [Online]. Available: https://books.google.com/books?id=j1OhquR_j88C

[65] W. W. Kotiuga and M. Vidyasagar, "Bad data rejection properties of weighted least absolute value techniques applied to static state estimation," *IEEE Trans. Power Appar. Syst.*, vol. PAS-

101, no. 4, pp. 844–853, 1982, doi: 10.1109/TPAS.1982.317150.

[66] A. M. Zoubir, V. Koivunen, Y. Chakhchoukh, and M. Muma, "Robust Estimation in Signal Processing: A Tutorial-Style Treatment of Fundamental Concepts," *IEEE Signal Process. Mag.*, vol. 29, no. 4, pp. 61–80, 2012, doi: 10.1109/MSP.2012.2183773.

[67] A. Primadianto, W. T. Lin, and C. N. Lu, "Performance comparison of distribution system state estimation methods," *IEEE PES Innov. Smart Grid Technol. Conf. Eur.*, pp. 1121–1126, 2016, doi: 10.1109/ISGT-Asia.2016.7796543.

[68] W. M. Lin, "State estimation for distribution systems with zero-injection constraints," *IEEE Trans. Power Syst.*, vol. 11, no. 1, pp. 518–524, 1996, doi: 10.1109/59.486142.

[69] M. Abdel-Akher, K. M. Nor, and A. H. A. Rashid, "Improved three-phase power-flow methods using sequence components," *IEEE Trans. Power Syst.*, vol. 20, no. 3, pp. 1389–1397, 2005, doi: 10.1109/TPWRS.2005.851933.

[70] E. A. Blood, "From Static to Dynamic Electric Power Network State Estimation: The Role of Bus Component Dynamics," Ph.D. dissertation, Carnegie Mellon University, 2011. doi: 10.1184/R1/6717410.V1.

[71] L. Xie, D. H. Choi, S. Kar, and H. V. Poor, "Fully distributed state estimation for wide-area monitoring systems," *IEEE Trans. Smart Grid*, vol. 3, no. 3, pp. 1154–1169, 2012, doi: 10.1109/TSG.2012.2197764.

[72] S. Chen, Z. Wei, G. Sun, N. Lu, Y. Sun, and Y. Zhu, "Multi-area distributed three-phase state estimation for unbalanced active distribution networks," *J. Mod. Power Syst. Clean Energy*, vol. 5, no. 5, pp. 767–776, 2017, doi: 10.1007/s40565-016-0237-0.

[73] C. Bila, "Power System Dynamic State Estimation and Load Modeling," M.S. thesis, Northeastern University, 2013.

[74] A. Rouhani, "Robust Dynamic State Estimation In Power Systems," Ph.D. dissertation, Northeastern University, 2017.

[75] J. Zhao, "A Robust Dynamic State and Parameter Estimation Framework for Smart Grid Monitoring and Control," Ph.D. dissertation, Virginia Polytechnic Institute and State University, 2018.

[76] C. Dafis, "An observability formulation for nonlinear power systems modeled as differential

algebraic systems," Ph.D. dissertation, Drexel University, 2005.

[77] A. Thabet, "Estimation de l'état pour la surveillance des systèmes de grandes dimensions. Application aux réseaux électriques," Ph.D. dissertation, Ecole Nationale d'Ingénieurs de Gabès, 2012.

[78] "OpenDSS." https://www.epri.com/pages/sa/opendss (accessed Jan. 05, 2019).

[79] J. D. Glover, M. S. Sarma, and T. Overbye, *Power System Analysis and Design*. Cengage Learning, 2011. [Online]. Available: https://books.google.com/books?id=U77A2C37QesC

[80] T. Van Cutsem and C. Vournas, "Voltage stability of electric power systems," *Volt. Stab. Electr. Power Syst.*, pp. 1–378, 2008, doi: 10.1007/978-0-387-75536-6.

[81] "IEEE Standard for Synchrophasor Measurements for Power Systems -- Amendment 1: Modification of Selected Performance Requirements," 2014. doi: 10.1109/IEEESTD.2014.6804630.

[82] R. D. Zimmerman, C. E. Murillo-Sánchez, and R. J. Thomas, "MATPOWER: Steady-state operations, planning, and analysis tools for power systems research and education," *IEEE Trans. Power Syst.*, vol. 26, no. 1, pp. 12–19, Feb. 2011, doi: 10.1109/TPWRS.2010.2051168.

[83] B. W. Gordon, "Dynamic Sliding manifolds for Realization of High Index Differential-Algebraic Systems," *Asian J. Control*, vol. 5, no. 4, pp. 454–466, Dec. 2003, doi: https://doi.org/10.1111/j.1934-6093.2003.tb00163.x.

[84] B. Stott and O. Alsac, "Fast decoupled load flow," *IEEE Trans. Power Appar. Syst.*, vol. PAS-93, no. 3, pp. 859–869, 1974, doi: 10.1109/TPAS.1974.293985.

[85] A. Langner, "Multi-Area Distribution System State Estimation Using a Virtual Reference," Ph.D. dissertation, Northeastern University, 2021.

[86] A. Mouco, "Robust monitoring and fault location in 3-phase power grids," Ph.D. dissertation, Northeastern University, Boston, Massachusetts, 2019. doi: 10.17760/D20325267.

[87] G. Kron, *Tensor analysis of networks*. New York: J. Wiley & Sons, inc.; Chapman & Hall, limited, 1939. [Online]. Available: file://catalog.hathitrust.org/Record/001617432

[88] W. H. Kersting, *Distribution System Modeling and Analysis*. CRC Press, 2016. doi: 10.1201/B11697.

[89] A. Primadianto and C. N. Lu, "A Review on Distribution System State Estimation," *IEEE Trans.*

Power Syst., vol. 32, no. 5, pp. 3875–3883, 2017, doi: 10.1109/TPWRS.2016.2632156.

[90]   D. Simon, *Optimal state estimation: Kalman, H∞, and nonlinear approaches*. Wiley Blackwell, 2006. doi: 10.1002/0470045345.

[91]   P. J. Huber, "John W. Tukey's contributions to robust statistics," *https://doi.org/10.1214/aos/1043351251*, vol. 30, no. 6, pp. 1640–1648, Dec. 2002, doi: 10.1214/AOS/1043351251.

[92]   "Fit robust linear regression - MATLAB robustfit." https://www.mathworks.com/help/stats/robustfit.html (accessed Mar. 28, 2022).

[93]   Y. Li, J. Li, J. Qi, and L. Chen, "Robust Cubature Kalman Filter for Dynamic State Estimation of Synchronous Machines Under Unknown Measurement Noise Statistics," *IEEE Access*, vol. 7, pp. 29139–29148, 2019, doi: 10.1109/ACCESS.2019.2900228.

[94]   V. J. Yohai, "High Breakdown-Point and High Efficiency Robust Estimates for Regression," *Ann. Stat.*, vol. 15, no. 2, pp. 642–656, Apr. 1987, [Online]. Available: http://www.jstor.org/stable/2241331

[95]   P. Rousseeuw and V. Yohai, "Robust Regression by Means of S-Estimators," pp. 256–272, 1984, doi: 10.1007/978-1-4615-7821-5_15.

[96]   L. Mili and C. W. Coakley, "Robust Estimation in Structured Linear Regression," *Ann. Stat.*, vol. 24, no. 6, pp. 2593–2607, Nov. 1996, [Online]. Available: http://www.jstor.org/stable/2242701

[97]   V. J. Yohai, "High Breakdown-Point and High Efficiency Robust Estimates for Regression," *https://doi.org/10.1214/aos/1176350366*, vol. 15, no. 2, pp. 642–656, Jun. 1987, doi: 10.1214/AOS/1176350366.

[98]   C. Croux, G. Dhaene, and D. Hoorelbeke, "Robust Standard Errors for Robust Estimators," *Work. Pap. Dep. Econ. Leuven*, 2003, Accessed: Jan. 04, 2022. [Online]. Available: https://feb.kuleuven.be/public/u0017833/Programs/#mme

[99]   R. Andersen, *Modern methods for robust regression*. Los Angeles: Sage Publications, 2008.

[100] Y. Susanti, H. Pratiwi, S. H. Sulistijowati, and T. Liana, "M Estimation, S Estimation, and MM Estimation in Robust Regression," *Int. J. Pure Appl. Math.*, vol. 91, no. 3, pp. 349–360, 2014, doi: 10.12732/ijpam.v91i3.7.

[101] N. Carter, "Data Science for Mathematicians," *Data Sci. Math.*, Sep. 2020, doi: 10.1201/9780429398292.

[102] R. Piziak and P. L. Odell, "Full Rank Factorization of Matrices," *Math. Mag.*, vol. 72, no. 3, p. 193, Jun. 1999, doi: 10.2307/2690882.

[103] N. Kishore Kumar and J. Schneider, "Literature survey on low rank approximation of matrices," *Linear Multilinear Algebr.*, vol. 65, no. 11, pp. 2212–2244, Jun. 2016, doi: 10.1080/03081087.2016.1267104.

[104] M. Koller, "Nonsingular subsampling for S-estimators with categorical predictors," Aug. 2012, Accessed: Sep. 10, 2021. [Online]. Available: https://arxiv.org/abs/1208.5595v1

[105] A. G. Miles *et al.*, "An Integrated Transactive Energy Market and Distribution Grid Analysis Platform," *2021 Grid Futur. Conf.*, 2021.

[106] R. C. Dugan, "Reference Guide The Open Distribution System Simulator (OpenDSS) With edits by Andrea Ballanti," 2016.

[107] S. Somasundaram *et al.*, "Reference Guide for a Transaction-Based Building Controls Framework," 2014. Accessed: Sep. 15, 2021. [Online]. Available: http://www.ntis.gov/ordering.htm

[108] B. A. Akyol, J. N. Haack, B. J. Carpenter, S. Katipamula, R. G. Lutes, and G. Hernandez, "Transaction-Based Building Controls Framework, Volume 2: Platform Descriptive Model and Requirements," 2015, Accessed: Sep. 15, 2021. [Online]. Available: http://www.ntis.gov/ordering.htm

[109] S. Hanif, "Distribution Locational Marginal Price: Approximations, Solution Algorithm and Organization," Ph.D. dissertation, Technischen Universität München, 2018. doi: 10.13140/RG.2.2.10748.39040.

[110] "Transactive Energy: American Perspectives on Grid Transformations | Energy Central." https://energycentral.com/c/ec/transactive-energy-american-perspectives-grid-transformations (accessed Sep. 15, 2021).

[111] D. J. Hammerstrom, R. Ambrosio, J. Brous, and Carlon T.A, "Pacific Northwest GridWise™ Testbed Demonstration Projects; Part I. Olympic Peninsula Project," 2007. Accessed: Sep. 15, 2021. [Online]. Available: http://www.ntis.gov/ordering.htm

[112] S. Hanif, M. Barati, A. Kargarian, H. Beng Gooi, and T. Hamacher, "Multiphase Distribution Locational Marginal Prices: Approximation and Decomposition," *IEEE Power Energy Soc. Gen. Meet.*, pp. 1–5, 2018, doi: 10.1109/PESGM.2018.8585925.

[113] Aditya Tarali, "Bad Data Detection In Two Stage Estimation Using Phasor Measurements," M.S. thesis, Northeastern University, 2012.

[114] S. Priyadarshini and C. Panigrahi, "Optimal Allocation of Synchrophasor Units in the Distribution Network Considering Maximum Redundancy," *Eng. Technol. Appl. Sci. Res.*, vol. 10, pp. 6494–6499, Dec. 2020, doi: 10.48084/etasr.3862.

[115] "Uniformly distributed random numbers - MATLAB rand." https://www.mathworks.com/help/matlab/ref/rand.html (accessed Sep. 16, 2021).

[116] S. Wang, J. Zhao, and Z. Huang, "Assessing Gaussian Assumption of PMU Measurement Error Using Field Data," *IEEE Trans. Power Deliv.*, vol. 33, no. 6, doi: 10.1109/TPWRD.2017.2762927.

[117] "Create Gaussian mixture model - MATLAB." https://www.mathworks.com/help/stats/gmdistribution.html (accessed Mar. 17, 2022).

[118] "Resources | PES Test Feeder." https://site.ieee.org/pes-testfeeders/resources/ (accessed Sep. 10, 2021).

[119] B. Gasbaoui and B. Allaoua, "Ant Colony Optimization Applied on Combinatorial Problem for Optimal Power Flow Solution", Accessed: Apr. 24, 2022. [Online]. Available: http://lejpt.academicdirect.org

[120] I. Pena, C. Brancucci, and B. M. Hodge, "An Extended IEEE 118-bus Test System with High Renewable Penetration," *IEEE Trans. Power Syst.*, Apr. 2017, doi: 10.1109/TPWRS.2017.2695963.

[121] N. Ahmadi, Y. Chakhchoukh, and H. Ishii, "Power systems decomposition for robustifying state estimation under cyber attacks," *IEEE Trans. Power Syst.*, vol. 36, no. 3, pp. 1922–1933, May 2021, doi: 10.1109/TPWRS.2020.3026951.

[122] M. G. Cheniae, L. Mili, and P. J. Rousseeuw, "Identification of multiple interacting bad data via power system decomposition," *IEEE Trans. Power Syst.*, vol. 11, no. 3, pp. 1555–1563, 1996, doi: 10.1109/59.535697.

[123]   Ali R. Al-Roomi, "Power Flow Test Systems Repository," 2015. https://al-roomi.org/power-flow/ (accessed Aug. 04, 2022).